universität wien

DISSERTATION / DOCTORAL THESIS

Titel der Dissertation /Title of the Doctoral Thesis

Controlled Direct Synthesis of Graphene Nanoribbons without Metal Catalyst

verfasst von / submitted by

Dott.ssa Dott. mag. Valeria Milotti

angestrebter akademischer Grad/ in partial fulfilment of the requirements for the degree of

Doktorin der Naturwissenschaften

(Dr.rer.nat.)

Wien, 2021 / Vienna 2021

Studienkennzahl lt. Studienblatt / degree programme code as it appears on the student record sheet:	UA 796 605 411
Dissertationsgebiet lt. Studienblatt / field of study as it appears on the student record sheet:	Physik
Betreut von / Supervisor:	Univ.-Prof. Mag. Dr. Thomas Pichler

Abstract

As the end of Moore's law approaches, alternatives to inorganic semiconductor technology are required for the continued miniaturization of electronic devices. Candidates for this change of paradigm are graphene nanoribbons (GNRs), one-dimensional strips of graphene, as they have the advantage of being compatible with current transistor technology. Their atomically precise synthesis and non destructive characterization are important steps toward GNR application as novel building blocks in the semiconductor industry, as control over topology and edge terminations would allow tailoring of their electronic properties.

However, control over GNR topology is currently achieved by bottom-up synthesis (BUS) on metallic surfaces. This is not ideal for either characterization nor practical application, thus a post-synthesis transfer to insulating substrates is usually required.

BUS alternatives to this method are emerging but require further investigation. One is cyclodehydrofluorination of fluorinated organic precursors, which has recently been shown to be a promising pathway to achieve metal-free bottom-up synthesis of nanographenes. Another is encapsulation and polymerization of already GNR-like small molecules inside single-walled carbon nanotubes (SWCNTs), which yields long homogeneous GNR.

In this work, I investigate these two synthesis methods and characterize them in a contactless manner via photoselective resonance Raman spectroscopy.

First, I present how to apply in-situ laser annealing to induce cyclodehydrofluorination leading to nanographene formation directly on non-metallic surfaces. In-situ laser annealing allows not only to influence chemical reactions, but also to have a fast and contact-free monitoring of the reaction products. Optimization of the laser annealing process adds a new level of control in the tailored synthesis of nanographenes on non-metallic substrates. This is a very promising pathway to unravel the full application potential of nanographenes in general and GNR in particular, enabling a fast optimization of precursor molecules and substrate geometry engineered for specific applications.

Secondly, I use multifrequency resonance Raman spectroscopy on narrow armchair GNR encapsulated in single-walled carbon nanotubes samples annealed at stepwise increasing temperatures, in order to unravel the fingerprints of precursor and hybrid system. I demonstrate their different responses to heating and find the goldilocks condition for signal disentanglement with a focus on Raman modes originating from edge terminations. Finally, I compare experimental results with theoretical spectra obtained via density-functional theory calculations. Thus this study represents a critical step forward in the successful analysis of the hybrid system GNR@SWCNT unraveled from its precursor's response.

Zusammenfassung

Da das Ende des Moore'schen Gesetz näher rückt, werden Alternativen zur anorganischen Halbleitertechnologie für die weiter Miniaturisierung elektronischer Geräte benötigt. Kandidaten für diesen Paradigmenwechsel sind Graphen-Nanobänder (GNRs), eindimensionale Streifen von Graphen, da sie den Vorteil haben, mit aktueller Transistoren-Technologie kompatibel zu sein. Ihre atomar präzise Synthese und zerstörungsfreie Charakterisierung sind wichtige Schritte zur GNR-Anwendung als neuartige Bausteine in der Halbleiter Industrie, da die Kontrolle über Topologie und Edge-Abschlüsse die Anpassung ihrer elektronische Eigenschaften, ermöglichen würde.

Kontrolle über die GNR-Topologie wird derzeit jedoch durch eine Bottom-up-Synthese (BUS) auf metallischen Oberflächen erreicht. Das ist weder für die Charakterisierung noch die praktische Anwendung ideal, daher ist in der Regel eine Übertragung nach der Synthese auf isolierende Substrate erforderlich. BUS-Alternativen zu dieser Methode sind im Entstehen, weitere Untersuchungen werden jedoch benötigt. Eine davon ist die Cyclodehydrofluorierung fluorierter organischer Präkursoren, die kürzlich als vielversprechender Weg zur metallfreien Bottom-up-Synthese von Nanographenen entdeckt worden ist. Eine anderere Methode ist die Verkapselung und Polymerisation von bereits GNR-ähnlichen kleinen Molekülen in einwandigen Kohlenstoffnanoröhren (SWCNTs), wodurch lange homogene GNR entstehen.

In dieser Arbeit untersuche ich diese beiden Synthesemethoden und charakterisiere sie in einer kontaktlosen Weise mit photoselektiver Resonanz-Raman-Spektroskopie.

Zuerst präsentiere ich, wie in-situ-Lasertemperierung angewendet wird, um eine Cyclodehydrofluorierung zu induzieren, die zur Bildung von Nanographen direkt auf nichtmetallischen Oberflächen führt. In-situ Lasertemperierung ermöglicht nicht nur die Beeinflussung chemischer Reaktionen, sondern auch eine schnelle und kontaktlose Überwachung der Reaktionsprodukte. Die Optimierung des Lasertemperierung-Prozesses bietet ein neues Maß an Kontrolle bei der maßgeschneiderten Synthese von Nanographenen auf nichtmetallischen Substraten. Dies ist ein vielversprechender Weg, um das volle Anwendungspotenzial von Nanographenen im Allgemeinen und GNR im Besonderen zu erschließen und eine schnelle Optimierung von Präkursormolekülen und Substratgeometrien für spezielle Anwendungen zu ermöglichen.

Zweitens verwende ich Multifrequenz-Resonanz-Raman-Spektroskopie an schmalen Armlehnenstuhl-GNR, eingekapselt in einwandigen Kohlenstoffnanoröhren Proben, die bei schrittweise steigenden Temperaturen getempert werden, um die Fingerabdrücke von Präkursor und Hybridsystem zu entwirren. Ich demonstriere ihre unterschiedlichen Reaktionen auf Erwärmung und finde die Optimalbedingung für Signalentflechtung mit einem Fokus auf Raman-Moden, die von Kantenabschlüssen stammen. Schließlich vergleiche ich experimentelle Ergebnisse mit theoretischen Spektren, welche mit Dichte-

funktionaltheorie berechnet wurden. Somit stellt diese Arbeit einen entscheidenden Fortschritt in der erfolgreichen Analyse des Hybridsystems GNR@SWCNT, getrennt vom Einfluss seines Präkursor, dar.

Contents

List of Figures

List of Tables

Chapter 1

Motivation and Goals

As integrated circuits have become exponentially smaller, microprocessors are about to reach the physical limits of miniaturization.[1, 2] A new paradigm in microengineering is required for electronics to continue following Moore's Law. Carbon nanomaterials have emerged in the past few years as likely candidates for this technological revolution.[3, 4]

Single layer graphene was first isolated in 2004 by Geim and Novoselov and soon after employed in an electronic device.[5, 6] This work was one most prominent breakthroughs of the turn of the century and it was rewarded with a Nobel Prize in 2010.[7] However, this material's electronic applications are limited by the absence of a gap between its valence and conduction bands.[8] Quantum confinement provides a way to open the gap while preserving other desirable characteristics of graphene, which is realized in carbon nanotubes (CNTs) and GNRs.[9]

Other than miniaturization CNT and GNR transistors offer other advantages, such as their ability to operate at lower voltages than their inorganic counterparts.[10, 11, 12] Simulations and experiments predict better on/off current ratio for single-walled carbon nanotube (SWCNT)-based field-effect transistor (FET) than GNR-based FET[13, 14]. However other challenges arise from the synthesis of this material, as only two thirds of SWCNTs are semiconducting and must be separated from the metallic fraction.[15] At the present time, the purity needed for large-scale applications is still elusive.

On the other hand, the electronic characteristics of GNRs depend mainly on their topology and can therefore be specifically tailored by employing suitable precursor molecules. In the same way, it is possible to create GNR heterojunctions, to lower the Schottky barrier at the contacts.[16, 17, 18]

Large scale applications are not yet available, as current high-yield state-of-the-art synthesis requires a metal substrate as catalyst, which hinders direct characterization of GNR and production of GNR-based transistors.[19] Therefore, research efforts into GNR and their application would greatly benefit from a synthesis method independent of any metallic surface. Currently available strategies under examination include *on-surface synthesis on insulators from fluorinated precursors* and *polymerization of small molecules encapsulated in SWCNT.*[20, 21]

Because of quantum confinement, edge morphology has a great influence over the characteristics of GNR, as it contributes to determine the electronic transport properties.[22, 23, 24] One well established tool in the characterization of 2D-carbon materials is Raman spectroscopy. While modes related to width and other topological characteristics of GNR have long since been analyzed, edge-related modes have so far

only been identified.[25] However, they provide a window into edge properties, which are pivotal for complete characterization of GNR and future applications.

In general, smaller width nanoribbons present bigger quantum confinement effects and thus more opened bandgaps. Furthermore, GNR with armchair edge topology can be categorized into three families according to the number of C-C dimers spanning their width, with the family with (N+2) number of dimers having the smallest bandgaps. GNR about 0.5 nm wide (5-AGNR, 6-AGNR and 7-AGNR) are suitable for encapsulation in SWCNT with mean diameter of 1.4 nm, which are the most easily retrievable SWCNT. 6-AGNR and 7-AGNR have been studied and characterized, while 5-AGNR, which, with its energy gap in the order of 1 eV, would be the most suitable for electronic applications, has yet to be investigated.[26]

The main objective of my project has been to use Raman spectroscopy for the characterization of two metal-free bottom-up synthesis methods of graphene nanoribbons. This aims at facilitating their characterization in the short term in view of eventual bulk production and industrial application.

For this purpose, I investigate the step-by-step graphitization of a small fluorinated precursor by using laser annealing as a localized heat source and Raman microscopy as a contact-free and thus non-disruptive characterization method. This allows me to shed light into the so far unknown chemical processes that take place during polymerization of this kind of precursors, creating a template for future investigations.

Furthermore, I encapsulate a small rylene dye, terrylene into SWCNT, with a narrow diameter distribution selected to promote precursor alignment and thus polymerization into a 5-AGNR. I use multifrequency Raman spectroscopy to investigate the photoselective resonances in this hybrid system, in order to disentangle the edge-related vibrational modes of GNR from those of the precursor and study for the first time the Raman response of edge passivation-related modes.

Chapter 2

Carbon and its Allotropes

Carbon is one of the most versatile elements in the periodic table. Its ability to hybridize and its electronegativity allow it to form an exorbitant number of stable molecules. Because of this extraordinary characteristic, carbon-based molecules are found in abundance in very different environments, from minerals to living organisms.[27]

In recent years, carbon-based molecules have been the focus of intense research to build the basis for a technological revolution that would allow the transistor industry to surpass the physical limits of Moore's law. This field has lead to multiple technological breakthroughs. Some of these can be already found in commercialized products, one high profile example of which are high contrast screens made of organic light emitting diodes (O-LED), currently widespread especially in the smartphone market.[28, 29]

As a member of the sixth group in the periodic table, in its ground state Carbon has two electrons in the 2s orbital and another six in the three 2p orbitals, with four electrons available to form bonds. However, the valence orbitals can mix into hybrid sp^n orbitals, where n indicates the hybridization type, each of which is related to different spatial distributions of carbon bonds: linear for sp hybridization, planar for sp^2 hybridization and three dimensional for sp^3 hybridization.

For the purposes of this work, carbon allotropes are especially interesting. These are structures which contain only carbon in their basic molecular composition.

Hybridization can be used as the discriminating factor to classify a few examples of interesting carbon allotropes, whose ball and stick model is depicted in figure 2.1:

sp - linear molecules cumulene and polyyne contain, respectively, carbon chains with double carbon-carbon bonds (=C=C=) and alternated single and triple carbon-carbon bonds (–C≡C–), they are called carbyne when the carbon chain becomes infinitely long;[30]

sp^2 - the template for planar carbon allotropes is graphene, which is the parent material to both graphene nanoribbons and carbon nanotubes, while the bulk form of graphene is graphite, which is the most thermodinamically stable form of carbon at room temperature and pressure;[8]

sp^3 - diamond is the cubic form of graphite and it is the hardest naturally occurring material.[31, 32]

Allotropes with mixed hybridizations are also possible. One example are small fullerenes, the smallest of which is C_{60} buckminsterfullerene. They consist of a graphene layer curled up into a ball. Because of curvature effect, their hybridization is no longer pure sp^2, but it presents itself mixed with sp^3 hybridization. This contributes to the chemical reactivity of fullerenes. Specifically, in the case of C_{60} curvature effects lead to a $sp^{2.28}$ hybridization.[33]

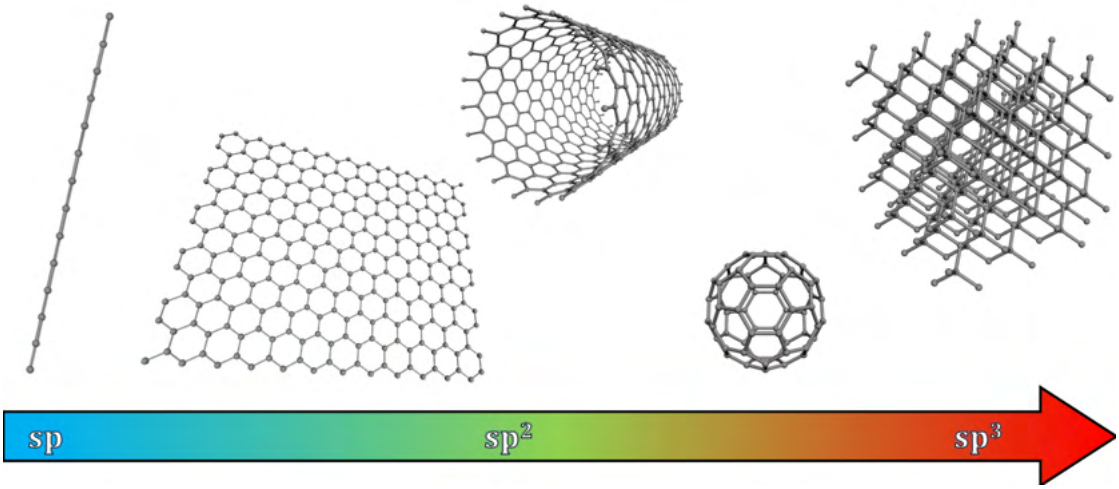

Figure 2.1: Ball-and-stick models of some carbon allotropes with different hybridizations, from one to three dimensional. Left to right: carbyne (sp), graphene (sp^2), single-walled carbon nanotube (sp^2 with curvature effects), C_{60} buckminsterfullerene ($sp^{2.28}$), and diamond (sp^3).

2.1 Graphene Related Nanomaterials

Graphene is a planar monolayer of sp^2 hybridized carbon atoms arranged in a honeycomb pattern. It was first successfully isolated in 2004 by Geim and Novoselov, which was recognized with a Nobel Prize in 2010.[5]

Theoretical models of graphene predict that its electrons behave as massless particles (at least approximately at low energies around the Fermi level), it possesses extremely large thermal conductivity and the highest tensile strength ever measured.[34, 35, 36]

Despite its extraordinary properties, its vanishing band-gap makes it unappealing for most electronic applications.[8] One way to surmount this problem is to open the bandgap through quantum confinement, as is the case for graphene nanoribbons and carbon nanotubes.[37]

Graphene nanoribbons (GNRs) are quasi-one dimensional strips of honeycomb carbon with vanishing width-to-length ratio. Though their structure is based on their parent material, graphene, GNRs are far superior candidates for the development of carbon-based devices. This is due to the tunability of their electronic and optical properties, which mainly depend on the topological characteristics of the ribbon. In fact, ribbon width, edge morphology and edge termination play a pivotal role in determining electrical, optical and magnetic properties of GNR.

The first paper to expressly correlate the electronic properties of finite graphene systems to their edge topology was published in 1996 by *Fujita et al.*. The authors demonstrated that control over a nanoscale ribbon's edges influences the overall electronic state.[22] Since then, further theoretical and experimental research has confirmed that, depending on their edge morphology and their width, GNR can behave as metals, semiconductors or insulators.[38, 39]

As precise control over the topology is required, bottom-up synthesis (BUS) is the ideal way to obtain nanoribbons. It was reported for the first time in 2010 by *Cai et al.*. The group established what is today the most widespread synthesis route, which consists in polymerization of small precursor molecules on a metallic surface, which acts as reaction catalyst.[40, 25]

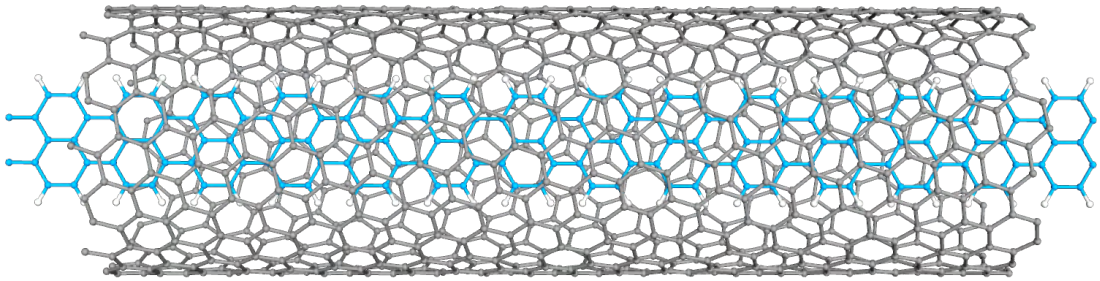

Figure 2.2: Ball-and-stick sketch of a GNR encapsulated in a SWCNT.

Also a semi-one dimensional derivative material of graphene, a **carbon nanotube (CNT)** can be thought of as a GNR "rolled-up" into a tube. Counting the number of walls in a CNT provides a first, rough classification into *single-walled carbon nanotubes (SWCNTs)* and *double-walled carbon nanotubes (DWCNTs)*. CNTs with more than two walls are called *multi-walled carbon nanotubes (MWCNTs)*.

Though some controversy exists on the discovery of MWCNT, SWCNT were first observed in 1991 by Iijima.[41]

Similarly to GNR, topological characteristics majorly affect the electronic properties of SWCNTs. The orientation of the graphene lattice determines whether the SWCNT is metallic or semiconducting, which exist in a 1:2 ratio. Moreover, the energy gap of semiconducting SWCNTs is inversely proportional to their diameter.[42, 37] The energy gap range is between 0.5 and 1.5 eV, which makes them attractive for FET integration.

Additionally, the synthesis of nanomaterials, SWCNTs can be used as nanoreactors, as they provide a protected hollow space for transformation and polymerization of small molecules, which is their main interesting characteristic in the scope of this work, such as the GNR@SWCNT sketched in figure 2.2.[43]

2.1.1 Graphene-Derivatives-Based Nanoelectronics

As mentioned above, graphene is unsuitable for most electronic components, as its vanishing band-gap prevents graphene-based transistors from switching off.[44] However, there are some notable applications, which include graphene-based optoelectronic components for photonics[45] and telecommunications.[46, 47]

With the exception of metallic SWCNT, smaller dimensions (respectively, diameter

and width) mean a bigger electronic band gap for both SWCNT and GNR. Both materials are under careful examination as building blocks for new kinds of technologies.

Because of their earlier discovery, to date SWCNT have been researched more extensively than GNR. The first transistor that employed a single SWCNT as channel, a CNTFET, was first built by *Tans et al.* in 1998.[48] Though a considerable Schottky barrier was present at the contacts, this problem can be solved with appropriate interfaces.[49] SWCNT-based field-effect transistors (FETs) are more energy efficient than those built out of inorganic semiconductors, as they operate at higher current densities and lower voltage.[10, 50, 51, 52]

Researchers have used this technology to build in 2013 a SWCNT-based computer with 178 CNTFET, able to run programs and operating systems.[53] The next big step was a microprocessor built out of 14000 CNTFET in 2019.[54]

SWCNT have also applications in the energy storage field, as they can be used to construct better capacitors.[55]

However, as one third of SWCNT are metallic, the outstanding challenge in building logic devices based on CNTFET is sample purity. In fact, a fast, low cost, high yield synthesis or separation method that would provide a sample with a concentration of metallic SWCNT impurities low enough for industrial applications has yet to be discovered.[56]

In FET fabrication, GNR offer a clear advantage over SWCNT, as their electronic characteristics of depend mainly on their topology, making it possible to tailor their band gap in with BUS methods. Specifically, GNR electronic properties are determined by the width, usually expressed in number N of C-C dimers spanning it, edge morphology and edge termination.[22, 23, 38]

The width necessary to open a gap in the band structure of graphene suitable for room-temperature nanoelectronics is 10 nm or less, which is at the limit of lithographic possibilities but easily achievable with BUS.[57, 58] The most commonly investigated edge morphologies are zigzag and armchair, though many other edge configurations are possible.[59] Edge terminations are also pivotal for electronic properties. Because of this, GNRFET could be used to build detectors for organic molecules.[60]

GNR of width N with armchair topologies, or N-AGNR, can be further categorized into three families with slightly different electronic gap behaviour, based on the number N.[38]

As is the case for CNTFETs, GNR-based FETs have been demonstrated to be able to operate at lower voltages than silicon-based transistors.[11, 12] BUS methods allow also the creation of GNR heterojunctions, to lower the Schottky barrier at the contacts.[16, 17, 18]

In this work, I investigate two GNR synthesis methods, in order to determine if they are good candidates for independence form metal substrates currently required for BUS.

Chapter 3

Electronic Properties of Planar Nanocarbons

The description of electronic properties of graphene-related materials in this chapter follows in part the book by Jorio et al. [9].

In this chapter, electronic properties of graphene and related materials will be discussed.

When the 2D material graphene is confined in 1D, either by rolling it up into a single-walled carbon nanotube or by cutting it into a graphene nanoribbon, the finite length forces the electronic wavefunction into standing waves along the smaller axis, thus introducing a quantization of the possible electronic states.

As both GNR and SWCNTs can be derived from graphene, many properties and their modeling are shared between the two materials. Though the main interest of this work is in GNR, I will first provide a description of SWCNTs as a template, which will also be useful later for the interpretation of spectral data of the hybrid system GNR@SWCNT.

3.1 Electronic Properties of Graphene

Graphene is a planar allotrope of carbon. Its molecular structure is composed of sp^2 hybridized carbon molecules arranged in a honeycomb pattern.

We start by defining two independent base vectors $\vec{a_1}$ and $\vec{a_2}$ for the real space honeycomb lattice of graphene (figure 3.1a), which can be expressed in Cartesian coordinates (with x axis parallel to an arbitrary C-C bond) as:

$$\vec{a_1} = \left(\frac{\sqrt{3}}{2}a, \frac{a}{2}\right) \qquad \vec{a_2} = \left(\frac{\sqrt{3}}{2}a, -\frac{a}{2}\right) \tag{3.1}$$

where $a = |\vec{a_1}| = |\vec{a_2}| = 2.46\,\text{Å}$ is the lattice constant of graphene.

From the usual definition, it follows that the reciprocal lattice base vectors are:

$$\vec{b_1} = \left(\frac{2\pi}{\sqrt{3}a}, \frac{2\pi}{a}\right) \qquad \vec{b_2} = \left(\frac{2\pi}{\sqrt{3}a}, -\frac{2\pi}{a}\right) \tag{3.2}$$

and the reciprocal lattice constant is $4\pi/\sqrt{3}a$ (figure 3.1b).[61]

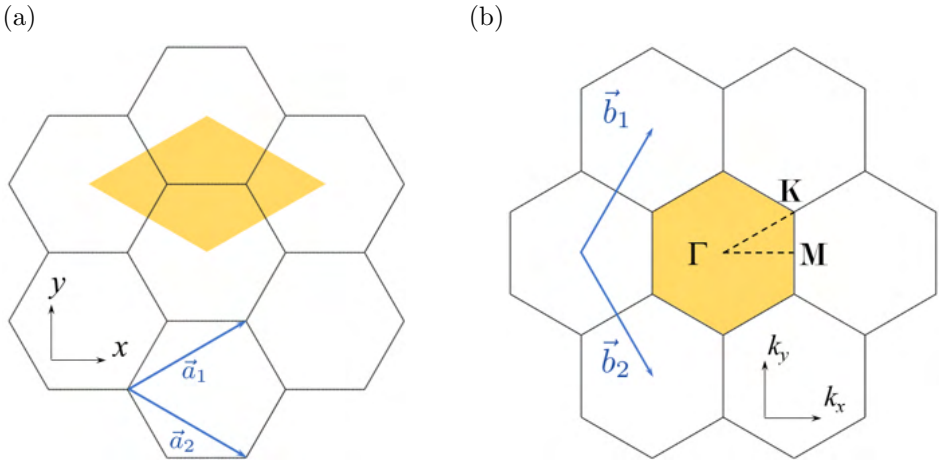

Figure 3.1: (a) Real and (b) reciprocal space lattice of graphene.

The band structure of graphene can be modeled using the well known tight-binding model. The thus found computed energy dispersion in the first Brilluoin zone of graphene is depicted in 3.2. At the K points valence and conduction bands touch, making graphene a zero band-gap semiconductor, or semimetal.

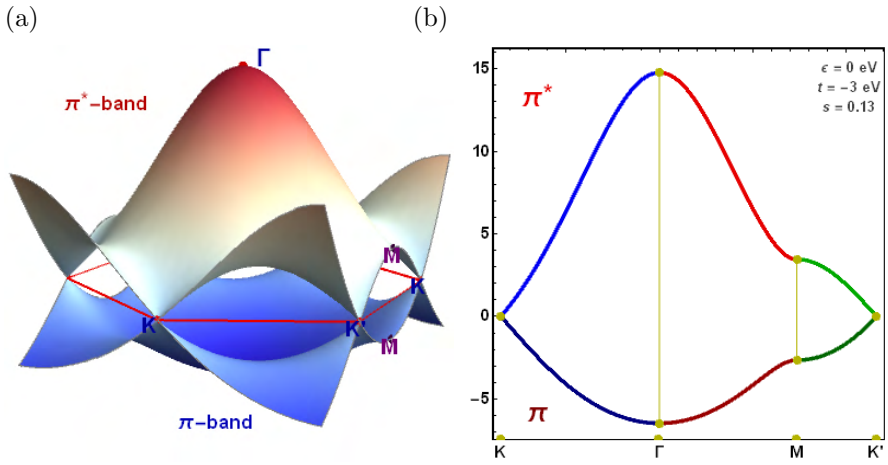

Figure 3.2: (a) Electronic energy dispersion of graphene in the first Brilluoin zone (b) and along high symmetry directions, generated from [62].

Figure 3.3 shows the phonon dispersion relations of graphene. As there are two atoms in the unit cell, there are six phonon branches, three of them acoustic (A) and the other three are optic (O). They are classified as longitudinal (L) when parallel to the wave propagation direction or transverse (T) if perpendicular. Finally, vibrations can be classified as out-of-the plane (o) or in-plane (i); the latter can be omitted when focusing on longitudinal modes. The three acoustic modes (LA, iTA, oTA) and two optical modes (LO, iTO) are degenerate at the high symmetry Γ point.

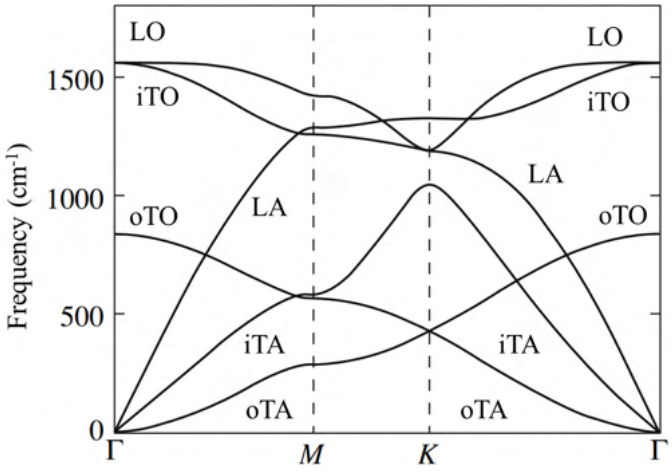

Figure 3.3: Phonon dispersion relations of graphene along high symmetry directions of the first Brilluoin zone, adapted from [63].

3.2 Electronic Properties of Single-Walled Carbon Nanotubes

Single-walled carbon nanotubes (SWCNTs) are long tubular strips of honeycomb carbon, which forces the electronic wavefunction into standing waves around the tube's diameter.

In general, the electronic properties of SWCNTs depend on the orientation of the graphene lattice along the axis and on the diameter of the tube. In order to take both parameters into account, we define the **chiral vector ($\vec{C}_h$)** as the vector perpendicular to the tube's axis:

$$\vec{C}_h = \mathrm{n}\vec{a_1} + \mathrm{m}\vec{a_2} \equiv (\mathrm{n}, \mathrm{m}) \qquad 0 \leq \mathrm{m} \leq \mathrm{n} \tag{3.3}$$

with $|\vec{C}_h|$ equal to the tube's circumference. With the scalar indices (n, m) it is possible to calculate the diameter d_t:

$$d_t = \frac{|\vec{C}_h|}{\pi} = \frac{a}{\pi}\sqrt{(\mathrm{n}+\mathrm{m})^2} \tag{3.4}$$

and the angle θ between $\vec{a_1}$ and $\vec{C}_h$:

$$\tan\theta = \frac{\sqrt{3}\mathrm{m}}{\mathrm{m}+2\mathrm{n}} \tag{3.5}$$

Therefore, a SWCNT can be uniquely characterized either by the scalar indices (n, m) or by d_t and θ. SWCNTs with $\theta = 0°$ are classified as *zigzag* (m = 0), those with $\theta = 30°$ are called *armchair* (m = n), while those with intermediate values of θ are classified as *chiral* (0 < m < n). Examples of ball-and-stick models for nanotubes with diameter ∼0.8 nm are in figure 3.4.

The unit lattice cell of a SWCNT can be defined using $\vec{C}_h$ and the **translation vector** $\vec{T}$:

$$\vec{T} = t_1\vec{a_1} + t_2\vec{a_2} \qquad \vec{C}_h \cdot \vec{T} = 0 \tag{3.6}$$

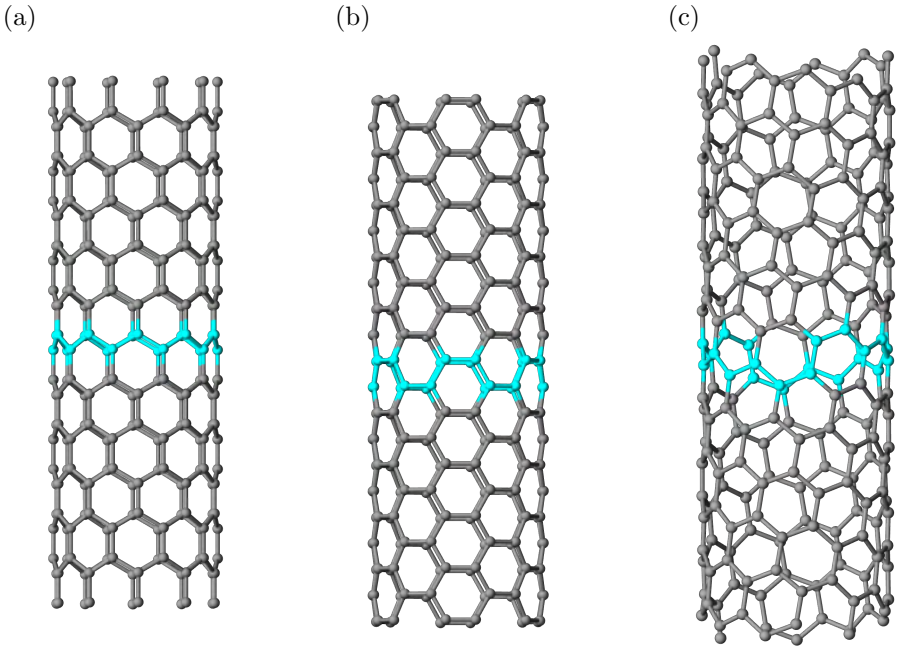

Figure 3.4: Ball-and-stick models of single-walled carbon nanotubes with diameter ∼0.8 nm: (a) (10,0), zigzag SWCNT; (b) (6,6), armchair SWCNT; (c) (9,2) chiral SWCNT.

The indexes t_1 and t_2 are related to the nanotube's indexes:

$$t_1 = \frac{(2\mathrm{m} + \mathrm{n})}{d_r} \qquad t_2 = -\frac{(2\mathrm{n} + \mathrm{m})}{d_r} \tag{3.7}$$

where d_r is the greatest common divisor of

$$d_r = \gcd(2\mathrm{m} + \mathrm{n}, \mathrm{m} + 2\mathrm{n}) \tag{3.8}$$

As an example, in figure 3.5, $\vec{C}_h$, θ and $\vec{T}$ are drawn for a (4,2) SWCNT, which is one of the smallest stable freestanding CNT, along with its ball-and-stick sketch.[64, 65]

The reciprocal space vectors corresponding to $\vec{C}_h$ and $\vec{T}$, $\vec{K}_1$ and $\vec{K}_2$, are found with the usual definition and the orthogonality condition:

$$\vec{C}_h \cdot \vec{K}_1 = \vec{T} \cdot \vec{K}_2 = 2\pi \qquad \vec{C}_h \cdot \vec{K}_2 = \vec{T} \cdot \vec{K}_1 = 0 \tag{3.9}$$

Since $\vec{K}_1$ corresponds to $\vec{C}_h$, the reciprocal space is quantized along its direction, which creates "cutting lines" on the electronic dispersion of graphene, whose length and direction are given by $\vec{K}_2$ (see figures 3.6a and b).

If the cutting lines cross the K point of graphene, the SWCNT has a metallic behavior (Fig 3.6c). Instead, if the cutting lines do not intercept any K point, the SWCNT has a band gap and is therefore semiconducting.

The electronic behaviour of SWCNTs is tied to their scalar indexes and can be deduced by examining $(2\mathrm{n} + \mathrm{m})/3$, or $(\mathrm{n} - \mathrm{m})/3$, depending on which convention is adopted.

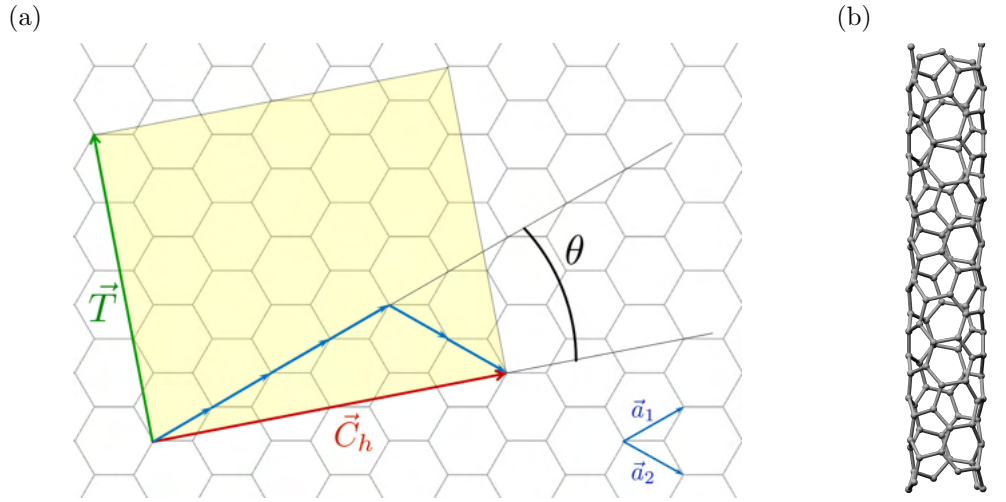

Figure 3.5: (a) Unit cell of an unrolled (4,2) SWCNT, showing $\vec{C}_h$, θ and $\vec{T}$, and b) its ball-and-stick sketch.

If $(2n + m) \in 3\mathbb{N}$, or $(n - m) \in 3\mathbb{N}$, the SWCNT is metallic. In all other cases it is semiconducting, with a further subdivision into Type I and Type II according to the remainder of the division. It is important to note which convention has been adopted, as the semiconducting types are switched according to the quantity used in the division. In this work, I will use the first convention $(2n + m) \in 3\mathbb{N}$.

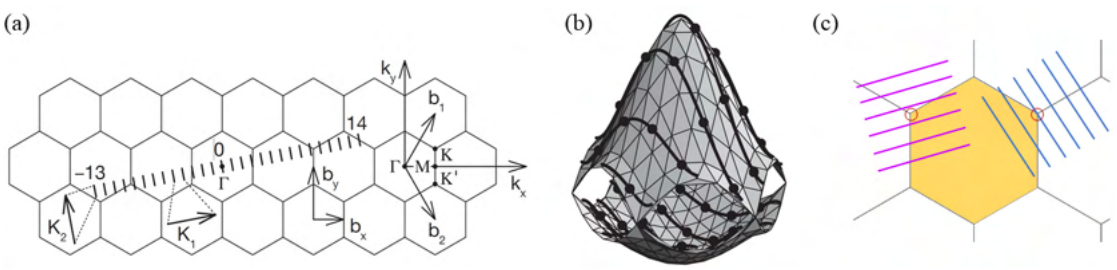

Figure 3.6: (a) Unrolled reciprocal space of (4,2) SWCNT overlapped on reciprocal space of graphene (adapted from [9]). (b) "Cutting lines" for (4,2) on energy dispersion in the Brilluoin zone of graphene (adapted from [9]). (c) Cutting lines in the vicinity of the K points for a metallic (blue) and a semiconducting (purple) SWCNTs.

One third of synthesized SWCNTs are metallic and two thirds semiconducting. The energy gap of semiconducting SWCNTs is inversely proportional to their diameter.[42]

As the electronic properties of SWCNTs are determined by their chirality, so is the density of states (DoS) in their energy levels. SWCNTs are a one-dimensional quantum well, thus peaks appear in the density of states called Van Hove singularities. Optically allowed transitions E_{nn} are those between the n^{th} Van Hove singularities conduction and valence bands (see figure 3.7a). Figure 3.7b shows an excitonic *Kataura plot*, which correlates the computed E_{nn} transition energies to the topological characteristics of the tube, such as diameter or chirality, thus providing a template to identify unknown SWCNTs.[66, 67]

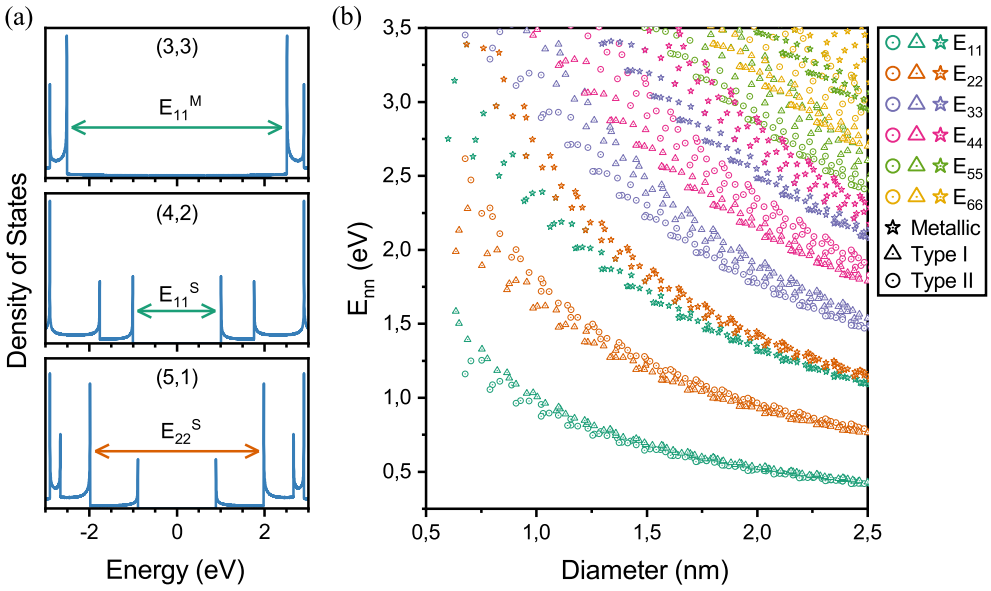

Figure 3.7: (a) Examples of DoS for the smallest allowed SWCNTs: metallic (3,3), type I (4,2), type II (5,1). Adapted from [68]. (b) Theoretical excitonic Kataura plot showing the relation between diameter and allowed optical transitions in SWCNTs.[66, 67]

The exact value of the transition energies depends not only on the chirality, but also on environmental factors such as bundling and chemical environment. Techniques such as optical absorption (OA) and photoluminescence (PL) can be used to determine the experimental values of E_{nn} and improve the theoretical calculations.

3.3 Electronic Properties of Graphene Nanoribbons

Graphene nanoribbons (GNRs) are strips of graphene with extremely large length to width ratios and are thus quantized along their smaller dimension. They are usually classified based on the number N of dimers spanning the width of their unit cell, and on their longitudinal morphology, which can be *zigzag graphene nanoribbon (ZGNR)*, *armchair graphene nanoribbon (AGNR)* or *chiral graphene nanoribbons*, in analogy to SWCNT.[22, 23] The number of carbon atoms in a unit cell is 2N.[9] Examples of GNR topologies are in figure 3.8.

The chiral vector $\vec{C}_h$, defined as in equation (3.3), is parallel to the longitudinal axis and the ribbon edges. $\vec{C}_h$ can also be rewritten as sum of projections in the zigzag and armchair directions:

$$\vec{C}_h = \vec{C}_{h,\mathsf{ZGNR}} + \vec{C}_{h,\mathsf{AGNR}} = (n-m)\vec{a_1} + m\,(\vec{a_1} + \vec{a_2}) \tag{3.10}$$

$\vec{C}_h$ or the chiral angle θ (3.5) provide some information about the edge morphology, but GNR with the same $\vec{C}_h$ can have a different number of of edge atoms N_e and dangling bonds N_d. Thus *minimal edge graphene nanoribbon* are defined with:[69]

$$N_e = N_d = m + n \tag{3.11}$$

to provide unanambiguous identification.

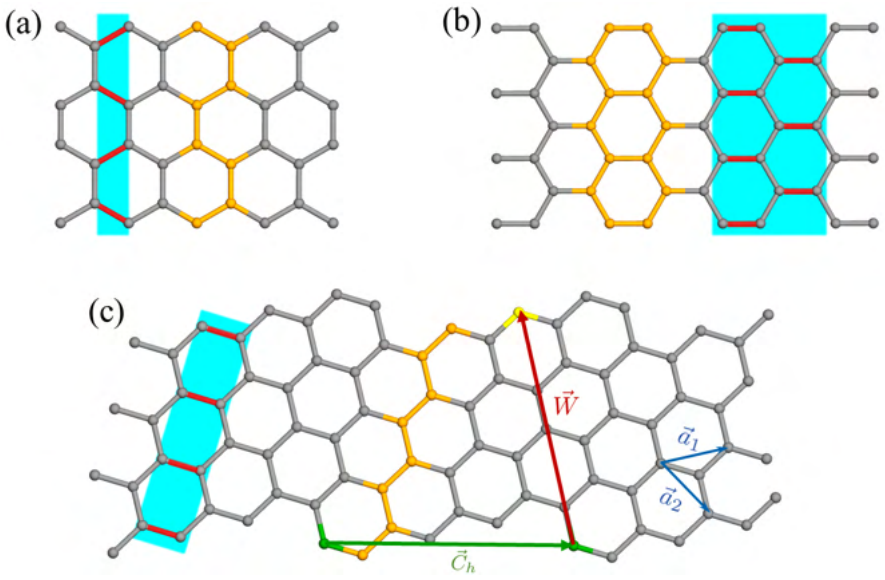

Figure 3.8: (a) N=4 zigzag GNR; (b) N = 7 armchair GNR; (c) N=4 chiral GNR with $\vec{C}_h$ = (3,1) and $w = 2$. The unit cell is highlighted in yellow. The N dimers spanning the width of the unit cell are highlighted in red. (Edge passivation not shown.)

The width of a GNR is defined as the distance between the central points of its outmost dimers. For ideal ribbons, the width depends on N as:

$$W_{\mathsf{AGNR}} = \frac{1}{2}\,(\mathrm{N}-1)\,a \tag{3.12}$$

$$W_{\mathsf{ZGNR}} = \frac{\sqrt{3}}{2}\,(\mathrm{N}-1)\,a \tag{3.13}$$

where a is the lattice constant of graphene (see section 3.1). If N is odd, there is a correspondence between ribbons and nanotubes:

- the width W_{ZGNR} of a N-ZGNR is equivalent to the circumference of an armchair SWCNT with indexes $\left(\frac{N-1}{2}, \frac{\mathrm{N}-1}{2}\right)$;
- the width W_{AGNR} of an N-AGNR is equivalent to the circumference of a zigzag SWCNT with indexes $\left(\frac{\mathrm{N}-1}{2}, 0\right)$.

No equivalent SWCNT exists for even N values.

For a chiral GNR, a width vector can be defined, parallel to the armchair direction of the graphene lattice spanning the unit cell (Fig. 3.8c):

$$\vec{W} = -w\,\vec{a_1} + 2w\,\vec{a_2} \equiv (-w, 2w) \qquad w \in \mathbb{N} \tag{3.14}$$

Thus, the width of a chiral nanoribbon is:[70]

$$W_{chiral} = \sqrt{3} w\, a \cos\theta \tag{3.15}$$

From now on, we will focus only on AGNR and ZGNR, as they provide the most straightforward examples of GNR.

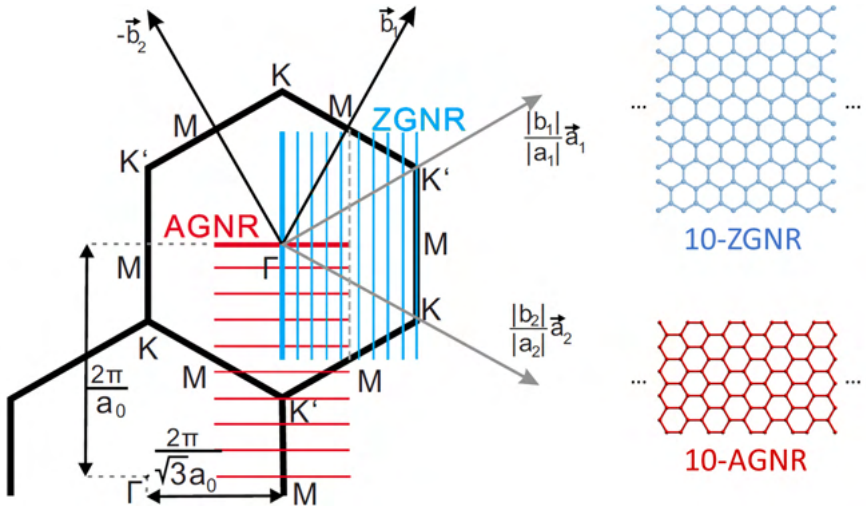

Figure 3.9: Reciprocal lattice of graphene overlapped with the Brilluoin zone of ideal 10-AGNR (red) and 10-ZGNR (green) and their ball-and-stick sketches. Adapted from [71].

Because of confinement along the width, only standing waves are allowed perpendicularly to the GNR's axis. Therefore, the wave vector in this direction is quantized as:

$$\vec{k}_\perp = \frac{n \cdot \pi}{W_{\text{GNR}}} \qquad n = 0, \ldots, \ N-1 \tag{3.16}$$

As a consequence, the Brilluoin zone of GNRs consists in N discrete lines, spaced $\Delta k = \frac{\pi}{W_{\text{GNR}}}$ apart. These cutting lines are parallel to the zigzag direction of the lattice for an AGNR, to the armchair direction of the lattice for a ZGNR (figure 3.9).[71, 72]

GNR can be considered a supercell of graphene unit cells. Thus when their Brilluoin zone is "unfolded" on the phonon dispersion relations of a graphene monolayer, the latter is almost perfectly reproduced by the GNR modes and their overtones (figure 3.10). Interesting is the branch switching occurring in GNR phonon modes at the K point, due to the wave vector rotating 120° between the $\bar{\Gamma K}$ and $\bar{KM}$ directions.

3.3.1 Energy Gap in Graphene Nanoribbons

As a first approximation, the band structure of GNR can be calculated by tight binding and zone folding of the graphene energy dispersion. In this approximation, a flat band appears at the Fermi energy of ZGNRs, while a AGNRs are predicted to be semiconductors except when $\frac{\text{N}-1}{3} \in \mathbb{N}$.[22, 23, 9] However, when the localized states at the edges, which greatly influence the band structure, are taken into account, all GNR are predicted to have a non-zero energy gap. Thus, both *ab initio* calculations and experiments have shown that all nanoribbons are semiconducting with an energy gap depending on the ribbon's width.[38, 73]

Armchair graphene nanoribbons (AGNRs) can be further subdivided into three families[22, 23]

$$N = (3p, 3p+1, 3p+2) \qquad p \in \text{N} \tag{3.17}$$

Fig. 3.11 shows the energy gap E_g for all three families of AGNR predicted from tight-binding and from *ab-initio* local-density approximation (LDA) calculations. While tight-

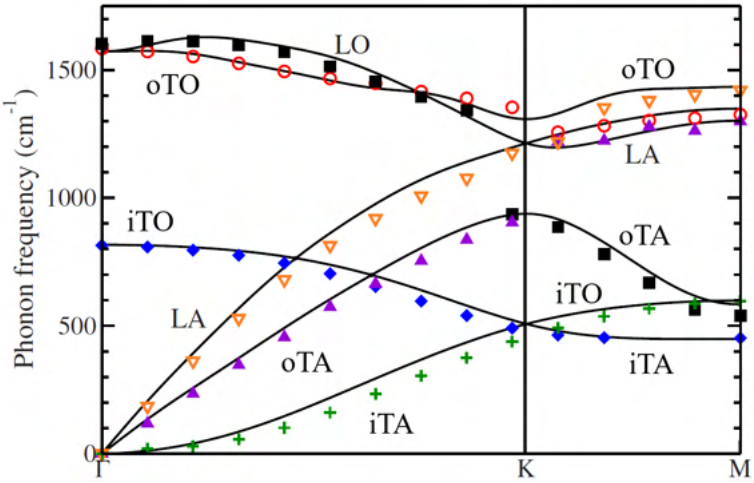

Figure 3.10: Mapping of iTO (filled squares), LO (circles), oTO (filled diamonds), iTA (empty triangles), LA (filled triangles), oTA (crosses) fundamental frequencies and overtones of an 15-AGNR onto calculated phonon dispersion of graphene solid lines. Longitudinal nanoribbon modes correspond to transverse graphene modes. Adapted from [71].

binding predicts that $E_g(3p) \simeq E_g(3p+1)$ and $E_g(3p+2) = 0$, LDA calculations exhibit the following energy gap trend:[38]

$$E_g(3p+1) > E_g(3p) > E_g(3p+2) > 0 \tag{3.18}$$

Thus AGNR of all three families are semiconductors with an energy gap that is inversely proportional to the ribbon width. Experiments confirm the trend from LDA calculations described in equation (3.18), showing that $E_g(3p+2)$ is small but not zero.[74]

The highlighted data represents 5-, 6- and 7-AGNR, all of which in principle have a suitable width to be grown inside 1.4 nm SWCNT from encapsulated small molecules.

Zigzag graphene nanoribbons (ZGNRs) are also direct semiconductors with a bandgap inversely proportional to the ribbon's width. First-principle calculations predict them to have magnetic properties at the edges, with a magnetic insulating ground state and antiparallel spin orientation between opposite edges.[38]

However, the energy gap is underestimated when only density functional theory (DFT) calculations are used. A more accurate theoretical determination of the energy gap requires *ab initio* calculations with the *Green-Coulomb (GW)* approximation, as illustrated in figure 3.12.

When comparing theoretical results with theory, experimental conditions must be taken into account, as presented in figure 3.12. Transport experiments are commonly conducted via scanning tunneling spectroscopy (STS) on metallic substrates, therefore it is necessary to consider the effect of charge transfer due to polarization between GNRs and their substrate, for example using *Image Charge (IC)* corrections. Optical experiments are influenced by the presence inside the material of excitons, interacting electrons and holes. In order to have an agreement between measured and computed optical gap, the binding energy of excitons must be computed with the *Bethe-Salpeter equation (BSE)* and subtracted from the energy gap of a free-standing nanoribbon.[75,

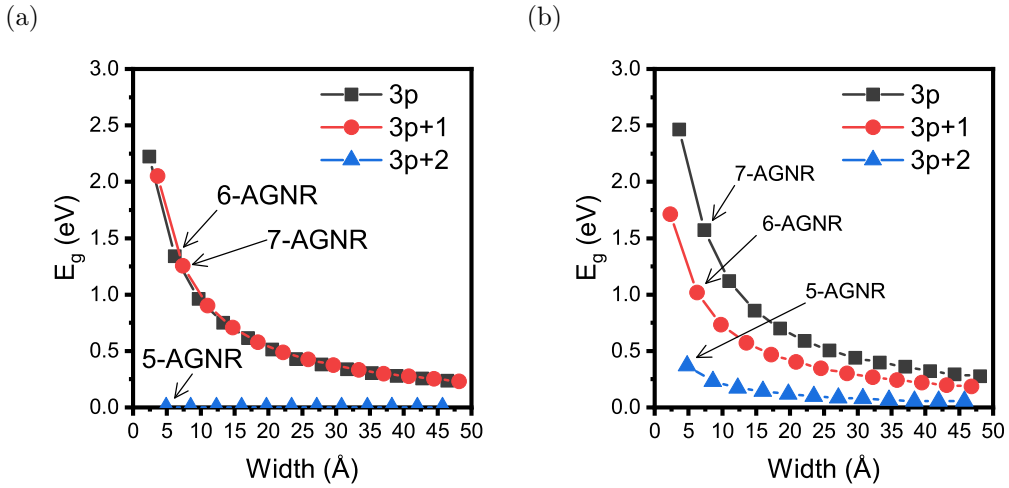

Figure 3.11: Energy gap of the three families of AGNR as a function of width, calculated with (a) tight binding approximation and (b) *ab initio* LDA calculations. Adapted from [38]. AGNR which can in principle be grown inside 1.4 nm SWCNT are highlighted.

76] Excitonic effects are also responsible for optical resonances observed in Raman, OA and PL spectroscopies.[77]

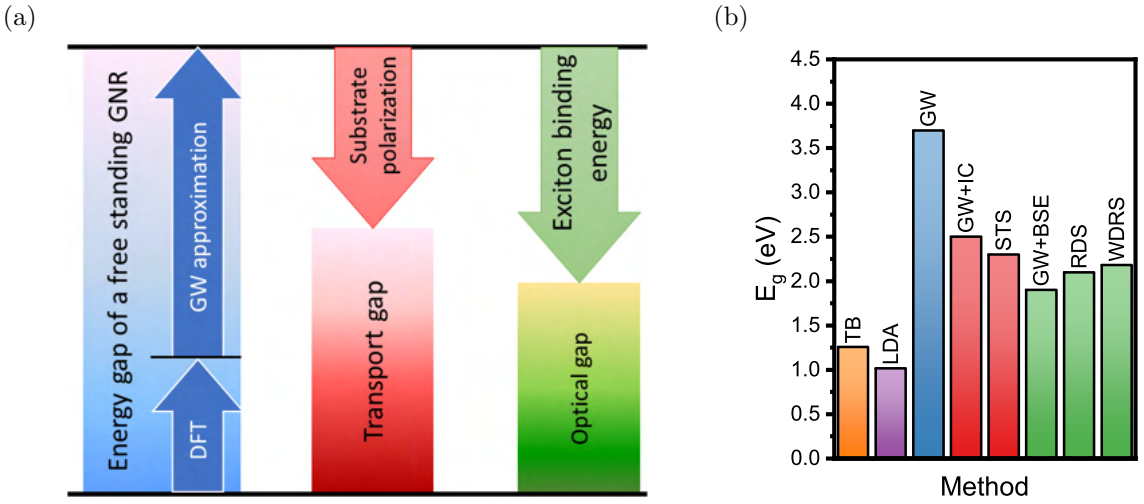

Figure 3.12: (a) Comparison between contributions to *ab initio* calculations of the GNR band gap in vacuum (blue), and the electronic (red) and optical (green) band gaps determined experimentally. Adapted from [76]. (b) Energy gap of 7-AGNR, calculated by TB, LDA, GW, GW corrected for substrate polarization (IC) or excition binding energy (BSE), and determined experimentally by STS, RDS and WDRS.[38, 76]

As an example of how dramatic the differences between estimates are, some calculated and measured values of the energy gap of 7-AGNR are reported in figure 3.12b. The values from figure 3.11 are compared with values reported in *Denk et al.*, in which the gap was calculated via DFT and GW approximation, corrected for substrate polarization

via IC and for excitionic presence via BSE; moreover the transport gap was measured via scanning tunneling spectroscopy (STS) and reflectance difference spectroscopy (RDS). Furthermore, the observed optical gap from *Kuzmany et al.* measured via wavelength dependent Raman spectroscopy (WDRS) is reported.

The GW approximation increases dramatically by about 2.5 eV the energy gap estimate for a free standing GNR. The IC correction lowers the estimate by about 1.2 eV, and is in agreement with experimental values registered with STS. In the same way, BSE correction to yields an optical gap of about 2 eV, very close to the experimental values of 2.1 and 2.18 eV found by RDS and WDRS, respectively.

Therefore, precise tailoring of the final topology provides control over the GNR's electronic and optical properties.

Zig-zag and armchair GNR hybrids have interesting transport properties, leading for example to localized states behaving as massless Dirac fermions or to non-trivial quantum phases at the hybridization junction.[78, 79, 80]

Not only topology but also edge passivation and doping influence the band gap of the ribbon.[24] The edge bonds can be left dangling[73] or terminated with heteroatoms.[81, 17] Heteroatoms can also be inserted in the honeycomb lattice to create localized states[82] or deposited on the GNR to act as charge donors.[83]

Other influences on the band structure are electrostatic interaction with the substrate[75] and physical distortion of GNR geometry, such as lattice relaxation.[84, 85, 86].

Chapter 4

Synthesis of Graphene Nanoribbons

4.1 State of the Art

Since the first theoretical work on graphene nanoribbon in 1994, tailored synthesis of GNR has been an active research topic.

The earliest synthesis trials used a top-down approach, which consists in nanolithography on graphene[87, 88] or on CNT.[89] This technique results in GNR with relatively large widths ($\gtrsim$10 nm) and irregular edge topology.[90]

The study of atomically precise, small-width GNR was made possible by the development of BUS techniques. They allow to atomically tailor the final electronic and optical properties of the GNR by selecting the organic precursor used for the synthesis.[91, 80, 92]

4.1.1 Solution-Mediated Polymerization

One noteworthy BUS method is solution-mediated polymerization. This is a very high yield method which has led to the synthesis of GNR of various topologies with lengths in the order of $\sim$100 nm.[93] Despite these successes, characterization and application of GNR synthesized in solution present challenges due to bulky solubilizing side groups and to their large size, which in turn raises concerns on their structural perfection.[94, 95, 96, 97]

Moreover, ordered deposition on substrates of long macromolecules is a well-known issue in the field of organic semiconductors, whose solutions require a compromise between good alignment and time efficiency.

4.1.2 Chemical Vapour Deposition on Metal Substrates

At the present time, the established high-yield BUS route to obtain atomic-precision GNR is on-surface cyclodehyodrogenation (CDH): a halogenated precursor (e.g. with Br or I atoms) is deposited in ultra-high vacuum (UHV) through chemical vapour deposition (CVD) on a metal substrate, then heat-treated to induce polymerization with Ullmann-like coupling reaction, during which the bond between halogen and precursor molecule is broken and hydrogen halides are formed (e.g. HBr or HI), and finally some of the remaining C-H bonds are endothermically broken leading to hydrogen gas and cyclization of the dangling C-C bonds.

CVD followed by on-surface CDH provides the most control over the morphology of the final product among the established BUS synthesis routes for GNR, which allows to tailor electronic, optical and magnetic properties by choosing the appropriate precursor.[96, 98].

The first reported instance of on-surface CDH was published by *Cai et al.* in 2010.[40] The reaction schemes they used are in figures 4.1a and b, together with STM overviews that confirmed polymerization into GNR in figures 4.1c and d.

During the decade that has elapsed since this breakthrough article, knowledge and expertise in GNR polymerization has grown enough to allow the same group to commence systematic, relatively high yield production of material with a "GNR reactor".[25]

State of the art bottom-up synthesis has led to the production of atomically precise GNR with interesting edge topologies, such as armchair[40], zigzag[73], cove type[99] or chevron shaped GNR.[40, 17] New exotic hybrid structures have been investigated, including GNR with staggered edges or in-line extended edges[80] and GNR syntesized from a sequence of oppositely oriented pyrene subunits (pGNR).[79]

Moreover, GNR with similar topology but different index N can be synthesized or attached together forming a junction, which may prove useful in future technological applications.[18, 100]

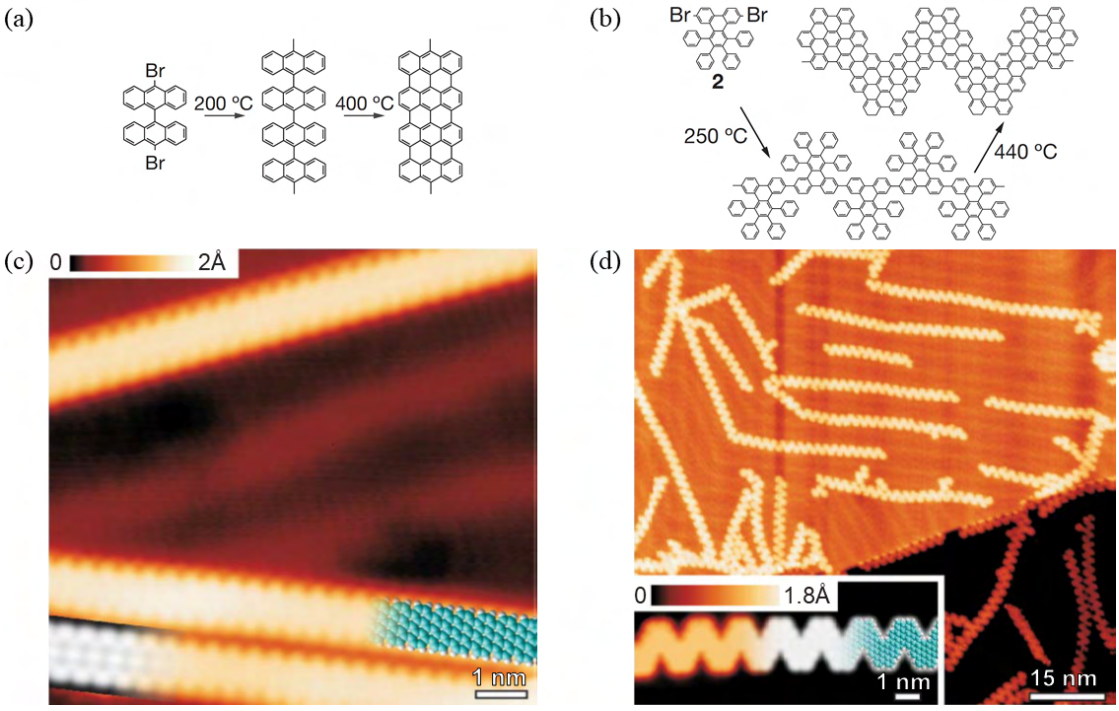

Figure 4.1: First reported on-surface bottom-up synthesis of GNR, adapted from [40]. Reaction schemes from halogenated precursors to (a) 7-AGNR and (b) chevron-type GNR. STM overview after CDH of (c) 7-AGNR and (d) chevron-type GNR.

The metal substrate in on-surface CDH acts both as catalyst for the Ullmann-like coupling reaction and as a two-dimensional template for the final GNR pattern. However, restraining the growth of GNR on metals is not ideal for multiple reasons. Metal substrate hinder the direct measurement of optical and electrical properties of the re-

action products.[75, 98] Moreover, for most of current technological applications GNR-based devices could only operate on insulating substrates. Although GNR synthesized on metals can be transferred to insulating surfaces, the process lowers the quality of the synthesized products significantly.[17, 14, 25] Finally, as the topological characteristics of the GNR strongly depend on the crystalline properties of the metal substrate that is employed during synthesis, it poses a limit to the variety of GNR that may be achieved.

4.2 Metal-Free Synthesis of Graphene Nanoribbons

As described in the previous paragraph, CDH on metal substrates is a pivotal technological breakthrough that has allowed most of experimental studies on GNR in the past decade. Unfortunately, the presence of a metal substrate is now also a practical impediment.

In view of an easier and better characterization and even future industrial applications, it is desirable to decouple the synthesis of GNR from the metallic catalytic substrate. Here I will summarize some of the metal-free techniques currently under study.

4.2.1 Semiconductors as Deposition Substrates

Chemical vapour deposition of carbon precursor such as CH_4 or C_2H_4 on germanium Ge(001) and on germanium-on-silicon Ge/Si(001) has also been used successfully for synthesis of GNR.[101, 102]

However, this method, which is usually employed for bottom-up synthesis of monolayer graphene, allows only marginal control over the GNR width. It is therefore not ideal for tailoring the properties of synthesized GNR.

4.2.2 Cyclodehydrofluorination

One candidate reaction is cyclodehyodrofluorination (CDHF), so called because fluorine is the halogen atom employed in precursors. In the absence of a metal substrate, the fluorine atom acts as catalyst for CDH.

Intramolecular Aryl-Aryl coupling by C-F bond activation in fluorinated aromatic molecules on thermally activated γ-aluminum oxide was found to be very effective for the synthesis of various graphene-like nanostructures by a bottom-up approach.[103, 104, 105, 106, 107]

The CDHF reaction is characterized by high efficiency and high regio- and chemoselectivity.[106, 108] It allowed to synthesize various nanographenes (NGs) in near quantitative yields under mild conditions, including highly strained bowl-shaped systems.[106, 107, 108, 109]

Moreover, virtually linear oligophenylenes bearing fluorine functionalities in defined positions were successfully "rolled up" to the respective target nanographenes in domino-like fashion by tandem cyclization via HF elimination.[110, 111] This oligophenylene zipping approach was also successfully performed directly on a semiconducting rutile titania surface and it was later employed for the synthesis of precisely tailored 7-AGNR, as depicted in figure 4.2.[112, 20]

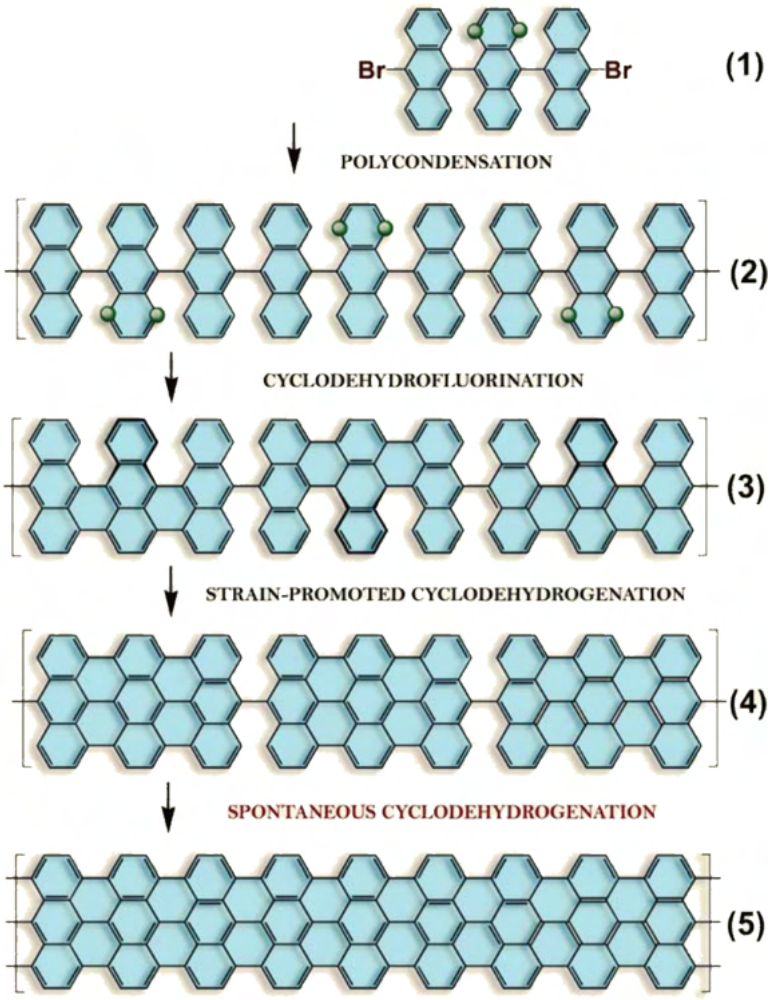

Figure 4.2: Cyclodehyodrofluorination pathway to 7-AGNR, relying on sequential activation of carbon-bromine (C-Br) and carbon-fluorine (C-F) bonds, and subsequent cyclodehyodrogenation. Adapted from [20].

4.2.3 Graphene Nanoribbons encapsulated in Carbon Nanotubes

Another possible approach to eliminate the dependence on metals is the encapsulation of precursors inside single or double wall carbon nanotubes (SWCNT and DWCNT) and synthesis of graphene nanoribbons inside single-walled carbon nanotube (GNR@SWCNT) or in double-walled carbon nanotubes (GNR@DWCNT).

In fact, it has been shown that the chemically inert internal environment of CNT can be used as a nanoreactor to synthesize and stabilize one-dimensional products, such as GNR,[113, 114] inner concentric SWCNT,[115, 116, 117, 118] and long linear carbyne chains.[119, 120, 121, 122] The synthesis of GNR@CNT allows to use virtually any kind of organic precursor small enough to fit inside the SWCNT. The presence of heteroatoms in precursors may allow the final GNR's edges to be terminated and thus more thermodynamically favoured than an inner concentric SWCNT.[113, 123]

The geometry of the encapsulating nanotube influences the final characteristics of the

GNR. In fact, the GNR's width can be selected very precisely by choosing the diameter of the enveloping CNT. The preferred width for an encapsulated GNR is slightly bigger than the encapsulating SWCNT's diameter. Because of this, the SWCNT's section is deformed into an oval and the GNR assumes a helical twist. [113, 124]

The similarity between precursors' widths and encapsulating SWCNT's diameters has been shown to strongly influence the yield of GNR@SWCNT. It is thought that if the two are similar enough, the distortion of the nanotube's section caused by the first encapsulated precursor molecules forces the alignment of all other following molecules, thus facilitating the polymerization into planar nanocarbons. The alignment can't happen if the SWCNT diameter is too big, while van der Waals strain prevents encapsulation with too small diameters.[125, 26]

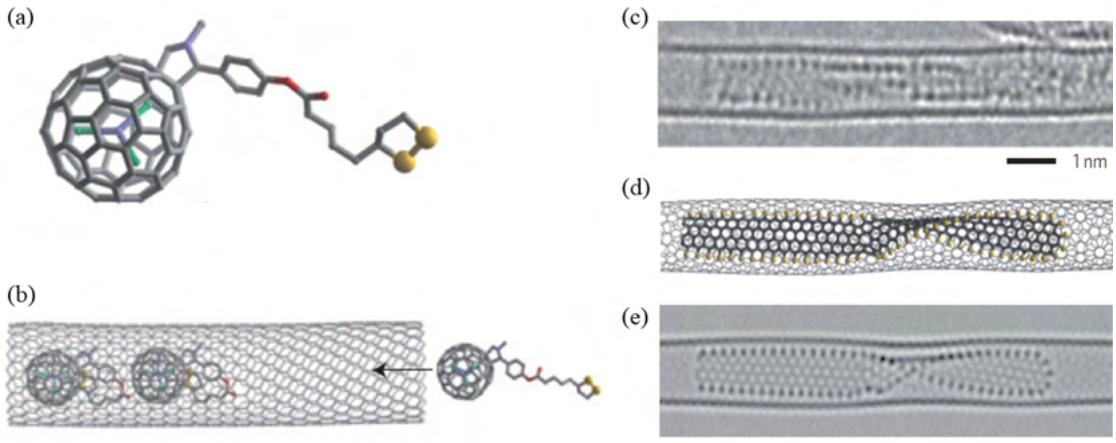

Figure 4.3: First reported synthesis of the hybrid system GNR@SWCNT. Fullerene molecules functionalized with a sulphur containing organic group (a) are encapsulated into host SWCNTs (b). Under irradiation with an electron beam, the functionalized fullerenes decompose and reassemble into GNRs with sulphur terminated edges: (c) experimental AC-HRTEM image, (d), calculated model of S-GNR@SWNT and (d) simulated AC-HRTEM image from the model. Adapted from [113].

Finally, the encapsulated molecule is far more stable under investigation with Raman spectroscopy, as GNR on substrates are quickly destroyed under laser irradiation.[19] This hybrid system allows a fundamental study of the Raman response of the GNR, with beneficial effects such as signal enhancement, as has been reported for encapsulate dyes in single-walled carbon nanotubes (SWCNTs).[126]

The first example of GNR@SWCNT was reported in 2011, when fullerene molecules functionalized with a sulphur containing organic group were encapsulated into host SWCNTs (see figures 4.3a and b). Energy was then supplied to the system by heating or electron bombardment. Encapsulation and synthesis of GNR@SWCNT were confirmed by Raman spectroscopy and aberration-corrected high resolution transmission electron microscopy (AC-HRTEM) (see figure 4.3c). Thermodynamic calculations and modelling of the GNR@SWCNT system demonstrated that the sulphur contained in the precursor terminated the GNR edges (see figures 4.3d and e).

Further experiments have been conducted with a variety of encapsulated precursor, such as perylene or ferrocene. If the precursor already has nanoribbon topology, the expected behaviour is heat induced polymerization into a long GNR. Otherwise, the

precursor has to first decompose and provide matter for nanographenes to form. In this case, the width of synthesized GNR is not uniform and can vary according to other parameters, such as the encapsulating nanotube's diameter.

One such example from *Kuzmany et al.* is in figure 4.4, which reports a two dimensional Raman map of GNR in 1.3 nm SWCNCT grown from encapsulated ferrocene.[26] The strongest resonance is found for 6-AGNR, but also present are nanoribbons of similar width, 7-AGNR and 5-AGNR, though the latter is only visible in overtones. Also present are signals from syntesized inner tubes that form DWCNT. Figure 4.4 makes it clear that the resonance window of GNR is not as wide as that of SWCNT, so using the right excitation energy during Raman spectroscopy is pivotal for investigation into these materials.

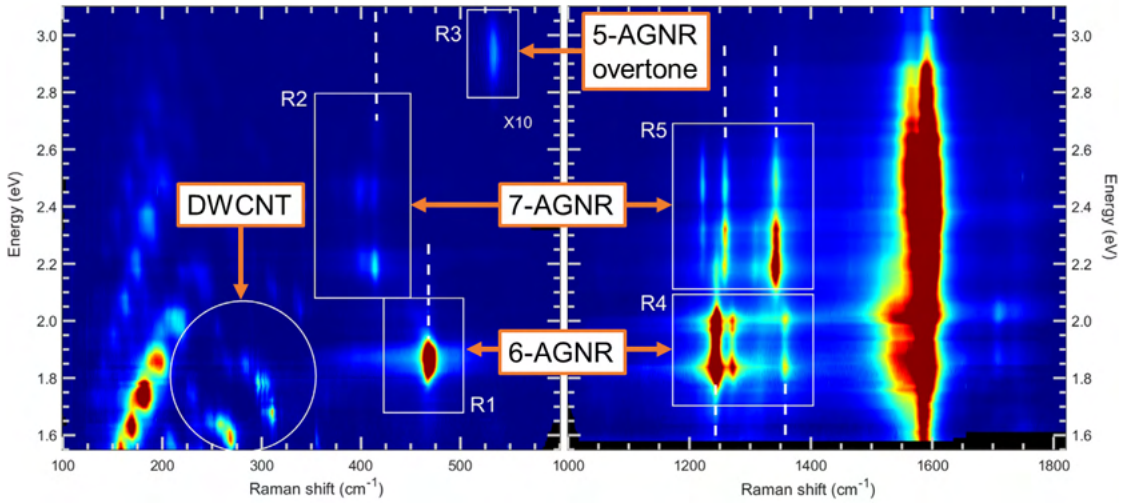

Figure 4.4: Raman map of 6-AGNR and 7-AGNR encapsulated in SWCNT with a mean diameter of 1.3 nm. Adapted from [26].

The encapsulation approach still cannot be applied to semiconductor-based electronic devices since an extraction method for the synthesized GNR has not yet been developed, but reports of successful extraction of materials from SWCNTs give hope for future developments.[21]

Chapter 5

Raman Spectroscopy, an Analysis Tool into Nanocarbons

The description of Raman spectroscopy in this chapter follows in part the books by McCreery *[127], by* Kuzmany *[128] and by* Jorio et al. *[9].*

5.1 Characterization Methods of GNR

The final structure of on-surface prepared GNR is directly confirmed by scanning tunnelling microscopy (STM) and transmission electron microscopy (TEM). However, both methods present setbacks, as the former requires a metallic substrate and the latter a free-standing sample.

As is the case for their parent material graphene, GNR are Raman active and their vibrational modes have extensively been explored both theoretically[71, 129] and experimentally.[40]

Therefore, Raman spectroscopy is nowadays a widespread established method to investigate the properties of GNR by their vibrational fingerprint.[25] It can be used to determine in a contact-free manner the optical band gap together with excitonic effects, the presence of defects, edge morphology and passivation, the width and, in limited cases, the length of a GNR.

5.2 General Description of Raman Spectroscopy

Raman spectroscopy is an experimental technique that allows to investigate the vibrational properties of photoexcited materials. It was first observed in 1928 and named after one of its discoverers, Chandrasekhara Venkata Raman.[130] In recent years, Raman spectroscopy has found application in the study of organic materials because it is a contactless, fast method to characterize carbon-based samples.

5.2.1 Theoretical Description of Raman Spectroscopy

For a classical description of the Raman effect, let us analyze the interaction between a generic molecule and a photon $h\nu_0$ with electric field:

$$\mathbf{E} = \mathbf{E}_0 \cos(2\pi\nu_0 t) \tag{5.1}$$

The interaction between a generic electric field **E** and a molecule induces changes in the latter's polarization **P**, proportional to the molecule's polarizability tensor α[1]:

$$\mathbf{P} = \alpha \mathbf{E} \tag{5.2}$$

This will originate vibrations in the molecule's electric field. To describe them, we use the normal modes of molecular vibrations Q_j:

$$Q_j = Q_j^0 \cos(2\pi\nu_j t) \qquad j \in \mathbb{N}, 1 \leq j \leq (3N-6) \tag{5.3}$$

for a generic molecule with N atoms.

The polarizability is therefore a function of Q_j. For small changes of α its Taylor expansion is:

$$\alpha = \alpha_0 + \left(\frac{\partial \alpha}{\partial Q_j}\right) Q_j + \dots \tag{5.4}$$

Using these equations and the trigonometry relation $\cos a \cos b = [\cos(a+b) + \cos(a-b)]/2$, we find the first order expansion of polarization:

$$\mathbf{P} = \alpha_0 \mathbf{E}_0 \cos(2\pi\nu_0 t) + \mathbf{E}_0 Q_j^0 \left(\frac{\partial \alpha}{\partial Q_j}\right) \frac{\cos(2\pi(\nu_0+\nu_j)t) + \cos(2\pi(\nu_0-\nu_j)t)}{2} \tag{5.5}$$

Classically, polarized electrons radiate photons with energies proportional to their oscillation frequency. Therefore light will not only be elastically re-emitted at frequency ν_0, but also inelastically at $\nu_0 \pm \nu_j$. The elastic process is called **Rayleigh scattering**. The inelastic processes are referred to as **anti-Stokes** and **Stokes scattering**, for a higher and lower energy emitted photon, respectively.

Raman spectroscopy observes the inelastically scattered photons. Only modes where $\left(\frac{\partial \alpha}{\partial Q_j}\right) \neq 0$, which therefore cause changes in the polarizability tensor, can be Raman active.

During a Raman active transition, an electron is scattered to a higher energy virtual state by the incoming photon. It is then scattered by one or more phonons inside the material and decays radiatively. This process can be visualized conceptually as an electronic transition that starts in the ground state and ends in a vibrational energy state (Stokes scattering) or viceversa (anti-Stokes scattering), as represented in figure 5.1.

5.2.2 Resonance Raman Scattering

Raman transitions usually have a low probability, as an electron is excited to a virtual state, a short lived perturbation in the electron distribution, before its radiative decay.

However, if the exciting photon energy $h\nu_0 = E_0$ is close to that of an electronic transition E_t, which is usually in the near infrared/optical range, the transition probability is enhanced by a factor 10^3 to 10^5; this is called **resonance Raman**.

Its intensity is a function of E_0 and E_t, yielding the Raman excitation profile:

$$I(E_0) = \left| \frac{A}{(E_0 - E_t - i\Gamma) \cdot (E_0 - (E_t \pm E_q) - i\Gamma)} \right|^2 \tag{5.6}$$

where E_q is the energy of phonons scattered during the transition and Γ is the resonance window width, related to the lifetime of the photoexcited states.

[1] In three dimensions, the polarizability α is a 3x3 symmetric tensor.

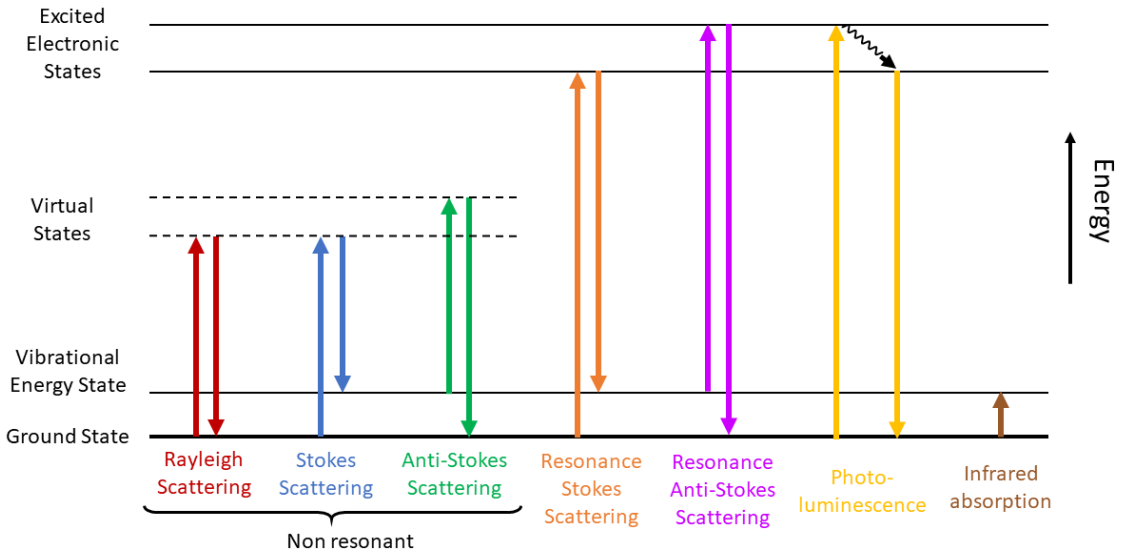

Figure 5.1: Conceptual image of Raman active transitions (resonant or non-resonant Stokes and anti-Stokes scattering) and their competitive phenomena (Rayleigh scattering, photoluminescence, infrared absorption).

5.2.3 Competitive Spectroscopic Phenomena

Other spectroscopic phenomena compete with Raman emission, hindering its observation.

Elastic or Rayleigh scattering, the zero order expansion of polarization in equation 5.5, is 10^{10} times more common than inelastic scattering such as Raman phenomena. It can be removed from Raman spectra using monocromators or the proper band-pass filters.

The main competitive non-elastic effect is **infrared (IR) absorption**, which is 10^{10} times more likely a phenomenon than Raman scattering. During this process, a photon is absorbed to promote an electron from the ground state to a higher energy vibrational state. While Raman active transitions require changes in the polarizability tensor, a transition is only IR active if the polarization vector $\mathbf{P}$ is modified.

Another competitive phenomenon is **fluorescence**, which is a photoluminescence effect with lifetime shorter than 10^{-5} s. In this process, the emitted photon has a lower energy than the incident photon because of photonic non-radiative relaxation prior to emission. This is not a scattering process and it can be several orders of magnitude greater than Raman effect.

Spectroscopic transitions related to Raman scattering and its competitive processes are depicted in figure 5.1.

5.2.4 Practical Raman Spectroscopy

Raman spectroscopy requires monochrome illumination in the near infrared (NIR) and optical range with sufficiently high intensity. Therefore, lasers are an ideal light source, as they provide coherent, high-luminosity emission.

As the response of photoexcited materials depends on exciting wavelength, and the resolution depends also on the width of the exciting laserline, the selection of proper

laser radiation is very important. Common available technology includes *gas lasers* and *semiconducting lasers*, which only emit in limited wavelengths. On the other hand, tunable lasers, such as *dye lasers*, allow to span the whole visible spectrum.

In general, the intensity of inelastically scattered light is much lower in anti-Stokes than in Stokes processes. Therefore, the latter are usually detected, also with the help of a low pass filter to cut away the much more intense elastic scattering.

A Raman spectrometer can be combined with microscope for higher spatial resolution, which in turn can be combined with an atomic force microscopy (AFM) setup to allow for spatial investigation of the sample.

With excessive fluorescence, *Fourier-Transform (FT) Raman* spectrometers can be used. These are Michelson interferometers that use a laser in the NIR, which does not provide enough energy to create an excited electronic state. This means that no fluorescence is present, but also that Raman processes are not in resonance. Fortunately, available NIR lasers provide brightness orders of magnitudes higher than usual optical lasers, which allows detection of Raman signals outside of the resonance window.

Multifrequency Raman Spectroscopy

If a sample is investigated with multiple laser exciting energies, the investigation technique is called multifrequency Raman spectroscopy.

It can be used as a photoselective process to discern between multiple materials present on an sample. In fact, as transition energies E_t are material-specific, it is possible to distinguish different material present in multi-part samples, as each could be resonant with different laser energies.

In the field of nanocarbons, photoselective multifrequency Raman spectroscopy is commonly used in the identification of carbon nanotubes, as optical transitions are chirality dependent.[131]

Laser Annealing

Laser annealing is a process where thermal energy is supplied to a material via irradiation with a laser beam. It provides the advantages of very localized, efficient heating and ease of control, as the amount of thermal energy supplied is determined by laser irradiation. This technique has been used for a very long time in the semiconducting industry for local photo-stimulated crystallization of silicon[132, 133]. Laser annealing can also be applied to organic materials to activate heat-induced transformations, such as the creation of crystalline domains from amorphous materials.[134]

When combined with Raman spectroscopy, this is a powerful, contactless tool to study *in situ* and step-by-step heat-induced reactions. Examples include the synthesis of inner SWCNTs and carbyne chains inside SWCNT and functionalization of potassium-intercalated graphite.[135, 136, 137]

5.2.5 Determination of Local Temperature via Stokes and anti-Stokes Modes

The intensity of Stokes and anti-Stokes Raman lines depends on the population of the ground and excited states. Under thermal equilibrium, the population level can be obtained from the Boltzmann distribution and can be approximated to:

$$\frac{\phi_A}{\phi_S} = \left(\frac{\nu_L + \nu_m}{\nu_L - \nu_m}\right)^A \exp\left(-\frac{h\nu_m}{K_B\, T}\right), \qquad A = 3, 4 \tag{5.7}$$

where ν_L is the exciting laser frequency, ν_m is the mode frequency, T is the temperature, K_B is the Boltzmann constant and h is the Plank constant.[138, 139, 128] The exponent A depends on the detection method used: according to *Gallardo et al.*, $A = 3$ provides more accurate results for photon counting detectors such as charge-coupled devices (CCD), while $A = 4$ is better suited for energy-based detection.[140]

From eq. 5.7, the temperature is:

$$T[K] = \frac{h\nu_m}{K_B}\left[-\log\left(\frac{\phi_A}{\phi_S}\right) + A\log\left(\frac{\nu_L + \nu_m}{\nu_L - \nu_m}\right)\right]^{-1} \tag{5.8}$$

The linewidth of a Raman mode is also dependent on temperature. This dependence is, in the case of a three phonon decay, that is when an optical phonon decays into two acoustic phonons:

$$\Gamma\left(\nu_m, T\right) = \Gamma\left(\nu_m, 0\right)\left[1 + 2\left(\exp\left(\frac{h\nu_m}{2K_B T}\right) - 1\right)^{-1}\right] \tag{5.9}$$

5.3 Raman Spectra of sp^2 Carbon Materials

Raman spectroscopy is a fast and effective method to characterize carbon-based materials. The most prominent spectral features which are present in all Raman fingerprints of graphene-related materials are the G-band, the D-band and the 2D-band. Additional modes arise with shape effects and quantum confinement, such as the radial breathing mode in SWCNT and the radial breathing-like mode in GNR.[141] As an example, the Raman spectrum recorded at 568 nm of a high-purity (9,2) SWCNT sample is depicted in figure 5.2, and that of a 7-AGNR is in figure 5.3.

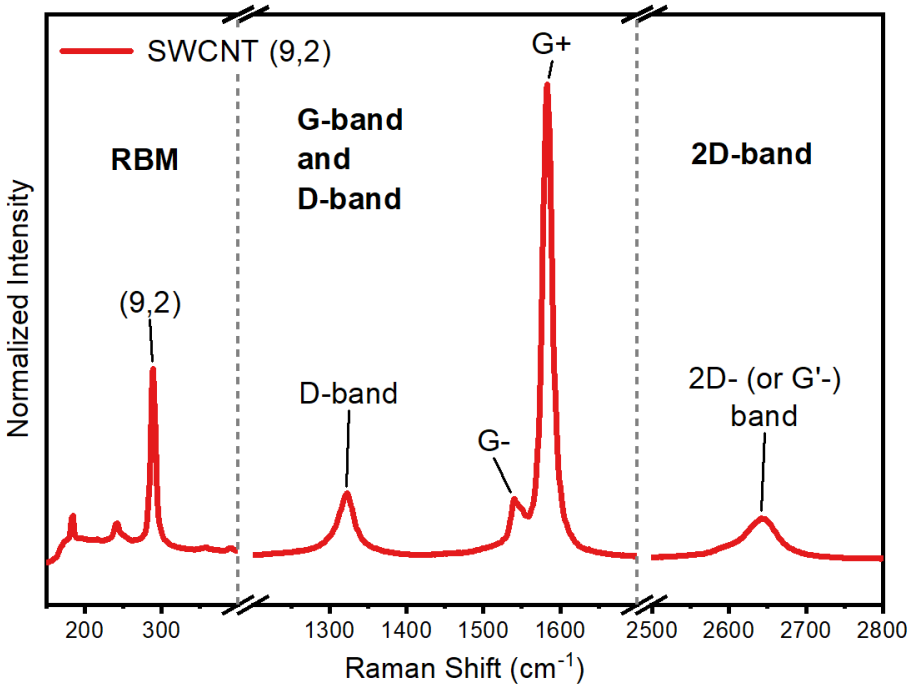

Figure 5.2: Raman spectrum recorded at 568 nm of a high-purity (9,2) SWCNT sample. Typical high intensity SWCNT modes are visible: RBM, D-band, G-band split into G+ and G-, and 2D- (or G'-) mode. Additional peaks in the RBM region are due to slight contamination by other chiralities. Data adapted from [142].

The origin of Raman modes in one-dimensional sp^2 carbon materials can be understood with zone folding applied to the two-dimensional phonon dispersion relations of graphene in figure 3.3, as sketched in figure 5.4 and in the paragraphs below.

5.3.1 Graphene Related Modes

G-Band

The G-band is a first order vibrational mode which is present in all Raman spectra of sp^2 hybridized carbon materials. It is called so because it was first identified in graphite single crystals.[143] It is found at energies around $\sim$1585 cm^{-1}.

This mode originates from LO and iTO branches close to the Γ point, where they are degenerate.

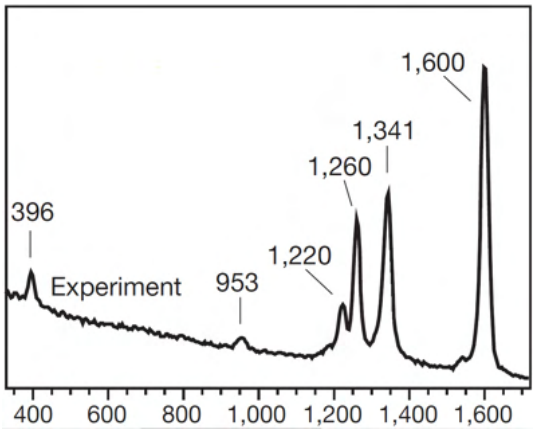

Figure 5.3: Raman fingerprint of a 7-AGNR. Visible Raman modes are the G-band at 1600 cm^{-1}, the RBLM at 396 cm^{-1}, the DLM at 1341 cm^{-1}, and modes related to CH vibrations between 950 cm^{-1} and 1260 cm^{-1}. Adapted from [40].

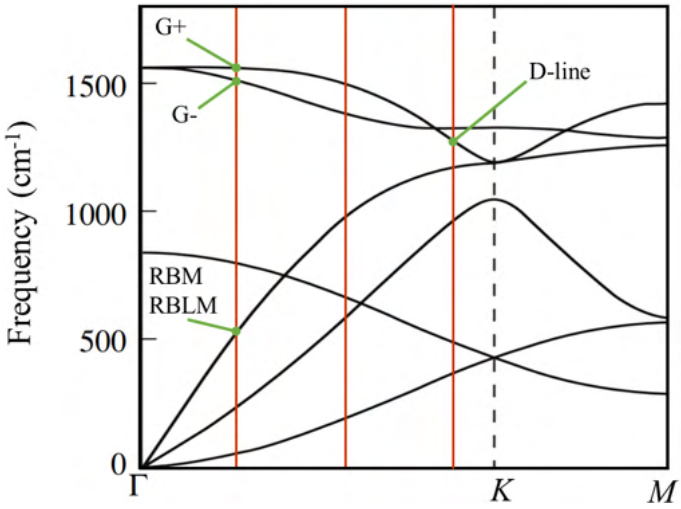

Figure 5.4: Phonon energy dispersion of graphene overlapped with cutting lines due to quantum confinement. Raman active modes for one-dimensional carbon materials can arise at the intersections. Adapted from [76].

Because of quantum confinement in SWCNT and GNR, the degeneracy is broken and the G-band of SWCNT splits into a doublet, as shown in figure 5.2. The G- and G+ modes originate from LO and iTO branches respectively. Their spectral position downshifts with increased strain, thus measuring the wavenumber distance of the splitting provides a way to measure the nanotube's diameter.

D- and 2D- (or G'-) bands

The D-band and 2D-band are second order resonant processes. The first one is observed in the range 1250 to 1400 cm^{-1}, the latter in the range 2500 to 2800 cm^{-1}, as shown in figure 5.2. They are both dispersive modes: their spectral positions shift with the exciting laser wavelength.

The D-band originates from modes on the iTO branch near the K point. In graphene related materials, it reveals the amount of defects present in the honeycomb lattice, such as heteroatoms or holes, but also curvature effects in SWCNT. The presence of the defect is required to enable the optically forbidden vibration.

The 2D-band is also historically called G'-band because it was first identified in the Raman spectrum of graphite single crystals together with the G-band.[143] Contrarily to the D-band, it arises from two-phonon scattering and it is thus always observable, irrespective of the presence of sp^3 defects. In the phonon dispersion relations graph, it originates on the 2iTO branch near the K point.

5.3.2 Additional Modes in One-Dimensional sp^2 Carbon Allotropes

Radial Breathing Mode of Carbon Nanotubes

The radial breathing mode (RBM), so called because it originates from CC vibrations of SWCNT in the radial direction (figure 5.5a), is usually found between 100 and 350 cm^{-1} for diameters between 2.6 nm and 0.7 nm. This mode does not have a corresponding vibration in graphene. The Raman spectral position of the RBM expressed in cm^{-1} can be calculated in a first approximation from the diameter of the SWCNT:

$$\omega_{\mathsf{RBM}} = \frac{A}{d_t} + B \tag{5.10}$$

where the factor $A \cong 227.0\,cm^{-1}\cdot nm$ is a proportionality constant and B is an offset due to van der Waals interactions with the environment.

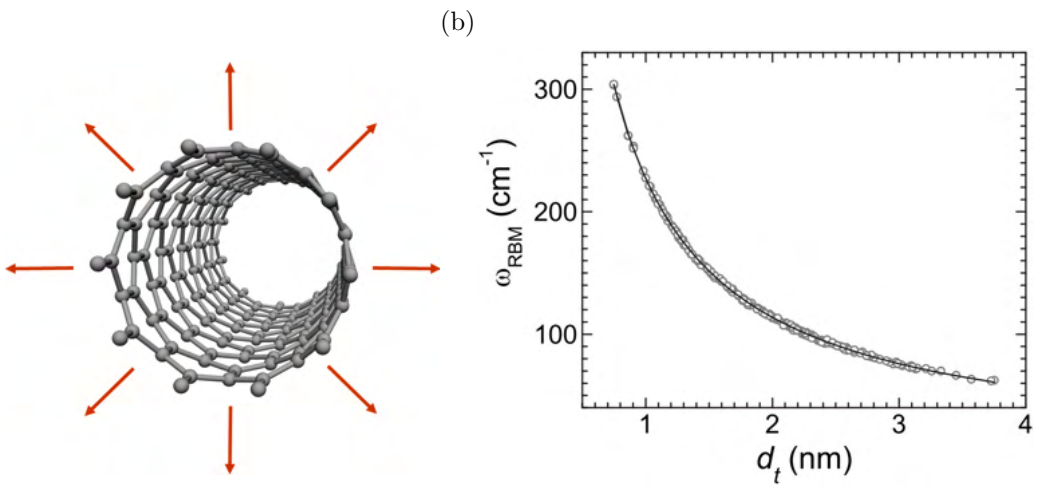

Figure 5.5: (a) Sketch of atomic displacement in a single-walled carbon nanotube (SWCNT) giving rise to the radial breathing mode (RBM). (b) Experimental RBM data as a function of tube diameter d_t. Solid line is a fit of equation 5.10 with $A = 227.0$ and $B = 0.3$. Adapted from [144].

This equation can predict experimental results rather accurately, as reported in figure 5.5b. However, ω_{RBM} should vanish for infinitely large diameters so as to accurately predict graphene values, which is not possible unless B=0. Therefore, a better estimate

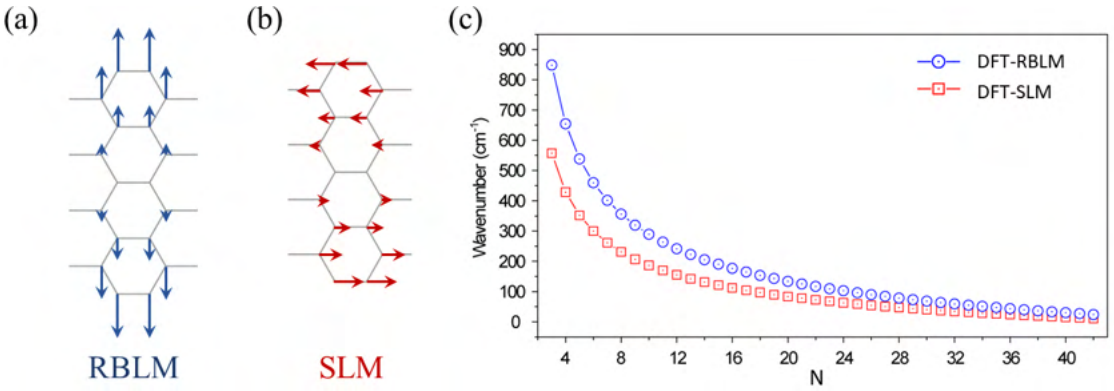

Figure 5.6: Sketches of atomic displacement in a 9-AGNR related to (a) RBLM and (b) SLM. (c) Width-dependent wavenumbers for RBLM and SLM, calculated using density functional theory (DFT). Adapted from [18]

can be made with:

$$\omega_{\mathsf{RBM}} = \frac{A}{d_t}\sqrt{1 + C_e \cdot d_t^2} \tag{5.11}$$

where C_e accounts for effects of interaction with environment.[145]

Therefore, from the spectral position of the RBM (expressed in cm^{-1}) it is possible to calculate the diameter of a SWCNT using the previous equations. For example, the RBM of (9,2) in figure 5.2 is found at 289 cm^{-1}, yielding a diameter of 0.8 nm in agreement with previously reported values.[146, 66, 67]

Radial Breathing-Like and Shear-Like Modes of Graphene Nanoribbons

The radial breathing-like mode (RBLM), so called in analogy to the RBM of carbon nanotubes, is a low energy acoustic mode. It is generated by transversal atomic displacement away from the GNR's long axis (figure 5.6a).

The shear-like mode (SLM) is a lower intensity width-related vibration. It is called so because it originates from shearing longitudinal atomic displacement (figure 5.6b).

Similarly to the RBM in SWCNT, both the RBLM's and the SLM's spectral positions show a dependence on GNR width:

$$\omega = a\frac{1}{\sqrt{W}} + b \tag{5.12}$$

Calculated positions for both modes are reported in figure 5.6c.[147, 129, 148, 18]

Additional GNR modes

The spectrum of GNR is characterized by strong, non dispersive, in-plane bending CH-modes that appear above 1200 cm^{-1}.[40] These modes have been observed also in GNR@SWCNT Raman spectra, as is visible in figure 5.7, in which they are called C_n modes. The $\mathbf{CH}_n$ modes are found between 1200 cm^{-1} and 1400 cm^{-1}.[149, 125] Additional small out of plane CH-modes appear around 800 cm^{-1}.[71]

The CH mode with the highest wavenumber is usually denominated **DLM**. This is an edge-related mode, where the CC bonds give a greater contribution than the termination bonds.[150]

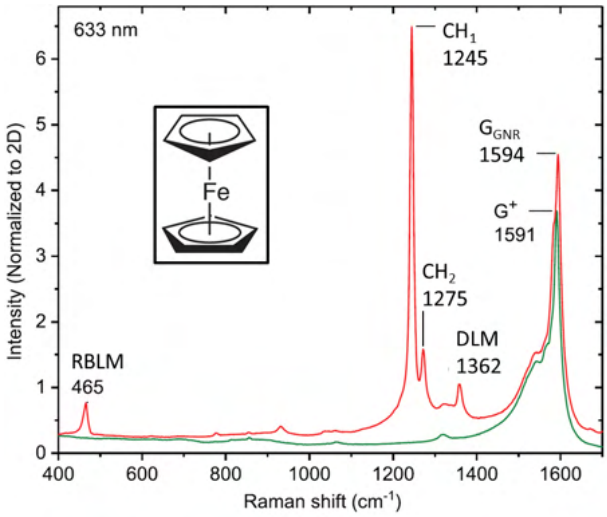

Figure 5.7: Raman modes of transformed ferrocene (molecular sketch in inset) encapsulated in SWCNT: RBLM at 465 cm^{-1}, CH_1 at ∼1245 cm^{-1}, CH_2 mode at ∼1275 cm^{-1}, D-like mode (DLM) at ∼1362 cm^{-1} and G-band at 1594 cm^{-1}. Adapted from [125].

For short GNR, it has been possible to identify a length-related mode, the longitudinal compressive mode (LCM). Atomic displacement is analogous to that of the RBLM. The mode has been observed in the 100 cm^{-1} to 200 cm^{-1} range for GNR shorter than 10 unit cells, and it is predicted to be close to 0 cm^{-1} for infinitely long GNR.[151]

Chapter 6

Experimental Methods

In this Chapter, I will introduce the experimental methods I employed in this work. I will describe sample synthesis and preparation, together with details on the main investigation technique I employed to complete this work, Raman spectroscopy.

6.1 Synthesis of Graphene Nanoribbons

In this work, I used two different approaches to polymerize small molecular precursors into nanographitic structures.

The first one relied on cyclodehyodrofluorination (CDHF) of a small fluorinated precursor, activated by visible light irradiation.

The second approach relied on encapsulation and endothermic polymerization of a small molecule into single-walled carbon nanotubes.

6.1.1 Fluorinated Molecules as Precursors for Graphene Nanoribbons

The fluorinated precursor tetrafluoro-diphenyl-quinquephenyl was synthesised by Dr. Ann-Kristin Steiner and provided by Prof. Konsantin Amsharov.

The fluorinated precursor tetrafluoro-diphenyl-quinquephenyl (TDQ) (ball-and-stick model in figure 6.1a) is pre-programmed for subsequent fourfold cyclodehydrofluorination reaction into heptacene dipyrene, a nanographene (NG), as depicted in figure 6.1b. It was synthesized by Dr. Ann-Kristin Steiner according to the protocol described in *Steiner et al. (2017).*

The total formula of the TDQ is C_{42} H_{26} F_4, its molecular weight is 606,66 g/mol. Its optical gap is in the ultra-violet (UV).[110]

As the CDHF reaction involves synthesis of the corrosive and poisonous gas hydrogen fluoride (HF), any investigation had to be conducted in a sealed environment to be carried out safely. For this reason, the molecule was either sealed inside a glass tube or put in a high vacuum (HV) chamber connected to the fume hood exhaust system.

Finding the Evaporation Temperature of TDQ

As a preliminary investigation, I determined the evaporation temperature of TDQ.

The powdered molecule was inserted into a glass vial connected to a UHV system with an internal pressure better than 10^{-6} mbar. Heating wire was coiled around the vial

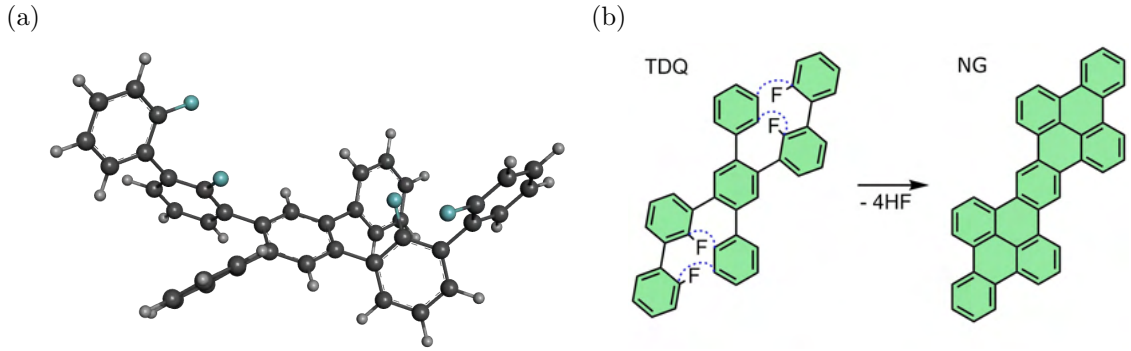

Figure 6.1: (a) Ball-and-stick sketch of tetrafluoro-diphenyl-quinquephenyl (TDQ). (b) TDQ precursor and expected cyclodehydrofluorination into heptacene dipyrene (NG) under ideal conditions [110].

into an home-made heater, which I connected to a voltage generator to apply stepwise heating. Each increase in temperature was approximately 10 °C , after which the sample was left to stabilize for about one hour. I monitored the local temperature of the sample with a custom-built thermocouple.

I was able to determine the approximate evaporation temperature of the molecule by observing at which heating temperature TDQ crystals formed in a condensation ring just outside the coil heater.

Experimental Setup

The cyclization of TDQ was investigated using laser annealing. Our setup combined a con-focal microscope Raman system with a tunable wavelength laser and a small vacuum chamber with a gas inlet connected to an argon gas reservoir.[136, 137] The Raman laser was focused on the sample inside the vacuum chamber through an optical window. The annealing was performed by supplying thermal energy via laser irradiation.[135]

For preliminary determination of the best wavelength to be used, in order to prevent evaporation the vacuum chamber was filled with Ar until a pressure of about 950 mbar was reached.

A small amount of TDQ molecule was deposited on an TEM gold grid support covered in amorphous carbon and brought into HV ($\sim 10^{-6}$ mbar). The sample was then heated with visible laser irradiation at 568 nm, 8 mW of power, irradiance of (1.6×10^4) W cm^{-2}. We collected the inelastically scattered radiation in 180° backscatter geometry to perform concomitant *in-situ* Raman spectroscopy on the sample. During laser annealing, the HV chamber was kept at a pressure better than 10^{-7} mbar. A sketch of the setup used for laser annealing is in figure 6.2.

For the measurement of the Stokes and anti-Stokes processes, the precursor was sealed in vacuum better than 10^{-6} mbar in a pyrex glass vial with square cross section. From this measurement we were able to correlate Raman linewidths with temperature and calculate the temperature evolution during the laser annealing process.

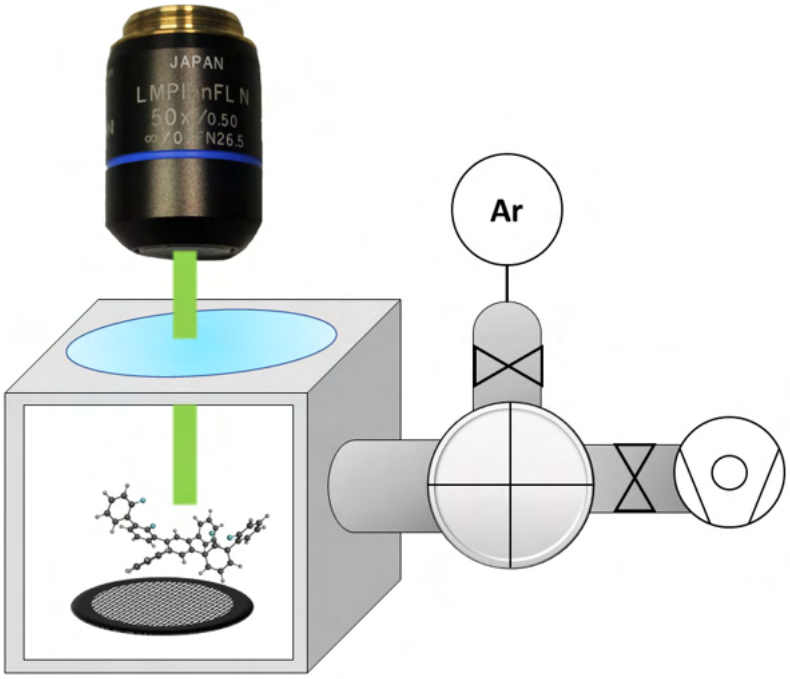

Figure 6.2: Sketch of the UHV setup for laser annealing on TDQ. A small amount of TDQ molecule was deposited on an TEM gold grid support covered in amorphous carbon. The small vacuum chamber with a gas inlet connected to an argon gas reservoir and to a turbopump.

6.2 Small Molecule Encapsulation in SWCNT

SWCNT used in this experiment were syntesized and put into bucky paper form by my colleague Weili Cui in the laboratory of Prof. Yanagi Kazuhiro.

In this section, I describe my investigation into **terrylene** encapsulation inside metallicity separated semiconducting SWCNT with a narrow diameter distribution around 1.4 nm.

SWCNTs with a mean diameter of 1.4 nm were synthesized by discharge method by my colleague Weili Cui in the laboratory of Prof. Yanagi Kazuhiro. Semiconducting SWCNT with a narrow diameter distribution around 1.4 nm were selected by density-gradient ultracentrifugation (DGU) using sodium dodecyl sulfate (SDS) as gradient material according to the existing protocol, and deposited into bucky paper form.[152] A picture of these SWCNT after dispersion into D_2O for optical investigation is in figure 6.5d.

Molecules in the family of rylene nanoemitters are an obvious choice as precursor molecule, since they already have the structure of a very short 5-AGNR. The shortest members of this family, perylene, terrylene and quaterylene, are respectively made of two, three and four unit cells of 5-AGNR. Their molecular structure is in figure 6.3.

The shortest, perylene, is the most easily commercially available of the three. However, due to their short length, perylene molecules have been observed to stack at an angle to the encapsulating SWCNT's axis, which hinders polymerization into GNR.[153]

Therefore, in this contribution I used the longer molecule from the rylene family, terrylene. It has the same 5-AGNR structure, but its length prevents stacking effects and forces it to align parallel to the axis of 1.4 nm diameter SWCNT used for encapsulation, which facilitates polymerization.

SWCNT in the form of bucky paper were opened by heating in air at 450 °C for thirty minutes.[154]

The opened SWCNT bucky paper and terrylene dye were sealed inside a borosilicate glass vial at an internal pressure of 10^{-7} mbar. The vial was kept at 350 °C for 455 h (19 days) in a tube furnace. A schematics of the encapsulation process is in figure 6.4.

As a side product, small amounts of van der Waals terrylene crystals formed on the inner walls of the vial. A photo of the crystals taken with an optical microscope is in figure 6.5a.

A common issue in synthesis of GNR@CNT is the excess precursor molecules which remains attached to the outside of the nanotube walls, which interferes with the characterization of encapsulated structures.[114] Most can be removed by washing with a solvent, however the final mono-layer on the outside is very hard to remove, since it has a much higher evaporation temperature than its non-bonded counterpart.

In order to remove excess terrylene material on the outside of the SWCNT, I washed the filled bucky paper multiple times with dichloromethane (DCM). The suspension of terrylene dispersed in DCM has a bright pink color, as visible in figure 6.5c. The washing procedure consisted in a first soak overnight in DCM, then rinsing the sample with 2 ml DCM five consecutive times, until the solvent remained colorless. Both soaking overnight and rinsing were repeated a second time.

Raman spectra gathered before and after the washing procedure in figure 6.6 show a dramatic increase in signal-to-noise ratio and a quenching of fluorescence, which indicates that excess terrylene was successfully removed. However, the last mono-layer may still be present.

After encapsulation inside SWCNTs, terrylene molecules were polymerized with heat treatment forming 5-AGNR. Optical and microscope investigation shows growth of long GNR at the filling temperature of 350 °C , which is consistent with reported values.[155]

Afterwards, the filled SWCNT was cut into smaller samples, such as the one depicted in the optical microscope photo in figure 6.5b. Each them was annealed in vacuum better than 10^{-5} mbar for two hours, each at a different temperature between 400 °C and 800 °C with 50 °C steps. Additionally, temperatures of 1300 °C and 1550 °C were used to confirm filling by providing enough thermal energy for the formation of double-walled carbon nanotubes. A photo of the mixed UHV and furnace setup I used for sample annealing under vacuum is in figure 6.7.

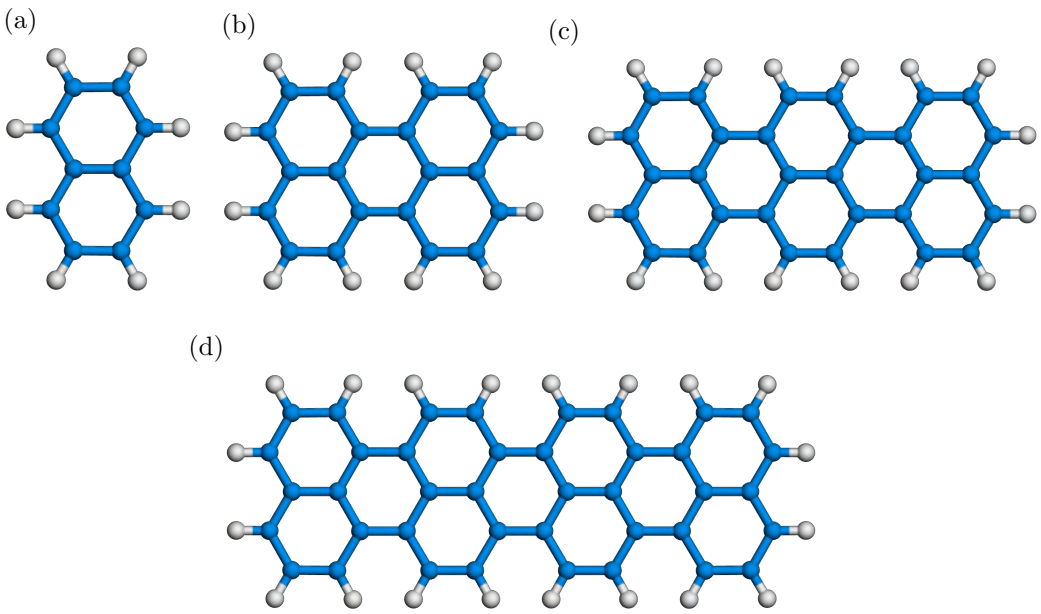

Figure 6.3: Molecular structure of rylene nanoemitters: (a) a rylene dye unit cell, which is also the unit cell of 5-AGNR; (b) perylene with a length of 2 unit cells; (c) terrylene with a length of 3 unit cells; (d) quaterrylene with a length of 4 unit cells.

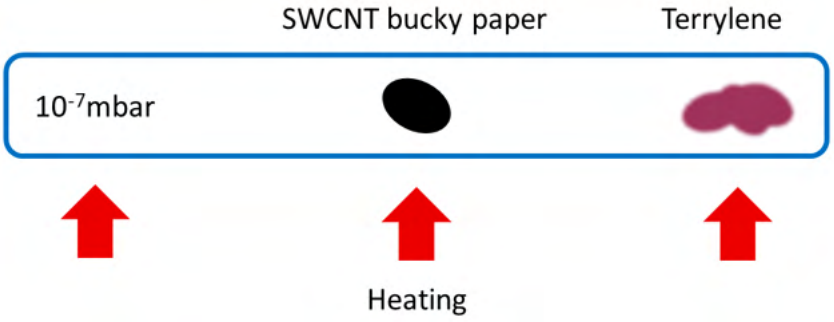

Figure 6.4: Schematics of the setup for encapsulation of terrylene inside SWCNT. Opened SWCNTs in the form of bucky paper were sealed together with terrylene in a quartz vial with internal vacuum at room temperature better than 10^{-7} mbar. The vial was then kept at 350 °C for 455 h (19 days) in a tube furnace.

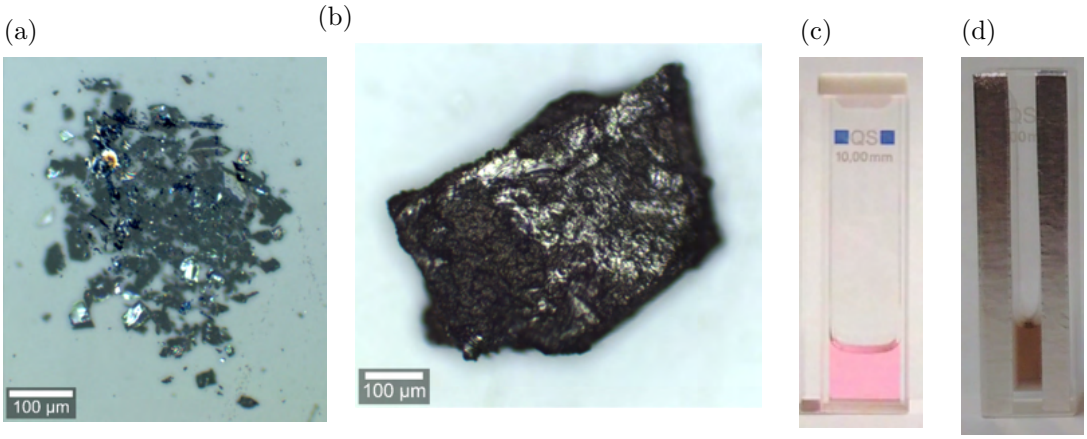

Figure 6.5: (a) Optical microscope image of van der Waals terrylene crystals formed as a side product of the encapsulation procedure. (b) Optical microscope image of one bucky paper sample after filling, washing and annealing under vacuum for two hours. (c) Terrylene dispersed in dichloromethane (DCM) inside an optical cuvette. (d) Semiconducting metallicity sorted SWCNTs in 2% weight DOC in D_2O with typical coloring inside an optical capillary cuvette.

6.3 Raman Spectroscopy

A key expertise of the research group Electronic Properties of Materials, where I have conducted this work, is Raman spectroscopy. It is a powerful optical tool for the investigation and characterization of graphene-related materials. Several complementary spectrometers for multifrequency resonance Raman spectroscopy including the corresponding lasers are available to the research group. The systems I used for the work described in my thesis are listed below

Horiba Jobin Yvon LabRAM HR

Horiba Jobin Yvon LabRAM HR is a multi-frequency Raman microscopy system with multiple Rayleigh filters available. The system was modified and adapted for multi-frequency use[156, 157]. A photo of the setup is depicted in figure 6.8. The backscattered Raman fingerprints are recorded by a liquid N_2 cooled CCD. The resolution is laser dependent, but it is in general between 2 and 3 cm^{-1}. Unless otherwise specified, all the measurements were done at ambient conditions with a 50× objective (about 2 μm laser spot), a 1000 μm hole, a 100 μm slit, and a 600 gr/mm grating. Two external lasers are coupled to the system, namely a He-Ne laser ($\sim$ 633 nm) and a multiwavelength Ar+/Kr+ laser (Coherent Innova 70C, available wavelengths $\sim$ 458, 488, 515, 531, 568, 647 nm).

The laser power for all wavelengths was kept at 1 mW for the measurements of GNR@SWCNT, while the laser annealing of TDQ was executed at 8 mW. The measurements were done as follows: a camera connected to the microscope was used to visually focus on the sample, and then a series of continuous measurements with acquisition time between 1 s and 10 s were made to find maximum signal intensity. The final measurements were done in single window mode for laser annealing and multi-window mode for

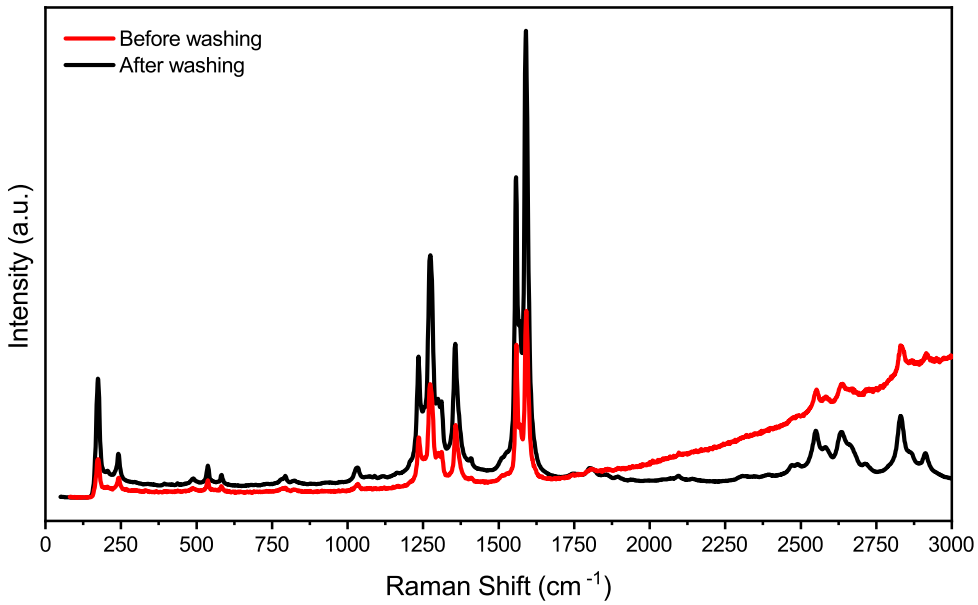

Figure 6.6: 568 nm Raman spectra of terrylene after encapsulation in 1.4 nm semiconducting CNT, before and after washing with DCM. Spectra recorded with 1 mW laser power and normalized to the exposition time.

all other measurements.

Horiba T64000

The Horiba T64000 is a triple grating spectrometer confocal Raman system with 1800 gr/mm grating. A photo of the setup is depicted in figure 6.9. Raman signals in a 180° backscattering geometry are recorded by a liquid N_2 cooled CCD. This setup allows the measurement of Stokes and anti-Stokes signals. Within the scopes of this work, the system was coupled with a diode laser emitting at 532 nm.

Brucker Fourier Transform Infrared Raman Spectrometer RFS 100

A Brucker Fourier Transform Infrared Raman (FT-IR) Spectrometer RFS 100 was used to record the Raman fingerprint of TDQ and its target NG without background fluorescence. The spectrometer is coupled with a Cobolt 05-01 high power single frequency CW diode pumped laser source emitting at a wavelength of 1064 nm. The measurements were taken with the samples deposited on a supporting quartz optical slide. A photo of the system is in figure 6.10.

WiTech Alpha 300A AFM/Raman System

Finally, I used a WiTech Alpha 300A high-resolution combined atomic force microscopy (AFM)/Raman system for the non-destructive characterization of nanostructures, available at the Faculty Center for Nanostructure Research of the University of Vienna. Samples are placed on a digital *xzy* micrometer stage. The backscattered signal is recorded by a Peltier cooled CCD. A photo of the system is in figure 6.11. This setup is used for

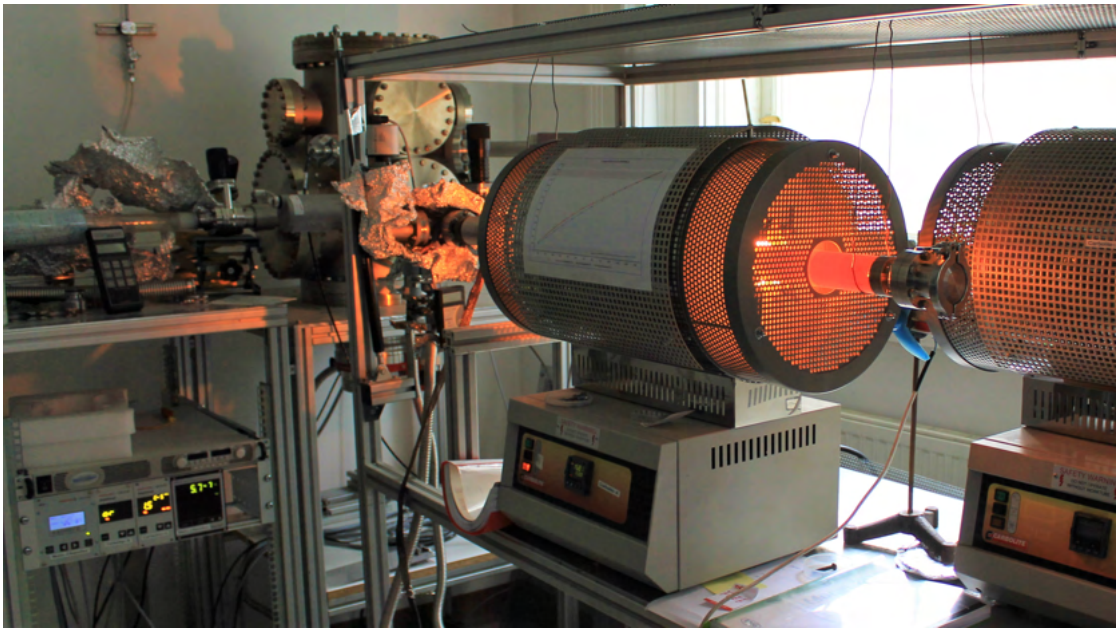

Figure 6.7: UHV and furnace setup for sample annealing under vacuum.

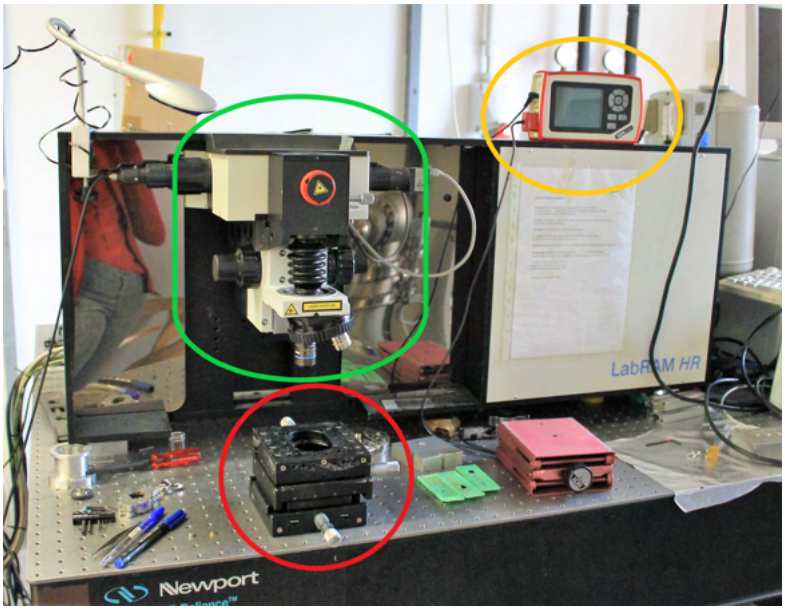

Figure 6.8: Horiba Jobin Yvon LabRAM HR multi-frequency Raman microscopy system. Green: microscope; yellow: light meter; red: micrometer xy stage.

spectroscopic measurements of molecules and solids with high spectral and lateral resolution. For the purposes of this work, I used the system coupled with a diode pumped laser source emitting at 785 nm. Measurements were taken with a 100× objective. Photos of the samples were taken with a 10× objective.

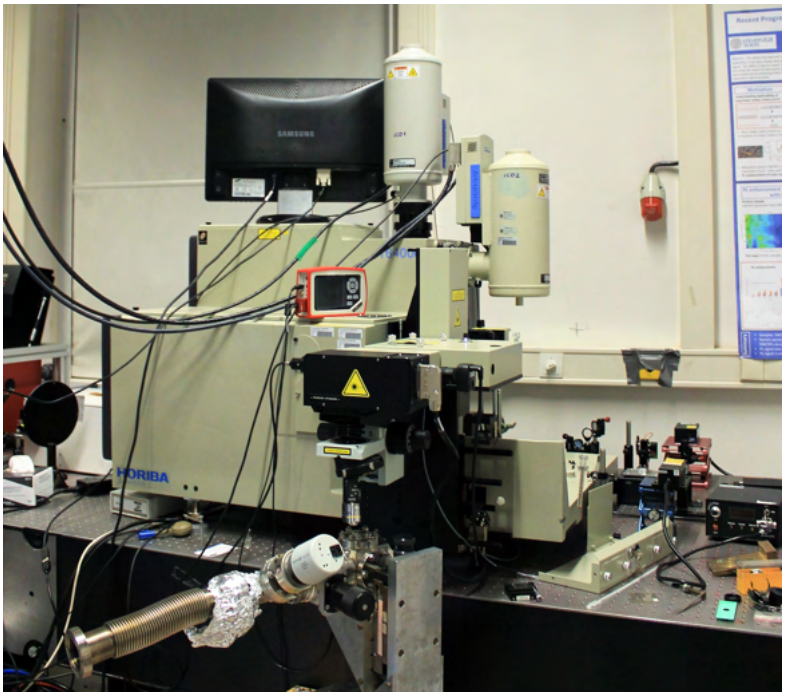

Figure 6.9: Horiba T64000 triple monocromator Raman microscopy system.

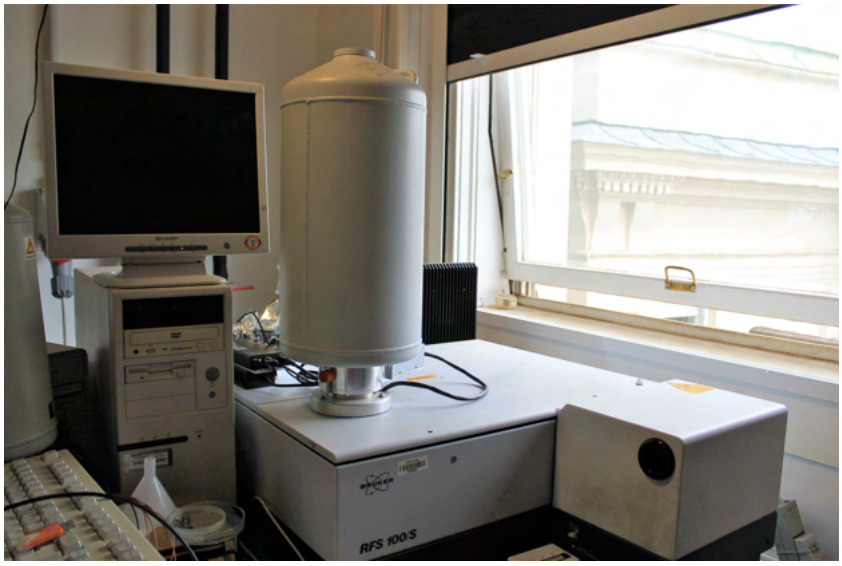

Figure 6.10: Brucker Fourier Transform Infrared Raman (FT-IR) Spectrometer RFS 100.

6.3.1 Multifrequency Resonance Raman Spectroscopy

The wide variety of spectrometers at my disposal allowed me to use multifrequency resonance Raman spectroscopy, so as to better investigate the resonance behaviours of the materials under examination. Though the available frequencies did not allow for a detailed Raman map, they were enough to discern different materials from one another.

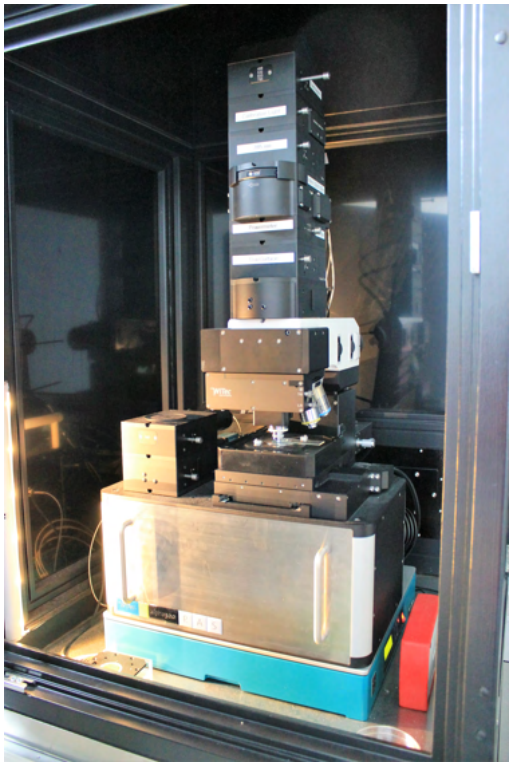

Figure 6.11: WiTech Alpha 300A high-resolution combined atomic force microscope/Raman system, available at the Faculty Center for Nanostructure Research of the University of Vienna.

Such an identification is reported in chapter 8, where the modes originating from terrylene, SWCNT with mean diameter of 1.4 nm and 5-AGNR@SWCNT are thus separated. In fact, the optical band gap of terrylene is at 557 nm, that of SWCNT is between 630 nm and 700 nm depending on the exact tube diameter, and that of 5-AGNR@SWCNT is observed to be close to 785 nm. The approximate resonance behaviour of these materials is reported in figure 6.12.

6.3.2 Peak Fitting of Raman Features

Whenever peak analysis of the Raman spectral features were required, the modes were fitted with Voigt profiles using the data processing and curve fitting tool Fityk.[158]

The full width at half maximum (FWHM) of a Voigt profile is estimated to be

$$FWHM = 0.5346 w_L + \sqrt{0.2169 w_L^2 + w_G^2} \tag{6.1}$$

where w_L and w_G are, respectively, the FWHM of the convoluted Lorentzian and Gaussian distributions.[159]

The Gaussian width w_G depends on the laser emission linewidth and on the spectrometer resolution. Therefore, I determined the w_G of the experimental peaks by fitting a Gaussian profile on the laserline measured at $0\,cm^{-1}$, as in the example reported in figure 6.13a.[160]. On the other hand, the Lorentzian width w_L depends both on vibrational lifetime and on Raman resonance.[9] Therefore either the physical conditions

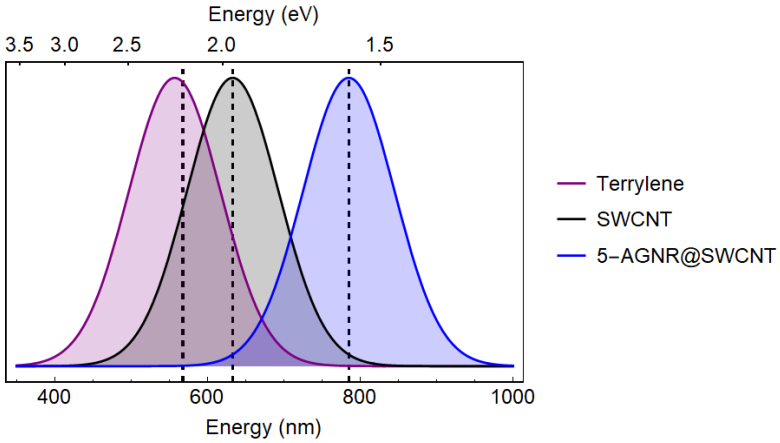

Figure 6.12: Approximate Raman resonance behaviour of terrylene, SWCNT with mean diameter of 1.4 nm and the hybrid system 5-AGNR@SWCNT. The dashed lines highlight were the 586, 633 and 785 nm laserlines are.

of the sample or the resonance with the exciting laser can be investigated if the other parameter is maintained unchanged. An example of peak identification via Voigt fitting is in figure 6.13b, where the CH modes of crystalline terrylene were fitted.

(a) (b)

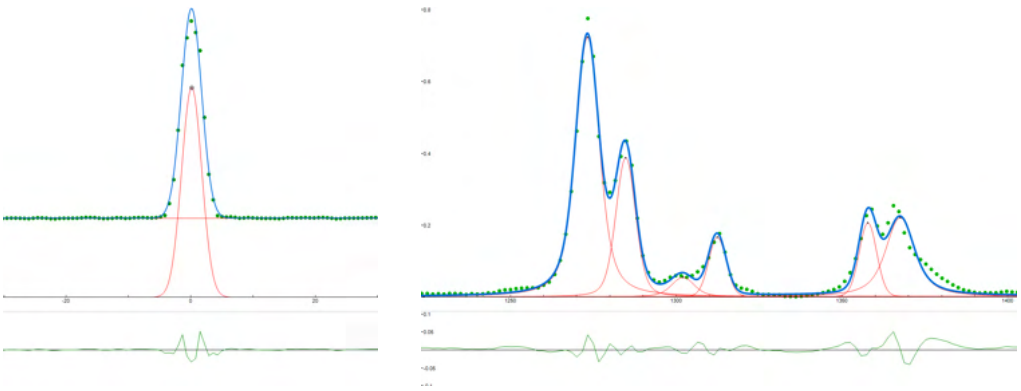

Figure 6.13: (a) Fitting of laserline of 633 nm laser with a gaussian distribution and a linear background. (b) Fitting of CH lines of terrylene with Voigt profiles. Residuals of fitting are represented in the lower graphs.

Chapter 7

Synthesis of Nanographenes by Cyclodehydrofluorination

*This chapter represents the results of my paper: "*In-situ *laser annealing as pathway for the metal free synthesis of tailored nanographenes".[160]*

My contribution consisted in experiment preparation, data acquisition, data analysis, manuscript writing including text and figures.

The molecules tetrafluoro-diphenyl-quinquephenyl and its target nanographene were synthesized by Dr. Ann-Kristin Steiner and provided by Prof. Konstantin Amsharov. Simulations of Raman spectra for this chapter were provided by Prof. Manuel Melle-Franco.

7.1 Finding the Best Experimental Conditions for Cyclodehydrofluorination

The fluorinated molecule tetrafluoro-diphenyl-quinquephenyl (TDQ), programmed for fourfold cyclodehydrofluorination into the nanographene (NG) heptacene dipyrene, was synthesized by Dr. Ann-Kristin Steiner at the Department of Organic Chemistry of the Friedrich Alexander University Erlangen-Nuremberg.

Both TDQ and the target NG were provided to me by Prof. Konstantin Amsharov.

After having acquired the TDQ precursor, I needed to determine the best way to transform it into NG. In order to do this, I found the approximate evaporation temperature under HV of TDQ and used multifrequency resonance Raman to determine which exciting wavelength would provide the best signal-to-noise ratio (SNR) ratio.

7.1.1 Evaporation Temperature of TDQ

As the CDHF reaction releases the highly dangerous gas HF, any investigation at any temperature higher than room temperature had to be conducted in a HV connected to the fume hood exhaust system in order to be carried out safely.

Using a HV setup with a home-made coil heater connected to a voltage generator, I subjected the powdered molecule to stepwise heating. Local temperature on the sample was measured with a custom-built thermocouple. Each increase in temperature was approximately 10 °C , after which the sample was left to stabilize for about one hour.

By observing at what temperature TDQ crystals formed in a condensation ring just outside the coil heater, I found that the evaporation temperature of the molecule was $(110 \pm 10)\,^{\circ}\mathrm{C}$ at a pressure of about 10^{-6} mbar.

7.1.2 Multifrequency Resonance Raman

Figure 7.1 shows the Raman fingerprint of the TDQ molecule recorded at room temperature with laser wavelengths of 458nm, 488nm, 514nm, 568nm, 1064nm.

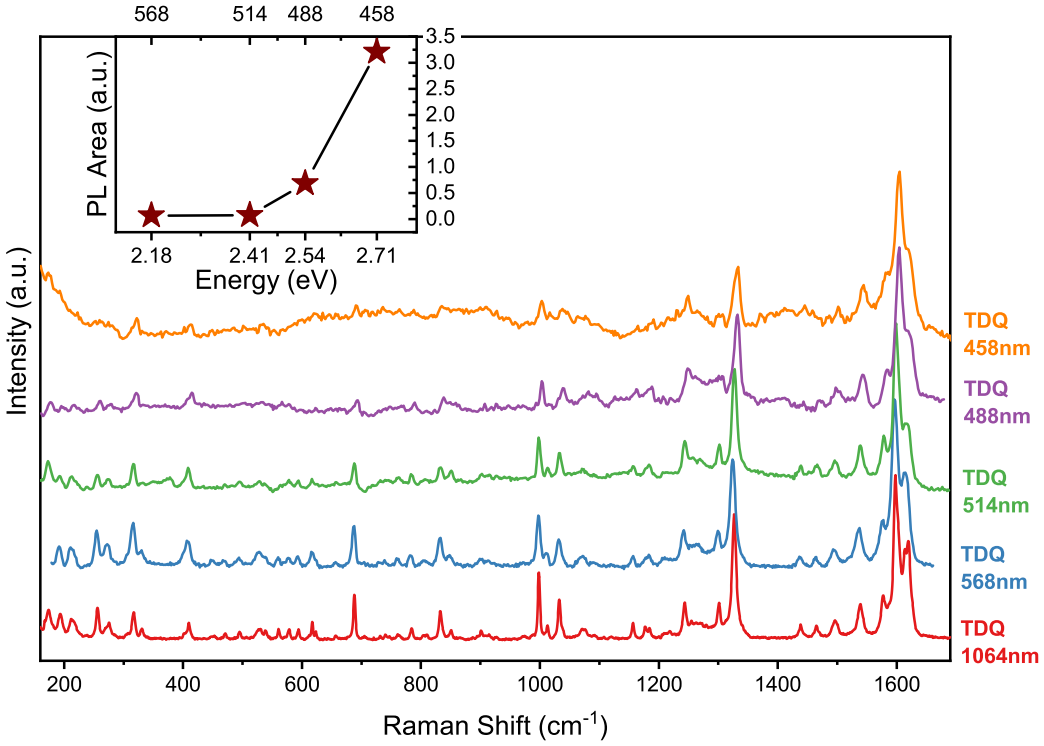

Figure 7.1: Raman fingerprint of TDQ deposited on aluminum oxide at exciting laser wavelengths of 458nm, 488nm, 514nm, 568nm and 1064nm. Inset: experimental photoluminescence background vs. exciting laser energy.

In order to analyze the relative response of the intrinsic Raman signal, I subtracted complementary fluorescence backgrounds, taking into account the shape of the photoluminescence (PL) background. Intensities were normalized to the G-peak at $\sim$1600 cm^{-1}.

The inset in figure 7.1 shows the dependence of PL on exciting laser energies in the visible range, quantified as the background area under the TDQ spectra.

It is possible to observe an increase in photoluminescence and a decrease in the relative intensity of the sample's characteristic emission for shorter wavelengths, which leads to higher noise levels after background subtraction and normalization. This happens because the optical gap of TDQ is in the ultraviolet range: increasing the incident photon energy, therefore, tunes the laser to the emission spectrum of the molecule, which is a complementary process to the vibronic excitation of the sample.[110]

The best SNR is achieved with the exciting wavelength of 1064nm, as its energy is too low to excite PL. However, acquisition at this wavelength is too slow to allow *in-situ* investigation of chemical processes.

The wavelength chosen for investigation into TDQ is thus 568nm, whose spectrum has the lowest PL among visible wavelengths.

As an additional reference, I acquired the target NG spectrum with exciting laser wavelength 1064nm. Because of excess PL, it was not possible to record this molecule's spectrum for visible wavelengths.

Additionally, the Raman spectra for the most likely conformations in the TDQ molecule and in the target NG were computed with DFT by prof. Manuel Melle-Franco. A graphic comparison between experimental acquired at 1064nm for TDQ and NG and their computed spectra is in figure 7.2a.

The presented simulated spectrum corresponds to the most populated conformation as all computed conformers yielded fundamentally similar spectra. The identification and analysis of the Raman active modes with sizable contributions by F atoms were obtained by prof. Melle-Franco computing and ranking the ratio of the F displacements with respect to the total.[161]

As further comparison between theory and experiment, I executed a peak analysis on the G-line and on the strongest fluorine related Raman active modes of TDQ, both the computed and the experimental 568nm spectra, results for which are in tables 7.1 and 7.2, respectively.

All experimental components of the G-band have a correspondence in predictions by TDQ calculations, except for the feature at 1591, which is not visible in the experimental spectrum (table 7.1). This is likely due to the lower intensity of the mode with respect to its spectral neighbors.

In the case of fluorine related Raman active modes (table 7.2), theoretical predictions fit remarkably well the experimental spectrum, allowing the correct identification of spectral features corresponding to CF vibrations.

Center (cm^{-1})		Intensity × 100 (a.u.)		FWHM (cm^{-1})	
T	E	T	E	T	E
1436	1437	21,4	6,6	8,5	13,8
1470	1464	9,1	5,9	8,0	3,3
1490	1495	7,9	10,7	8,0	14,3
1500	1519	34,5	2,3	8,0	16,4
1533	1536	39,7	22,0	8,0	14,1
1581	1576	52,6	20,5	8,2	13,8
1591	=	26,4	=	9,7	=
1607	1597	83,0	93,4	8,3	12,3
1614	1612	64,3	33,5	7,0	1,8
1622	1618	51,4	28,2	8,8	10,6

Table 7.1: Peak deconvolution of the G-line of TDQ, comparison between the theoretical computed spectrum (T) and experimental spectrum measured at 568nm (E). The peak predicted to be at 1590 was not identifiable in the experimental spectrum.

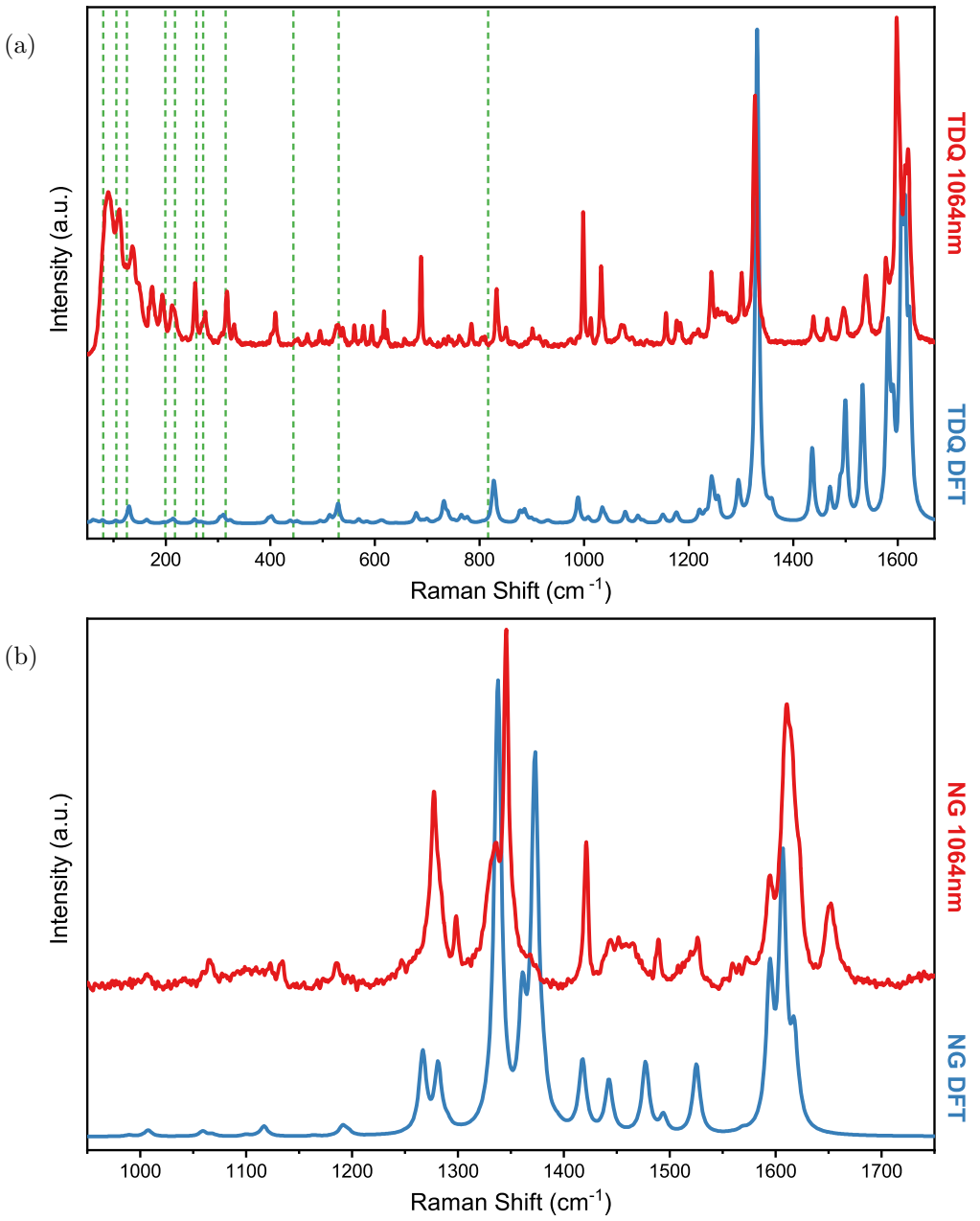

Figure 7.2: Raman fingerprint of (a) TDQ and (b) target NG at exciting laser wavelength of 1064nm, compared to DFT simulations at the PBE-6-31G(d,p)-D3 level. In figure (a) computed vibrations of TDQ with large F displacement are reported in green dashed lines.

Center (cm^{-1})		Intensity × 100 (a.u.)		FWHM (cm^{-1})	
T	E	T	E	T	E
255	255	1,2	20,1	8,2	8,6
268	272	0,4	12,7	7,7	11,8
304	306	1,4	03,2	7,9	7,6
311	316	2,2	24,1	8,0	8,9
324	330	0,8	06,8	7,9	10,1

Table 7.2: Peak deconvolution of the strongest Raman active modes with large F displacement in the TDQ spectrum, comparison between the theoretical computed spectrum (T) and experimental spectrum measured at 568nm (E).

7.2 Laser Annealing on TDQ

The precursor was annealed through laser irradiation in HV using the Raman spectroscopic HV set-up with a 568nm laser at $(1.6 \times 10^4)\mathrm{W\,cm^{-2}}$ irradiation. This laser line, being in the vanishing tail of the fluorescence spectrum of the target precursor molecule, enables us to have a weak luminescence Raman spectrum, which concomitantly allows to study the transformation to nanographene from both a decrease of the luminescence and a change in the Raman fingerprint.[110]

A selection of original spectra gathered during laser annealing are in figure 7.3a. The acquisition time for each laser annealing cycle was 100s, while the time between the end of an acquisition and the start of the next was about 20s.

During the laser annealing process, the molecule's color turned from white to black. An indication of TDQ decomposition came from the quartz optical window of the HV chamber, whose inner surface was etched by hydrogen fluoride during the experiment. No other fluorinated materials were present inside the HV chamber, therefore hydrogen fluoride must have originated from the first step of cyclodehydrofluorination, in which the molecule decomposes by breaking its CF bonds.

A dramatic increase in fluorescence between the first and second cycles was observed, followed by a slow decrease that continued through the whole process. At the same time, the Raman fingerprint of the molecule progressively lost intensity, leading to a decreasing signal-to-noise ratio.

In order to highlight the molecular fingerprint, a background subtraction was needed. It is now important to note that the spectral background is made of two separate components.

The most prominent one is the photoluminescence of TDQ, which is approximately linear in shape, but, as has already been observed, evolves with increasing irradiation time.

An additional component, which is constant for all acquired spectra, is the stray Raman fingerprint of the fused quartz UHV window. Though the laser was focused on the TDQ precursor below the window, stray Raman signals from out-of-focus materials have already been reported.[164] Moreover, this background component was isolated from the spectrum with the lowest SNR, namely cycle 32, as reported in figure 7.3 and its shape is consistent with the fingerprint of fused quartz glass reported in literature.[162, 163]

After executing a subtraction of the stray quartz signal, the changes in photolumi-

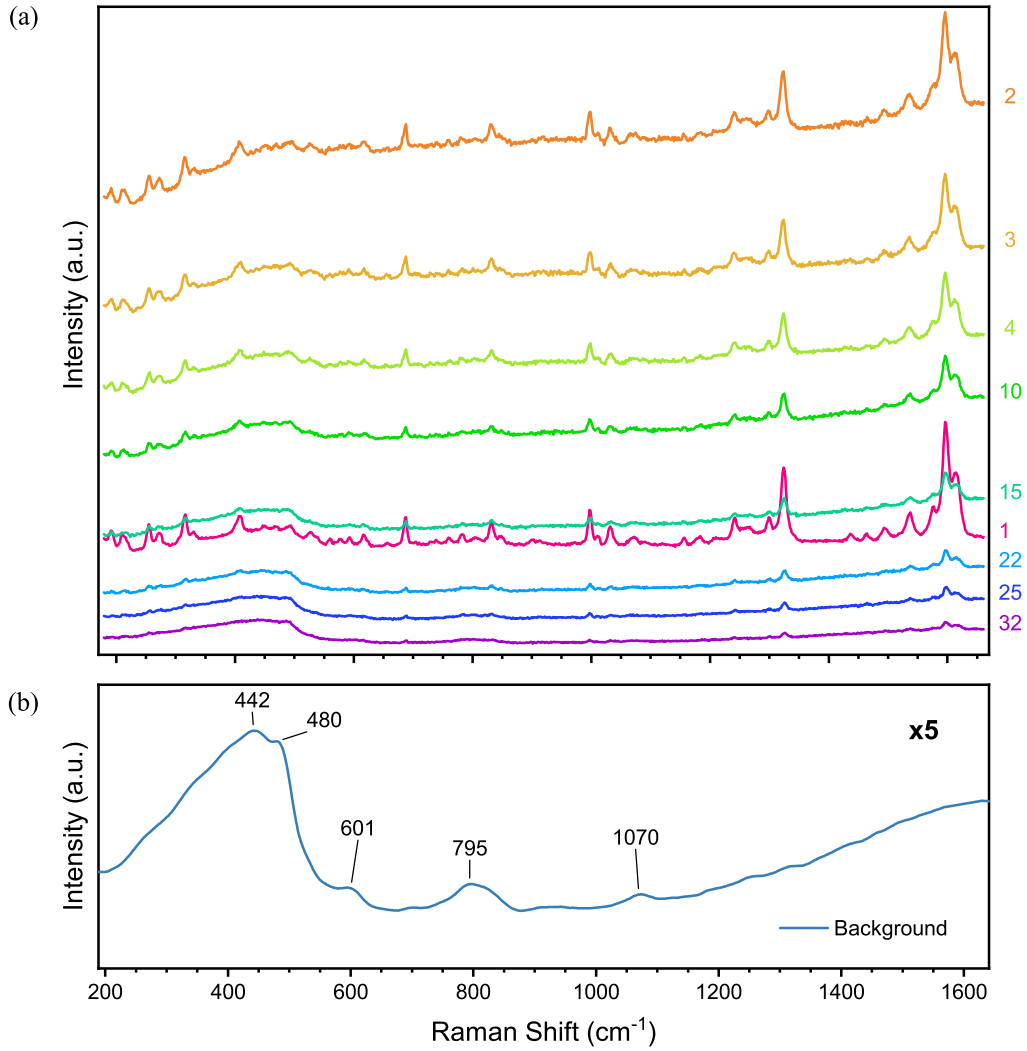

Figure 7.3: (a) Selection of unprocessed spectra acquired during *in situ* laser annealing. The photoluminescence background increases dramatically between the first and the second acquisition cycle, then it decreases slowly throughout the whole process (b) Constant component of the background extrapolated from the acquisition cycle with lowest SNR, cycle 32. The shape and the highlighted peaks are compatible to a fused quartz glass fingerprint,[162, 163] thus it originates from the stray Raman signal from the UHV window.

nescence were quantified by integration of the remaining background area. Acquisition cycles were equally spaced in time, with each cycle starting 120s after the previous one:

$$\text{Time [s]} = 120\,\text{s} \cdot \text{Cycle} \tag{7.1}$$

Using this equality, I was able to plot the photoluminescence evolution against time, as is represented in figure 7.4a. The changing photoluminescence indicates that a transformation of the TDQ precursor took place.

After further subtraction of the photoluminescence background found in the previous

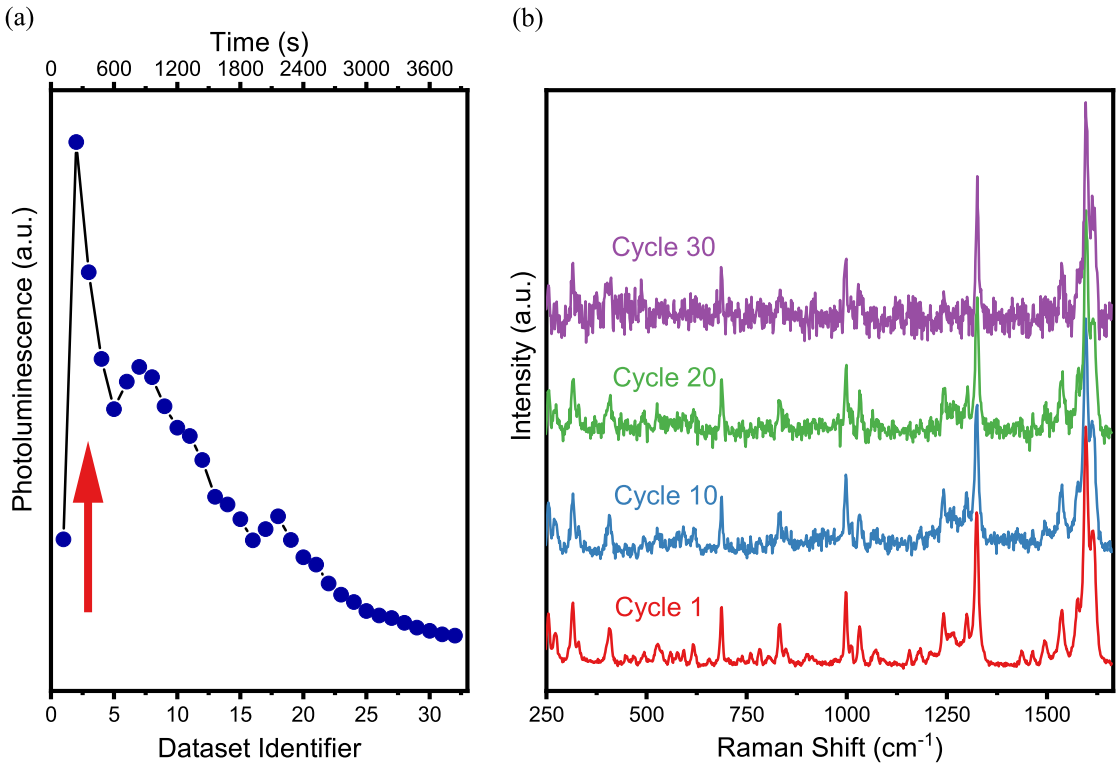

Figure 7.4: (a) Evolution of the area of the photoluminescence background during laser annealing: after a sharp increase between cycle 1 and 2, it decreases gradually. The changing photoluminescence indicates that a transformation of the TDQ precursor took place. (b) Spectral evolution under laser annealing at 568nm. The spectrum loses definition as the intensity decreases (background was subtracted, spectra were normalized to the G-line).

ste, all spectra were normalized to the G-band at $\sim$1600 cm^{-1} in order to highlight the spectral evolution of the Raman fingerprint, a selection of which is reported in figure 7.4b. The main spectral features persist during the whole laser annealing process, even as the signal loses definition leading to a diminishing SNR.

In summary, the processes I described are the changes in photoluminescence and molecular color, the etching of the quartz UHV window, the diminishing SNR.If considered together, they all point to transition of TDQ into another molecular species.

In order to gain better understanding into the physical and chemical processes that had happened during laser annealing, the next step I took was to determine the local temperature a posteriori, which can be done by correlating the lineshape width Γ to the sample temperature.

7.3 Extrapolation of Temperature from Raman Spectra

7.3.1 Correlation between Linewidth and Temperature

In order to determine the local temperature of the precursor during laser annealing, I used a T64000 spectrometer with exciting laser wavelength of 532 nm to record Stokes and anti-Stokes peaks at increasing laser irradiation.

I chose to examine Stokes and anti-Stokes scattering of the mode at 1326 cm^{-1}, as it is the second highest intensity feature in the TDQ spectrum. This mode is preferable to the higher intensity G-line because modes at the intensity of anti-Stokes lines decreases dramatically for modes with higher wavenumber.[139]

At equilibrium, equation 5.7 is a valid approximation of the ratio between Stokes and anti-Stokes intensities, I_S and I_A. In my calculations, though the detectors I used were CCDs, I used both values of A to provide a comparison between the two forms of the equation.

I executed a lineshape analysis on the recorded peaks which allowed me to find each peak's linewidth. I then correlated the linewidths thus found to sample temperature using equation 7.3. Results are reported in table 7.3 for each value of used laser irradiance.

I then plotted $\Gamma(\nu_m, T)$ as a function of temperature for all data reported in table 7.3. From these values, I was able to find an estimate for $\Gamma(\nu_m, 0)$ for $A = 3, 4$ by executing a non-linear fit of equation 5.9, as pictured in figure 7.5.

7.3.2 Extrapolation of Temperatures during Laser Annealing

The temperatures during laser annealing were then found by simply inverting equation 5.9:

$$T = \frac{h\nu_m}{2K_B}\left(\log\left(\frac{\Gamma(\nu_m, T) + \Gamma(\nu_m, 0)}{\Gamma(\nu_m, T) - \Gamma(\nu_m, 0)}\right)\right)^{-1} \tag{7.2}$$

and using the Lorentzian width found from fitting a Voigt profile on the peak at 1326 cm^{-1} with the program Fityk.[158]

The greatest contribution to the standard deviation on the temperature comes from the error of the estimate $\Gamma(\nu_m, 0)$, in comparison to which all other contributions are negligible. The standard deviation on the temperature calculated by 7.2 is thus:

Irradiance ($W \cdot cm^{-2}$)	I_A (a.u.)	I_S (a.u.)	T (K), $A = 3$	T (K), $A = 4$
$1.4 \cdot 10^2$	13.3	2336.5	341.5	333.0
$3.4 \cdot 10^2$	85.7	4016.2	446.4	432.1
$6.0 \cdot 10^2$	17.5	1032.8	424.0	411.1
$1.0 \cdot 10^3$	42.0	1028.9	526.3	506.5

Table 7.3: Experimental data of Stokes and anti-Stokes processes measured with T64000 spectrometer at 532 nm laser wavelength and temperatures calculated from equation 5.8 with $A = 3, 4$.

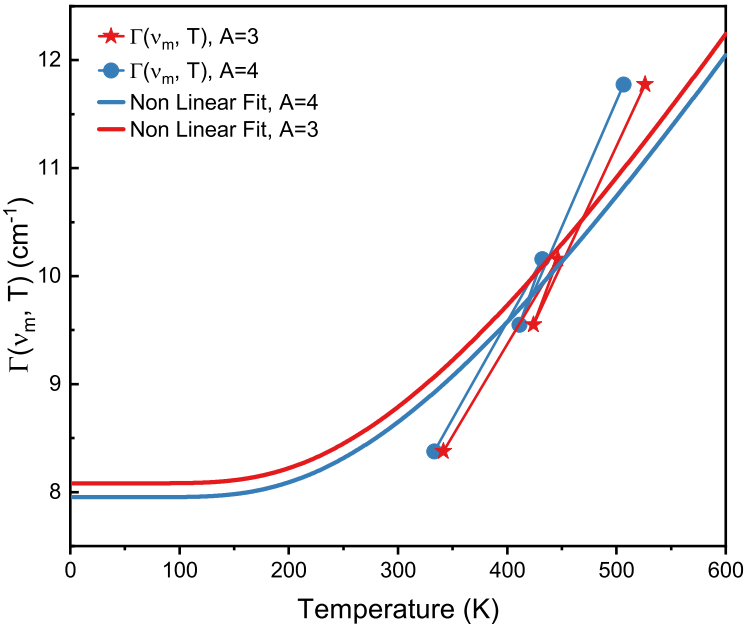

Figure 7.5: Non-linear fit on (T, $\Gamma(\nu_m, \mathrm{T})$).

$$\begin{aligned}\sigma_T &= \sqrt{\frac{\partial T}{\partial \Gamma(\nu_m,0)}^2 \sigma^2_{\Gamma(\nu_m,0)}} = \\ &= \frac{h\nu_m}{K_B}\left(\log^2\left(\frac{\Gamma(\nu_m,T)+\Gamma(\nu_m,0)}{\Gamma(\nu_m,T)-\Gamma(\nu_m,0)}\right)\right)^{-1} \frac{\Gamma(\nu_m,T)}{\Gamma(\nu_m,T)^2-\Gamma(\nu_m,0)^2}\,\sigma_{\Gamma(\nu_m,0)}\end{aligned} \tag{7.3}$$

The term $\sigma_{\Gamma(\nu_m,0)}$ is the standard deviation of $\Gamma(\nu_m,0)$, which is found from the non-linear fit in figure 7.5.

Results of Temperature Calculations

The results to my temperature extrapolation are reported graphically in figure 7.6 and numerically in appendix A.2.

The temperatures predicted by the two values of A follow the same trend. Temperatures calculated with $A = 3$ are in the order of 50 K higher than those calculated with $A = 4$. The biggest discrepancies are present in calculations on lower SNR spectra. The error σ_T, though, is always bigger for values calculated with $A = 4$. For this reason, from now on only temperatures calculated with $A = 3$ will be considered.

At the beginning of the laser annealing process, the precursor molecule heats almost immediately to about 1100K (green shading). The temperature is then about constant until cycle 4, when it starts decreasing (orange shading). After cycle 23 (grey shading) calculated values are unreliable due to the too low SNR. The trend change indicates that two different regimes were present before and after cycle 4.

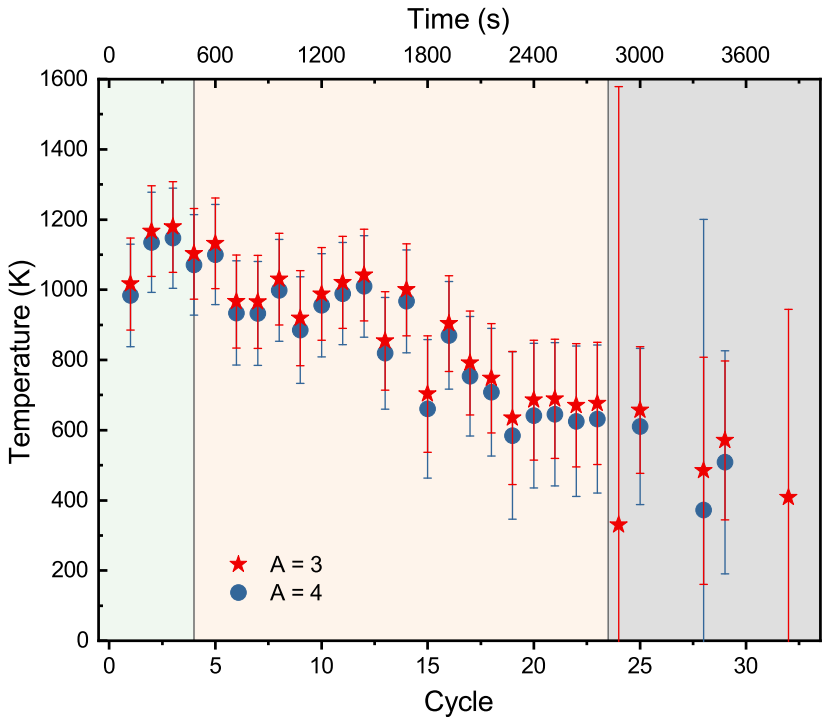

Figure 7.6: Temperature evolution during laser annealing calculated with equation 5.9. The standard deviation was calculated with equation 7.3. The temperature increases sharply from room temperature to about 1100K at the beginning of the process (green shading) and then gradually decreases (orange shading). The values after cycle 23 (grey shading) are unreliable due to lower signal-to-noise ratios.

7.4 Phase Transition during Laser Annealing

The temperature trend found in the previous paragraph suggests that at about cycle 4 of laser annealing a phase transition between two different regimes took place in the sample.

During the laser annealing process, the signal-to-noise ratio of the molecular Raman fingerprint decreased, while the color change of the molecule and etching on the inside of the optical window suggest a defluorination and graphitization of TDQ.

The Raman fingerprint of the target NG presents peaks between 1200 cm^{-1} and 1600 cm^{-1}, with a very low SNR because of strong photoluminescence when measured with visible light excitations. Therefore, the high photoluminescence is an indication that the target nanographene or similar molecules were synthesized by cyclodehydrofluorination of TDQ.

At the same time, the absence of signal from the decomposition products points to a non-uniform synthesis and to their fast transition into amorphous carbon due to the high irradiance used during laser annealing.[19]

A quantitative study of the spectrum's decay can be made after subtraction of the background. As suggested by the temperature trend above, the intensity decay can be separated at cycle 4 (480s) into two well defined regimes of exponential decrease (fig.

7.7). Each regime can be modeled by an exponentially decaying trend:

$$I = e^{-\lambda t} \tag{7.4}$$

In this case, the decay constant λ is a function of laser irradiation. In the second regime, between cycles 4 and 23, also the photoluminescence and the temperature decay exponentially (see figure 7.8).

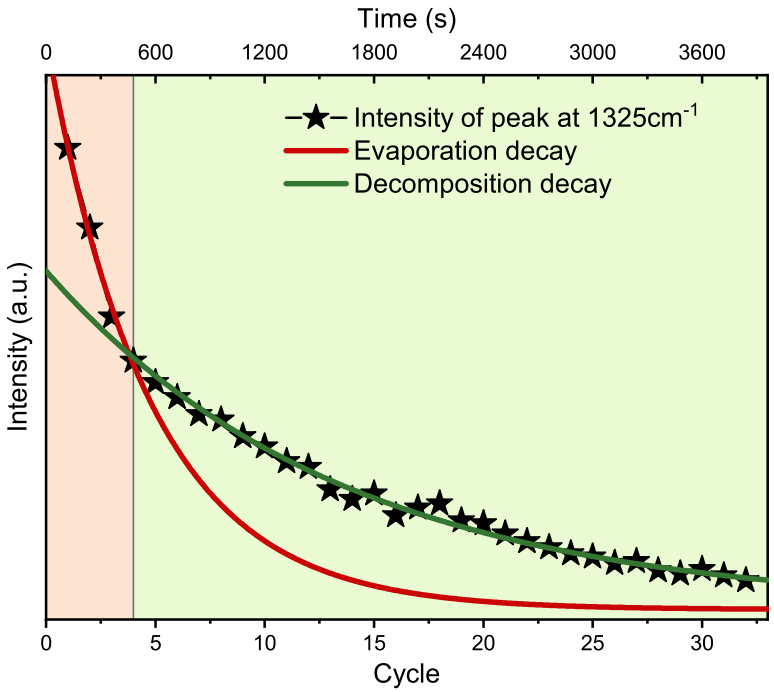

Figure 7.7: Intensity decay of the peak at 1326 cm^{-1}. Two distinct regimes can be identified: during the first, the decay is governed by evaporation, during the second by molecular decomposition into graphitized amorphous carbon.

Regime	λ (cycle^{-1})	σ_λ (cycle^{-1})	λ (s^{-1})	σ_λ (s^{-1})
Evaporation	796.85	0.04	$6.64{\cdot}10^{-2}$	$3.01{\cdot}10^{-4}$
Decomposition	744.47	0.03	$6.20{\cdot}10^{-2}$	$2.46{\cdot}^{-4}$

Table 7.4: Decay constants from fit.

In the first regime, the intensity decay is governed by the evaporation of the molecule λ_{ev}. In this regime, the calculated temperature is stable around 1100K within experimental error. At cycle 4 (480s), a phase change occurs, after which the intensity decay is governed by the decomposition of the precursor molecule until the end of the laser annealing. The later regime, therefore, is governed by the decomposition rate of the precursor molecule, λ_{dec}.

From the analysis of the two regimes, we can conclude that a transformation occurred in the molecule. As the temperature is stable in the first regime, already before cycle 2 a steady state is reached between heating by laser irradiation and heat dissipation.

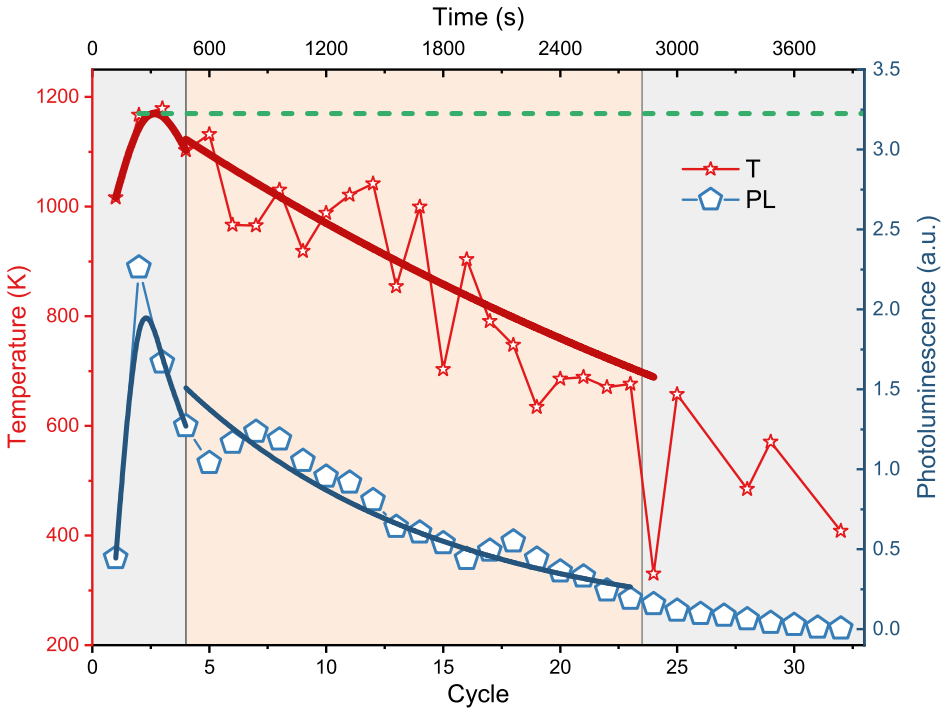

Figure 7.8: Fit of temperatures and photoluminescence (PL) in the decomposition regime (cycles 4 to 23). Dashed line: hypothetical constant temperature if no phase change between evaporation and decomposition regimes had occurred.

The high temperature reached fuels endothermal processes like evaporation and cyclodehydrofluorination, with a fraction of precursor molecules starting to decompose by breaking of CF and CH bonds, as sketched in figure 7.9a. This in turn leads to the formation of HF and CC bonds, which leads to small local clusters of graphitized material.

A phase change between unpercolated and percolated clusters of graphitized material occurs at cycle 4, as sketched in figure 7.9b. As observable in figure 7.8, in this regime both the temperature and the PL decrease exponentially, which means that heat conductivity increases dramatically as the light emission from the sample becomes quenched. If percolation did not occur, the temperature would be constant as the system would remain in the steady state reached during the evaporation regime.

The decrease in temperature is further evidence supporting the transformation of the precursor, as percolated graphitized materials lead to a more efficient heat exchange in comparison to single molecules held together by van der Waals interactions.

(a) (b)

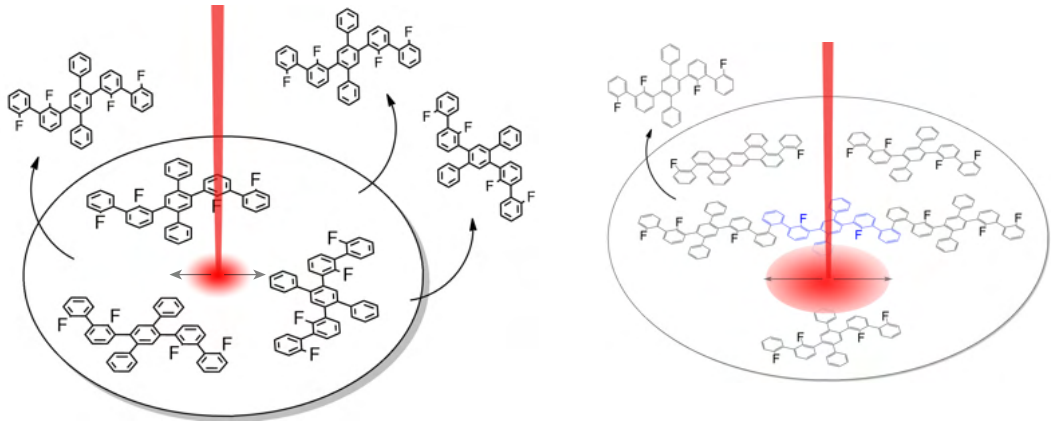

Figure 7.9: (a) Evaporation regime: heat conductivity in the precursor sample is small, temperature is constant, Raman signal decrease is mostly due to evaporation. (b) Decomposition regime: heat conductivity is high, temperature decreases, Raman signal decrease is dominated by molecular decomposition. The decomposed precursor molecules bond, creating graphitized material, which increases heat dissipation.

Chapter 8

5-AGNR encapsulated in SWCNT

This chapter represents the results of a manuscript currently under preparation, which was written together with my colleague Claudia Berkmann. Claudia Berkmann executed preliminary experiments that demonstrated the feasibility of the work, acquired and analyzed optical absorption data and prepared the draft for the manuscript. My contribution was to execute the main experiment, acquire Raman spectroscopy data and analyze it. The final version of the manuscript is the result of countless hours of discussion, interpretation and rewriting by both of us.

Simulations of Raman spectra for this chapter were provided by Prof. Manuel Melle-Franco and Jorge Laranjeira. AC-HRTEM pictures were taken by Prof. Kecheng Cao and contrast profiles were created by Prof. Lei Shi.

8.1 Optical Properties of Rylene Dyes

In order to study the optical properties of a small width GNR, I filled SWCNT with the rylene dye terrylene, which already has the structure of a very short 5-AGNR. A preliminary determinatino of the optical properties of rylene dyes was necessary to properly distinguish precursor from synthesis product.

8.1.1 Raman Fingerprint of Terrylene

The molecule I used for encapsulation into SWCNT and polymerization into GNR is terrylene, the second shortest molecule in the rylene dyes family.[165] Because of its relevance into this work, a detailed analysis of the molecule's Raman spectral features was necessary.

When it is in powder form, terrylene presents excessive fluorescence under Raman investigation, which is to be expected from a molecular dye. However, during the filling procedure, some van der Waals crystals of terrylene formed as condensation on the internal walls of the sealed glass vial used for filling. Crystalline alignment reduces dramatically the amount of fluorescence emitted by the molecule.

Nevertheless, fluorescence was still too high to obtain a detailed spectrum with a visible light excitation, therefore I used an exciting wavelength of 785 nm to record the Raman fingerprint of terrylene.

The Raman spectra for the most likely conformations in the free terrylene molecule were computed with DFT calculations by prof. Manuel Melle-Franco and Jorge Laranjeira.

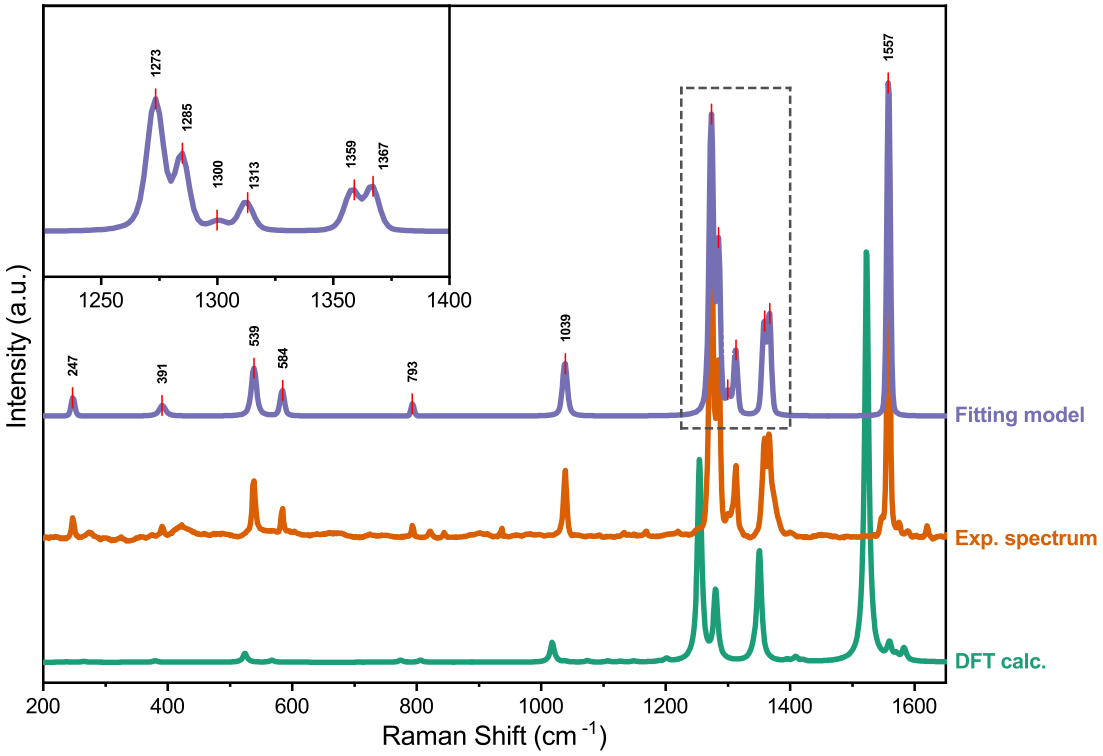

Figure 8.1: Raman fingerprint of terrylene acquired at exciting wavelength of 785nm, the DFT computed spectrum of free terrylene and the fitted model of experimental data, with peak identification. Inset: peak identification in the CH-modes region highlighted in the main graph by the dotted box.

Position (cm^{-1})	Identification	References
247	longitudinal compressive mode (LCM)	calculated from [151]
390	shear-like mode (SLM)	[19, 18]
538	radial breathing-like mode - (RBLM-)	[151]
584	radial breathing-like mode + (RBLM+)	[151]
792 - 1299	CH-modes	[71]
1359 - 1367	D-like mode (DLM)	[150]
1555	G-band	[148]

Table 8.1: Identification of terrylene Raman features found from peak analysis in figure 8.1.

Figure 8.1 reports both experimental data and the DFT calculations of free terrylene executed by Prof. Melle-Franco. The calculated spectrum of terrylene agrees remarkably well with the experimental one. The main difference between the two is the splitting into doublets of experimental DLM and CH-modes, due to a different dielectric environment.

Additionally, I fitted the most prominent spectral features with Voigt profiles as described in section 6.3.2, in order to find exact center and linewidth of each component.

Experimental peaks found by peak analysis are reported and their origin identified in table 8.1. Like all sp^2 hybridized structures, terrylene has a G-band vibration, which is found at $1557\,cm^{-1}$ [148]. As terrylene has the molecular structure of very short 5-AGNRs, it also shares most of their Raman features, such as CH-modes[71] and the shear-like mode (SLM)[19, 18].

The influence of confinement effects must also be taken into account. In fact, if we consider terrylene a 3-naphtalene unit 5-AGNR, the peak at 247 is clearly its longitudinal compressive mode (LCM), as can be extrapolated from the observed values reported in *Overbeck et al.*. Moreover, due to the short length of terrylene, the radial breathing-like mode (RBLM) of 5-AGNRs usually found around $540\,cm^{-1}$ loses its purely transversal character and splits into a doublet with lower (RBLM-) and higher energy (RBLM+) modes.[151]

This peak identification will be helpful later, in unraveling the terrylene signal from that of GNR encapsulated in SWCNT.

8.1.2 Length Related Effects in Rylene Dyes

In order to understand the influence of length on CH–vibrations and properly distinguish between the Raman modes of unpolymerized terrylene longer encapsulated 5-AGNR@SWCNT, a preliminary study was performed the rylene dyes perylene, terrylene and quaterrylene (molecular structures in figure 6.3).

The comparison between Raman fingerprints of perylene, terrylene and quaterrylene recorded at 568 nm is in figure 8.2. The CH–modes in the 1200-1400 cm^{-1} region of the spetra have a different intensity ratios and their position shifts to smaller wavenumbers with increasing length. The highest CH-modes of perylene, terrylene and quaterrylene are at $1355\,cm^{-1}$, $1272\,cm^{-1}$ and $1251\,cm^{-1}$ respectively.

We can hypothesize a dependence of the highest mode on the inverse length, in analogy to LCM, RBLM and SLM modes. In this case, the data can be fitted as shown in the inset in figure 6.3, to obtain the fitting function:

$$y = (1138 \pm 23) + (428 \pm 61) \cdot x \tag{8.1}$$

It follows that the highest CH mode of an infinitely long 5-AGNR is to be found around $1150\,cm^{-1}$, and that of 5-AGNR with intermediate lengths between 1150 and $1250\,cm^{-1}$.

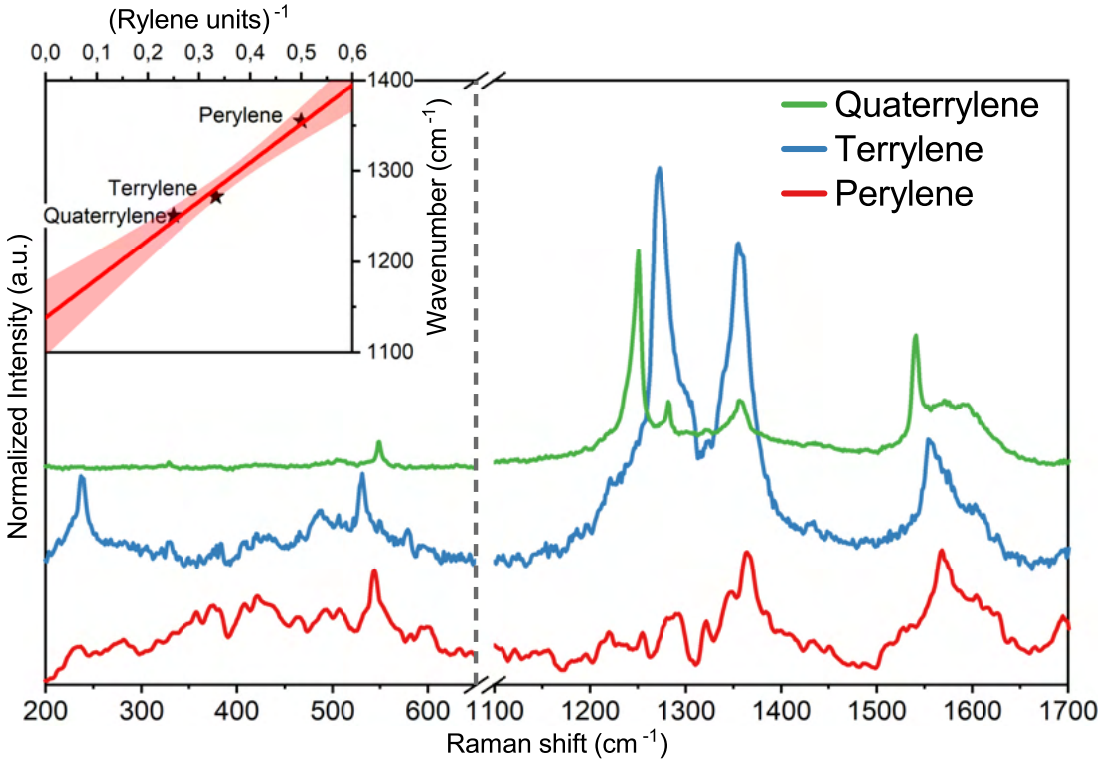

Figure 8.2: Comparison of Raman fingerprints of perylene, terrylene and quaterrylene recorded at 568nm, after background subtraction and normalization to the G-line. Inset: position of the highest CH-mode as function of inverse number of rylene groups in the molecule, overlapped with linear fit and one standard deviation confidence band.

8.2 Confirmation of filling

The first step I took after filling was to determine whether the encapsulation procedure had been successful.

Therefore, I washed the bucky paper sample thoroughly with DCM and acquired Raman spectra before and after the wash (see section 6.2). The background fluorescence disappeared, while the intensity of the sample's Raman response almost tripled, as reported in figure 6.6. On the one hand the absence of fluorescence demonstrates that excess terrylene was removed with washing, and on the other an increase of Raman signal is commonly seen in dyes after successful encapsulation in SWCNT because of increased sample order [126].

Further confirmation of successful encapsulation comes from the synthesis of inner tubes via heat treatment of the hybrid sample at 1550°C[115, 116, 123]. RBMs of syntesized DWCNTs with many inner tube diameters are visible in the Raman spectra in figure 8.3a. Their diameter is calculated in section B.1. Moreover the RBM of SWCNTs up–shifts and changes its shape significantly after encapsulation as reported figure 8.3b, due to a changed force constant.[166, 167]

However, as mentioned above the last mono–layer is harder to wash away,[114] and although the PL of the dye is quenched a lot in the Raman spectra, there are still some peaks present which can be attributed to terrylene monomers. Additionally, in this layer

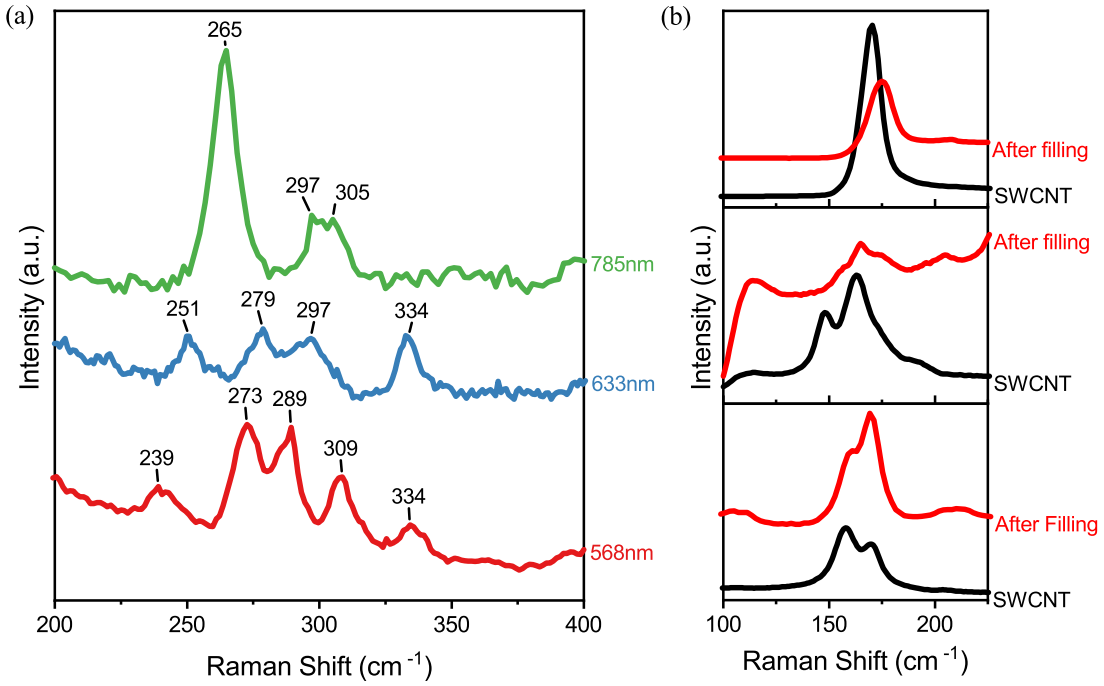

Figure 8.3: (a) RBMs of DWCNTs synthesized after heating at 1550 °C, recorded at 568nm, 633 nm and 785 nm. (b) Comparison between RBMs of encapsulating SWCNT before and after filling. The modes up–shift and change shape due to a changed force constant. Recorded at at 568 nm (top) 633 nm (middle) and 785 nm (bottom).

the PL quenching can also be explained by Förster resonance energy transfer (FRET) from the dye molecules to the tubes [168, 169, 170, 171, 172].

Successful filling was also confirmed by aberration-corrected high resolution transmission electron microscopy (AC-HRTEM) pictures taken by Prof. Kecheng Cao. Figure 8.4a clearly shows the presence of long flat molecules inside SWCNT already after filling at 350 °C and DCM washing. Structures on the outside of the tubes are also visible. Contrast analysis was executed by Prof. Lei Shi on the highlighted bars and results are reported in figure 8.4b. The flat molecules encapsulated in SWCNT have a width compatible with the computed value of 0.49 nm for 5-AGNR.

Multifrequency resonance Raman on encapsulated terrylene recorded at exciting wavelengths of 568, 633 and 785 nm is reported in figure 8.5, together with Raman spectra of unfilled SWCNTs and crystalline terrylene recorded at 785 nm. These wavelengths were used as 568 nm is close to the terrylene optical band gap at 557 nm, 633 nm is in resonance with SWCNTs and 785 nm is close to the 5-AGNR band gap.

In the CH-mode region, between 1200 cm^{-1} and 1400 cm^{-1}, multiple peaks originated by CH vibrations are present. Their relative intensities vary according to the exciting wavelength. This indicates the presence of different molecular species, as in resonance Raman their signal is enhanced in the vicinity of their energy gap.

The terrylene monomer peaks are dominant in the spectra after filling at the laser lines 568 nm and 633 nm, while their intensity is much lower at 785 nm. In addition to that, new lines appear in the RBLM and CH-modes regions in resonance with the 785 nm excitation, that are related to neither SWCNT nor terrylene and possibly belong to the

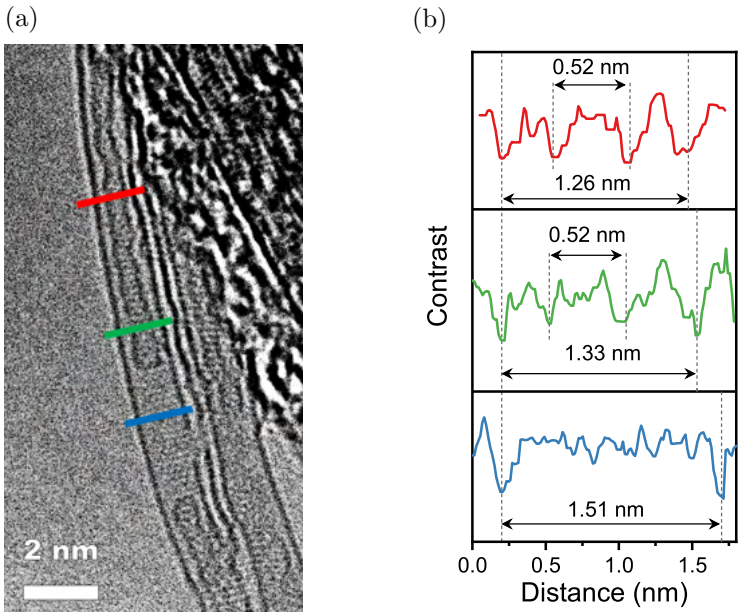

Figure 8.4: (a) AC-HRTEM image of terrylene@SWCNT after filling. Flat encapsulated structures are already present inside the tubes. (b) Contrast profile of the highlighted lines in (a).

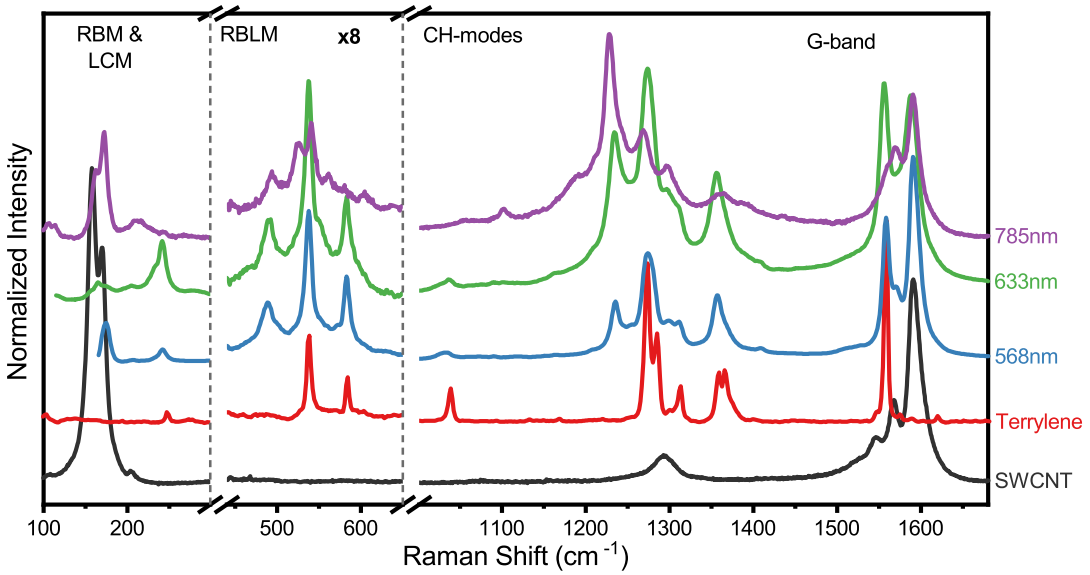

Figure 8.5: Raman spectra of pristine SWCNT, terrylene, both acquired at 785 nm, and terrylene @ SWCNT after filling at 350 °C and washing with DCM, acquired at 568 nm, 633 nm and 785 nm. The presence of modes not attributable to either terrylene nor SWCNT points to successful filling and polymerization.

encapsulated 5-AGNR@SWCNT. The most dominant of these is found at 1230 cm^{-1}.

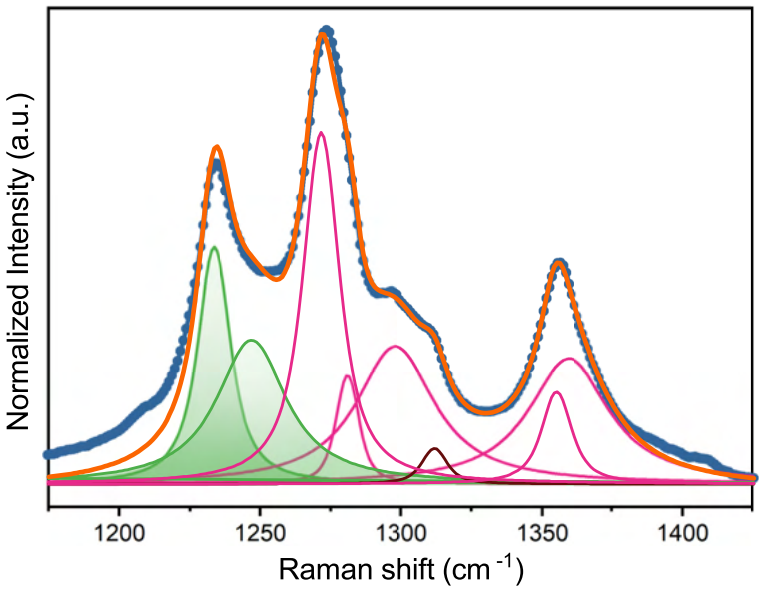

Figure 8.6: Peak fitting model (orange) of CH-modes of 633 nm spectrum after filling (blue dots). Most of the identified features originate from terrylene (magenta) or to SWCNT (black), while others, highlighted in green, are possible GNR vibrations.

Position (cm^{-1})		
Terrylene	SWCNT	5-AGNR
1271	1312	1233
1281		1247
1298		
1355		
1360		

Table 8.2: Centers of peaks identified by peak fitting in figure 8.6.

In order to start to quantitatively unravel features arising from different molecular species, I executed a peak deconvolution on the CH-mode region of the 633 nm spectrum by fitting Voigt profiles to the spectrum and is reported in figure 8.6. Centers of identified peaks are reported in table 8.2.

This wavelength was chosen to facilitate peak deconvolution, as features of different origin, such as terrylene-related modes and the one at 1230 cm^{-1}, have comparable intensities. On one hand, most of the peaks found this way are identifiable with known terrylene CH-vibrations or with the SWCNT D-band. On the other hand, the peak at 1230 cm^{-1} and a feature at 1247 cm^{-1} highlighted in the graph must originate from another molecular species, likely 5-AGNR@SWCNT.

Despite thorough washing, multiple features attributable to terrylene are present in the Raman spectra after filling and persist even after thorough washing with DCM. Thus, in order to unravel the properties of the CH–modes of the GNR alone, further analysis on the spectra is required.

These results show that the terrylene encapsulation and GNR growth was successful, but despite thorough washing, multiple features attributable to terrylene are present in the Raman spectra after filling and persist even after thorough washing with DCM. Thus, in order to unravel the CH–modes of the GNR alone, further analysis on the spectra is required.

8.3 Annealing Series

Let us now turn to Raman spectral changes as a function of annealing temperature. This will be helpful in unravelling the signal of the hybrid system 5-AGNR@SWCNT from that of its precursor, as we expect mono–layer terrylene on the outside of SWCNTs to burn away at a temperature lower than the decomposition temperature of encapsulated GNR.

Filled SWCNT samples underwent heat treatment under vacuum better than 10^{-5} mbar for two hours, each at a different temperature between 400°C and 800°C with 50 °C steps.

Laser lines 568 nm, 633 nm and 785 nm where chosen for investigation with Raman spectroscopy. The first two resonantly enhance the optical band gap of terrylene at 557 nm and the latter is in resonance with the much lower band gap of longer 5–AGNR. The spectra were normalized to the G-band of SWCNTs.

The exponentially decaying background due to the laserline was fitted with a sum of linear background and exponential decay:

$$a + bx + c \cdot \exp(-(x/d)) \tag{8.2}$$

and subtracted from all spectra.

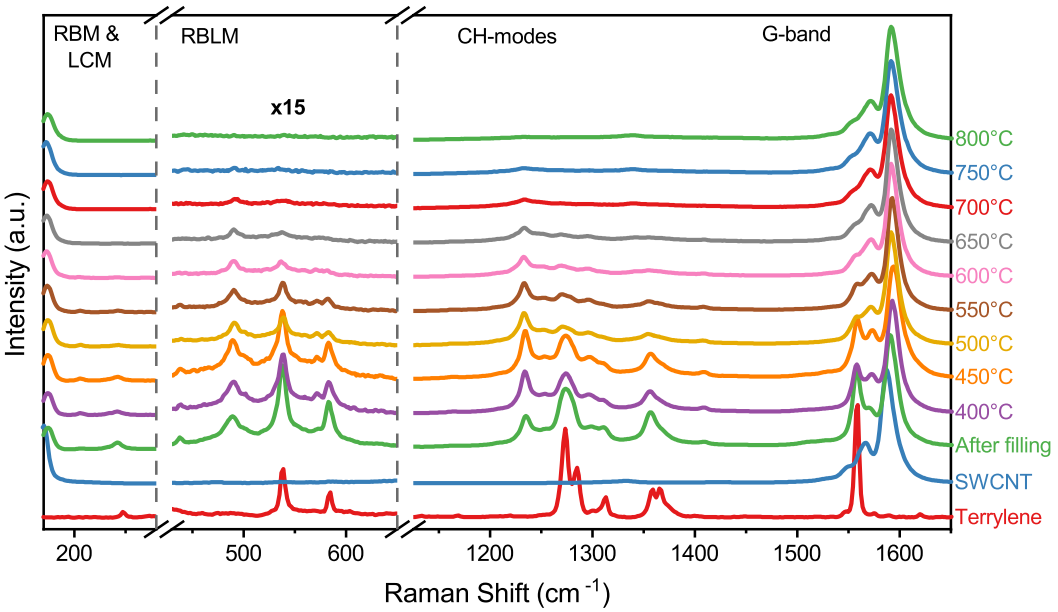

Figure 8.7: Evolution under heat treatment of the hybrid system 5-AGNR@SWCNT recorded at 568 nm exciting wavelength.

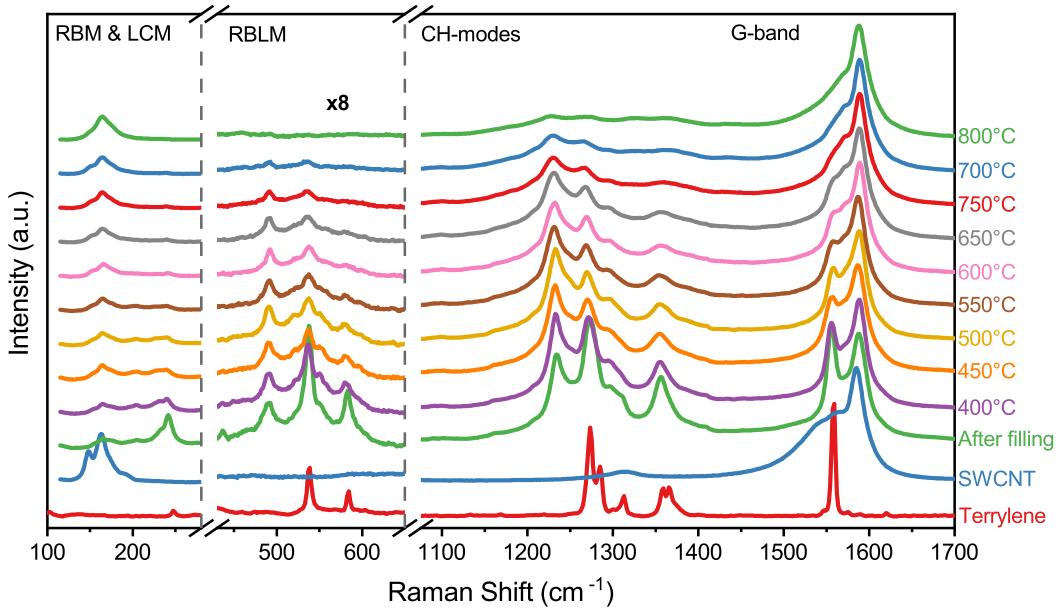

Figure 8.8: Evolution under heat treatment of the hybrid system 5-AGNR@SWCNT recorded at 633 nm exciting wavelength.

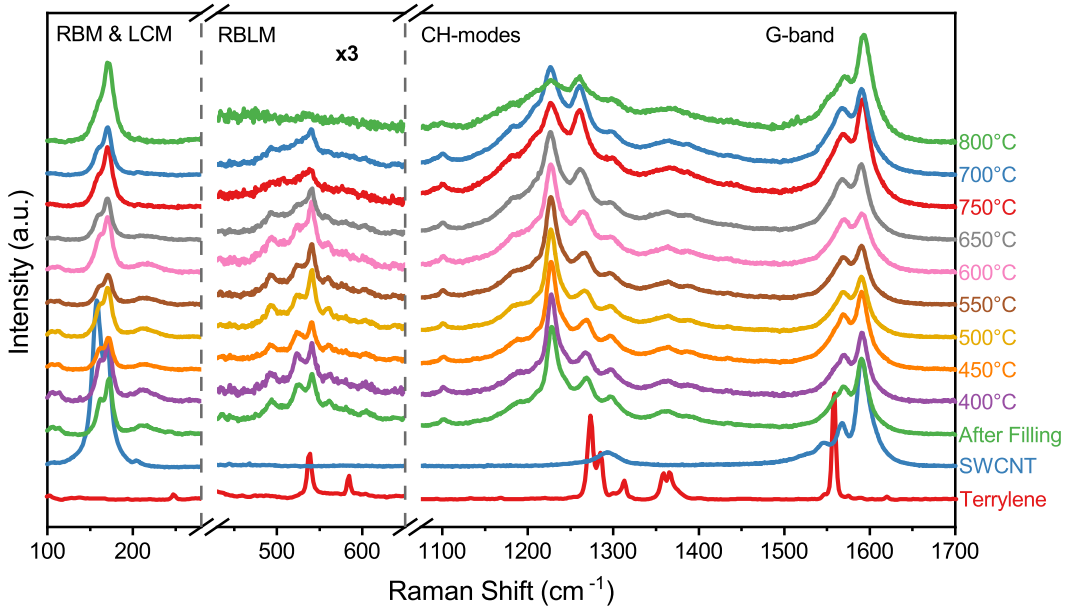

Figure 8.9: Evolution under heat treatment of the hybrid system 5-AGNR@SWCNT recorded at 785 nm exciting wavelength.

The data I gathered is reported in figures 8.7, 8.8 and 8.9 for exciting wavelengths 568 nm, 633 nm and 785 nm respectively. The spectra were normalized to the G-band of SWCNTs, which was prominent in all spectra.

It is interesting to observe how the spectral features evolve dependent on annealing temperature. In general, most of the signals in the 568 nm spectrum that don't belong to SWCNT decay rapidly, while in the 785 nm spectrum additional features are visible until heating at 800 °C. This behaviour suggests that, as expected, the encapsulated GNR and the unpolymerized terrylene left on the outside of the sample react differently to heat exposure.

One example of this is the RLBM, which is found at around 539 cm^{-1} for both 5-AGNR and terrylene. Modes from the two molecular species are therefore too close to be resolvable with the spectrometer used. However, we can use the photoselectivity of resonance Raman spectroscopy to observe that the RBLM in the 568 nm spectrum, whose biggest contribution comes from terrylene, undergoes a different evolution from the RBLM in the 785 nm spectrum, which mainly originates from 5-AGNR@SWCNT.

The feature with the most peculiar behaviour is that at about 1272 cm^{-1}. It is visible in all spectra after filling: it decays rapidly at 568 nm and is stable at 785 nm before gaining in intensity. It is prominent in the 633 nm spectrum, where its center downshifts to 1266 cm^{-1} before undergoing a slight upshift. This behavior strongly indicates that multiple components of different origin constitute the feature.

8.3.1 Terrylene Removal under Heat Treatment

I executed a lineshape analysis by fitting a Voigt profile on the G-band of terrylene at 1555 cm^{-1},[158] so as to quantitatively identify the influence of residual mono-layer terrylene on the Raman spectra of 5-AGNR@SWCNT. We find that its intensity decays exponentially with increasing temperatures, as evidenced by the fitted model in figure 8.10, which can be used as scaling factor for the terrylene signal.

The last mono-layer of the precursor molecule is notoriously difficult to remove from the tube outside, but the exponential decrease in terrylene signal demonstrates its removal with increasing annealing temperatures. This heating procedure cleans the hybrid material 5-AGNR@SWCNT, preparing it for further characterization devoid of influence of the precursor molecule.

The existence of multicomponent features such as the RBLM and the peak at 1272 cm^{-1} , indicates that a subtraction of the terrylene fingerprint should be executed to properly disentangle it from the signal of 5-AGNR@SWCNT.

A detailed Raman fingerprint of crystalline terrylene was only available for excitation at 785 nm, so I had to create an empirical model to take into account laserline broadening and different CCD sensibilities at other exciting wavelengths. I did this by fitting the terrylene spectrum and then adapting the fitted model to take into account the varying laserline widths and detection resolutions at different wavelengths. The appropriate intensity was found by observing the intensity of the terrylene G-band as a function of temperature and using its fitted model from figure 8.10 as an intensity scaling factor.

The detailed process for the creation of empirical terrylene models is described in section 8.4.

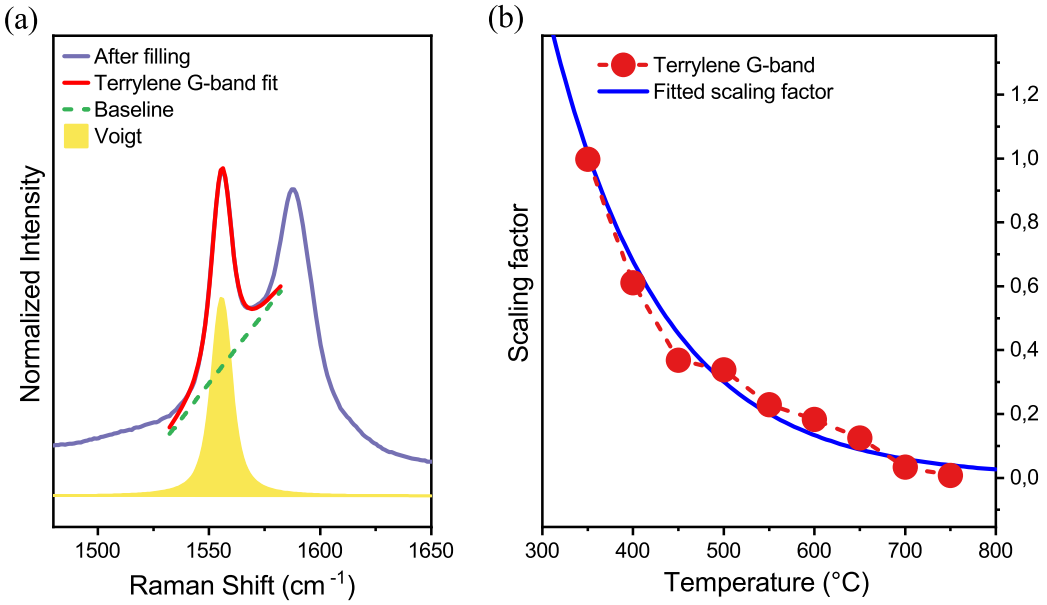

Figure 8.10: (a) The G-band of terrylene at 1555 cm^{-1} (yellow) was extrapolated from the experimental spectra (purple) by fitting a Voigt profile (red) over a linear baseline (green). (b) The peak's intensity, correspondent to the height of the fitted Voigt, is found for all annealing temperatures. Its evolution as a function of temperature is fitted by an exponential decay, which is used as scaling factor in subsequent analysis.

8.4 Empirical Terrylene Model for Subtraction

In order to properly highlight the Raman features of 5-AGNR@SWCNT over those of the last mono-layer of terrylene, the spectrum of the latter must be suitably subtracted from the Raman fingerprint of the samples.

Because of excess fluorescence, a detailed terrylene spectrum is only available at exciting wavelength 785 nm. In order to subtract correctly the signal of terrylene from spectra acquired with other exciting wavelengths, we used the fit from section 8.1.1 to construct an empirical model.

A spectral feature in Raman spectra can be approximated with a Voigt profile, which is a convolution of a Gaussian and a Cauchy-Lorentz distributions. Its full width at half maximum (FWHM), extimated with equation (6.1), is a function of the Gaussian width w_G and of the Lorentzian width w_L.

w_G depends on the laser emission linewidth and on the spectrometer resolution, while w_L depends on vibrational lifetime and Raman resonance. These influences must be taken into account when building an empirical model.

The terrylene G-line at 1555 cm^{-1} had to be isolated in each spectrum after filling in order to be used as reference. Thus I subtracted an appropriate spectrum from the after filling spectra:

- either the spectrum of pristine SWCNTs, if the shape of the SWCNT G-band was unchanged before and after filling, as is the case for 568nm;
- otherwise, for 633nm, the spectrum of the sample annealed at 600 °C .

The example in figure 8.11a shows the subtraction process for the 633 nm wavelength. The terrylene line at 1555 cm^{-1} thus found was fit with a Voigt profile with the correct w_G for the exciting wavelength. This fitting allowed me to find the broadening factor b_l to the w_L component due the different Raman resonance and detect possible shifts in spectral calibrations.

The fitted model of crystalline terrylene acquired at 785 nm found in section 8.1.1 was used as base for the empirical model. Each Voigt profile was modified in the following way:

- the Gaussian width w_G was set at the value found by Gaussian fitting of elastic scattering detected at 0 cm^{-1};
- the Lorentzian width w_L was multiplied by the broadening factor b_l;
- the intensity was multiplied by the scaling factor found in figure 8.10b;
- finally, calibration shifts were compensated for.

An example of this procedure for the empirical model at 633 nm is summarized in figure 8.11b.

The empirical model was then subtracted from the experimental spectra.

8.5 Unraveling the 5-AGNR@SWCNT Fingerprint

This empirical procedure allowed us to highlight other peaks that can be attributed to neither terrylene nor SWCNT, but consequently belong to 5-AGNR. The most prominent CH-vibration is confirmed to be the peak at 1230 cm^{-1}, previously found in the peak deconvolution reported in Figure 8.6, which we name $CH_{1,GNR}$.

Especially interesting is the peak found at 1272 cm^{-1} before subtraction: it seems to downshift about 10 wave-numbers with increasing temperature in the unmodified spectra. With the help of the subtraction procedure it becomes apparent that this is due to the superposition of a CH mode of 5-AGNR@SWCNT at 1266 cm^{-1}, which we name $CH_{2,GNR}$, and a peak from terrylene at 1272 cm^{-1}. Additional GNR@SWCNT modes include a CH mode which we called $CH_{3,GNR}$ at 1294 cm^{-1}, DLM_{GNR} at 1350 cm^{-1}, and the RBLM-adjacent mode at 492 cm^{-1} mentioned above. A summary of CH-modes for both terrylene and 5-AGNR@SWCNT is available in table 8.3.

In figure 8.13a I repeated the lineshape analysis on the peaks at 492 cm^{-1} and 1230 cm^{-1} in the spectra after subtraction and observed their intensity evolution as function of the annealing temperature. They are stable until heating at temperatures between 550 °C and 600 °C , while their intensity decays linearly at higher temperatures (see figure 8.13b).

The lineshape analysis confirms the different origins of the terrylene G-band and the peaks at 492 cm^{-1} and 1230 cm^{-1} , thus the assignation of the latter features as modes of 5-AGNR@SWCNT is correct. Moreover, the hybrid structure GNR@SWCNT is stable under heating until temperatures between 550 °C and 600 °C , after which the decrease in signal-to-noise ratio points to the decomposition of GNRs into amorphous carbon, until the thermal energy supplied is enough to form inner SWCNTs.

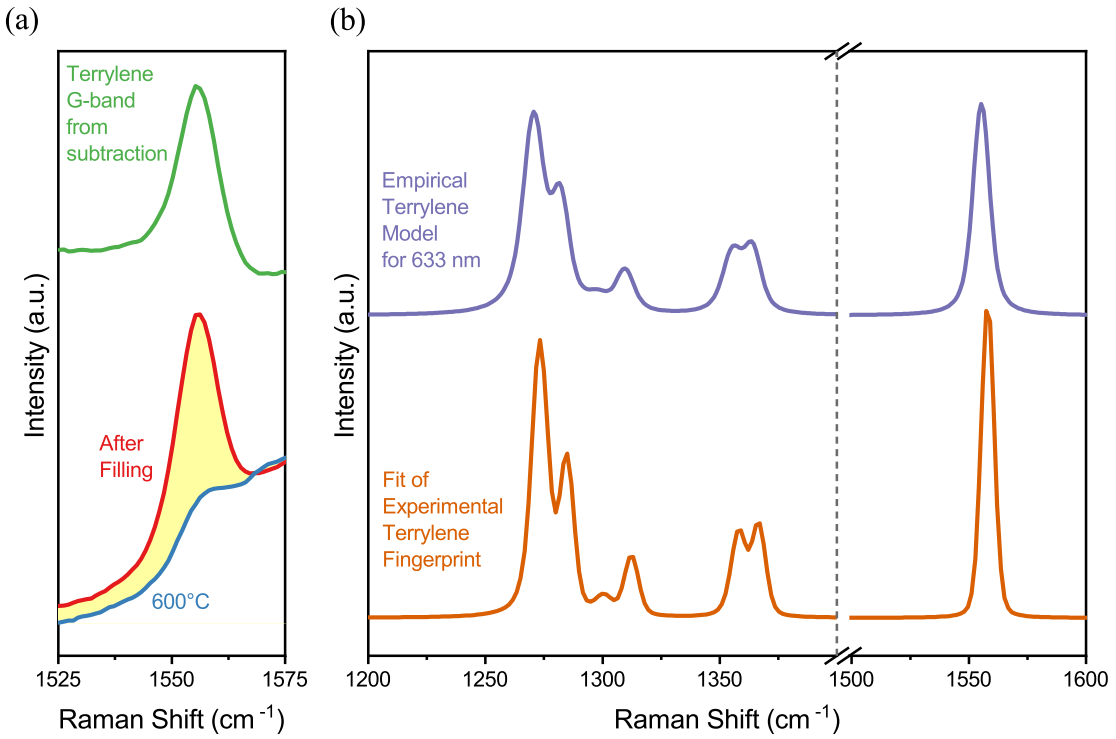

Figure 8.11: Creation of the empirical terrylene model for the 633 nm wavelength. (a) The difference between spectra after filling (red spectrum) and after annealing at 600 °C (blue spectrum) is computed. The resulting peak is the extrapolated G-band of terrylene, which is then fitted to a Voigt profile to find the width broadening factor b_l and possible calibration shifts. (b) The data found in (a) is used to adapt the fitted model for the experimental terrylene fingerprint found in section 8.1.1 to the wavelength under examination.

Comparing the dependence on temperature of both terrylene and the hybrid system 5-AGNR@SWCNT signals in Figures 8.10 and 8.13, we conclude that the spectra gathered after annealing at 600 °C are best suited for further peak analysis, as the 5-AGNR signal has just started to decrease, while the terrylene signal is already below 20% its original intensity.

8.6 Comparison to DFT Computed Spectra

Raman spectra were computed for 5-AGNR@SWCNT whose edges were terminated by one H atom by Prof. Manuel Melle-Franco and Jorge Laranjeira.

Figure 8.14 compares the spectrum of a hybrid system sample annealed 600 °C gathered at exciting wavelength of 785 nm to computed DFT spectra of 5-AGNR@(19,0) semiconducting SWCNT and 5-AGNR@(18,0) metallic SWCNT. Computed GNR edges were passivated with one H atom. The highest intensity signal of 5-AGNR@(19,0) is predicted to be the G-band, followed by CH-modes at 1234 cm^{-1} and 1280 cm^{-1}, with a small side mode at 1298 cm^{-1}. On the other hand, the G-band signal of 5-AGNR@(18,0) is quenched, highest contribution from mode 1280 cm^{-1} and 1298 cm^{-1},

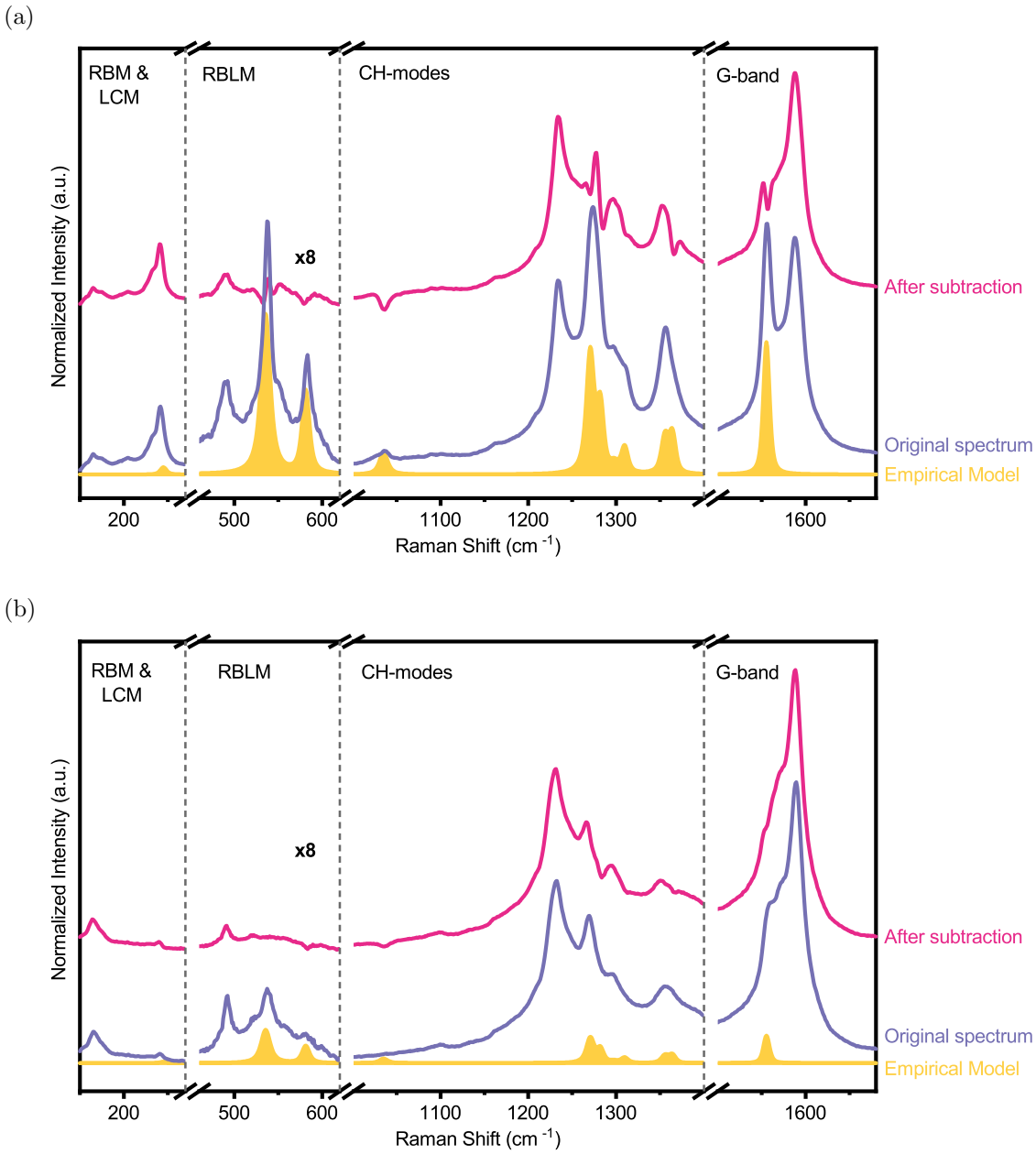

Figure 8.12: From the terrylene spectrum at 785 nm (green) multiplied by the scaling factor, we build an empirical model for exciting wavelength 633 nm (yellow). The empirical model is then multiplied by the scaling factor and subtracted from the spectra at 633 nm (purple). The resulting spectra (pink) highlights modes belonging only to GNR@SWCNT. Process shown for (a) after filling and (b) after annealing at 600 °C.

Terrylene@633 nm		5-AGNR@785 nm	
CH-mode	Position (cm^{-1})	CH-mode	Position (cm^{-1})
-	-	$CH_{1,GNR}$	1230
$CH_{1,Ter}$	1272	$CH_{2,GNR}$	1266
	1285		
$CH_{2,Ter}$	1299	$CH_{3,GNR}$	1294
	1313		
DLM_{Ter}	1359	DLM_{GNR}	1350
	1367		

Table 8.3: The dominant CH-modes of terrylene and 5-AGNRs are listed. They were measured at the resonance laser line of terrylene at 633 nm and 5-AGNR at 785 nm. Because of symmetry breaking effects, the CH lines of Terrylene have additonal peak compared to GNRs

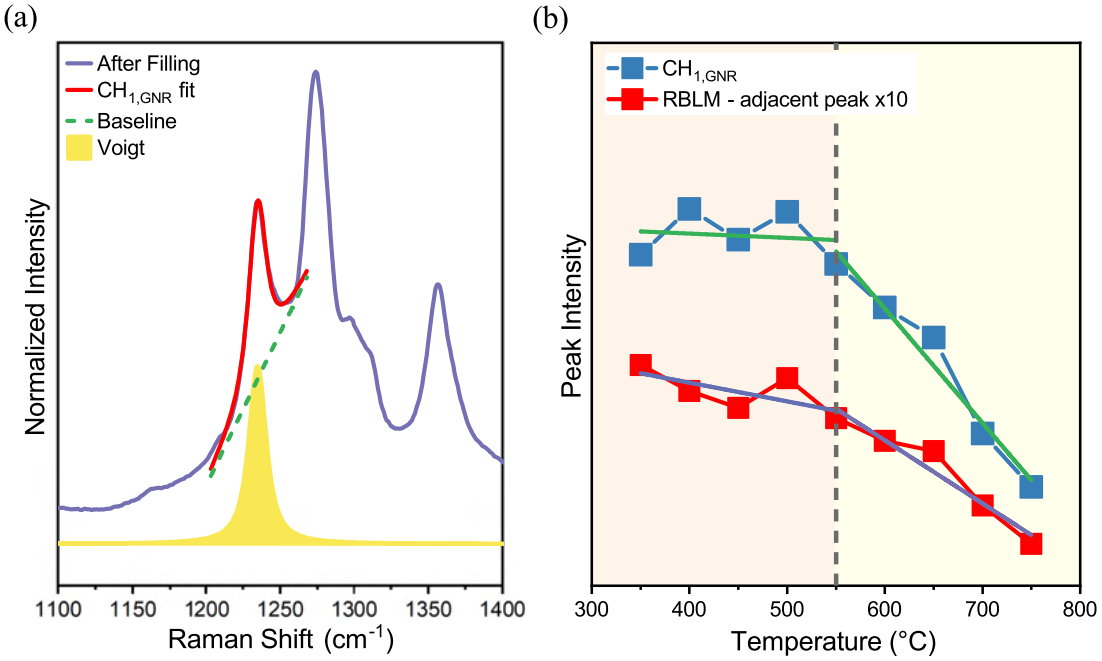

Figure 8.13: (a) The $CH_{1,GNR}$ mode of 5-AGNR at 1230 cm^{-1} (yellow) was extrapolated from the experimental spectra (purple) by fitting a Voigt curve (red) over a linear baseline (green). The same procedure was repeated for the RBLM-adjacent mode at 492 cm^{-1} (not shown). This process allowd us to find (b) intensities for $CH_{1,GNR}$ mode and RBLM (multiplied by 10). The intensities are stable (orange area) until annealing at about 550 °C. For higher annealing temperatures the signal loses intensity (yellow area). Thus GNR@SWCNT are stable until about 550 °C, after which they start to convert into amorphous carbon inside SWCNTs. Process shown for exciting wavelength 633 nm.

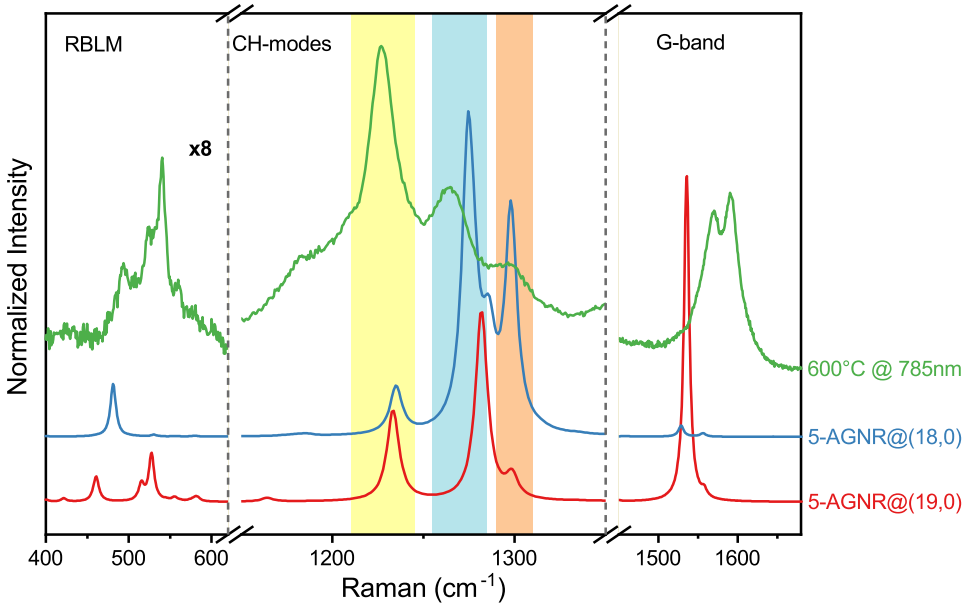

Figure 8.14: Comparison between DFT computed spectra of 5-AGNR@(19,0) semiconducting SWCNT and 5-AGNR@(18,0) metallic SWCNT to encapsulated 5-AGNR@SWCNT annealed at 600 °C gathered at 785 nm. The calculated positions of major CH vibrations are consistent with experimental data, with the peaks at 1230 cm^{-1} (highlighted in yellow) and 1266 cm^{-1} (highlighted in blue) being a superposition of signals from 5-AGNR encapsulated both in metallic and semiconducting SWCNTs, while the biggest contribution to the peak at 1294 cm^{-1} comes from 5-AGNR encapsulated in metallic SWCNTs (highlighted in orange).

followed by mode at 1234 cm^{-1}, then by RBLM at 534 cm^{-1} and SWCNT mode at 480 cm^{-1}, all of which are stronger than the G-line. Additional modes arise in the low-frequency region of encapsulated system, also due to the contribution of the encapsulating SWCNT. One such modes is the RBLM-adjacent mode at 492 cm^{-1}, which represents an asymmetric nanotube vibration. A second mode originating from mixed nanotube-nanoribbon vibration is found at 205 cm^{-1} in the computed spectrum of 5-AGNR@(18,0).

In summary, we were able to assign CH-vibrational modes to specific vibrations in the hybrid system 5-AGNR@SWCNT. This comparison with theory also allowed us to demonstrate that the edges of synthesized 5-AGNR@SWCNT are terminated with one H atom, which is consistent with the expected outcome of terrylene polymerization.

Chapter 9

Summary and Outlook

In conclusion, in my thesis I investigated two metal-free bottom-up synthesis methods of graphene nanoribbons using photoselective resonance Raman spectroscopy as a contact free characterization method.

Firstly, I used laser annealing coupled with Raman microscopy to investigate the step-by-step graphitization of a new fluorinated precursor, therefore creating a template for future investigation into the cyclodehydrofluorination reaction.

I reported for the first time the experimental and computed Raman fingerprints of the fluorinated precursor tetrafluoro-diphenyl-quinquephenyl (TDQ). TDQ was processed in a pilot study on laser annealing as a pathway to induce heat- and photo-induced reactions in fluorinated precursors. During the process, we found evidence that the molecule underwent photo-induced cyclodehydrofluorination, though the high laser irradiance led to the almost immediate decay into amorphous carbon of the reaction products. Further studies will be required on the TDQ molecule and related fluorinated precursors to optimize the laser annealing process.

Laser annealing allows to influence the reaction by laser irradiation, while at the same time providing quick, *in-situ* measurements of the Raman fingerprint without requiring a metallic substrate or physical contact between probe and reagents. Therefore, it was demonstrated to be the perspective technique to optimize nanographene synthesis through cyclodehydrofluorination and unravel its full potential in engineering tailored bottom-up synthesized GNR.

Secondly, encapsulation of a small rylene dye, terrylene, into SWCNTs with small diameter distributions allowed me to investigate the vibrational properties tied to edge terminations of small width armchair graphene nanoribbon, disentangling them from the signal of the precursor.

I demonstrated successful encapsulation of terrylene into 1.4 nm diameter SWCNT and concomitant transformation into 5-AGNR@SWCNT. These results strongly suggest that using terrylene as a precursor molecule encapsulated in SWCNTs represents a viable pathway to produce truly width-controlled armchair nanoribbons.

Moreover, I used photoselective multifrequency resonance Raman spectroscopy to investigate the samples, from which we identified the presence of multiple molecular species, leading to the identification of possible new GNR features. The resonance observed suggest that the electronic gap of 5-AGNR is in a suitable range for integration in current nanodevices technology.

To confirm the different origin of the peaks, samples were subjected to a heat treatment. This procedure allowed me to untangle terrylene-related peaks from the Raman fingerprint of 5-AGNR@SWCNT by creating a subtraction procedure to highlight CH vibrations belonging to the hybrid encapsulated system. We were thus able to unravel for the first time the Raman signal of encapsulated GNR from that of the precursor.

I identified the evolution as a function of temperature of isolated modes belonging to 5-AGNR@SWCNT, thus finding the goldilocks annealing temperature that would allow to study the samples free of the influence of residual not-encapsulated terrylene. I determined that 600 °C is the ideal annealing temperature for sublimation of residual terrylene monolayer without damage to 5-AGNR@SWCNT.

Finally, I compared the experimental data to computed spectra of 5-AGNR @ 1.4 nm SWCNT, which predict the experimental results remarkably well and demonstrate that synthesized 5-AGNR@SWCNT are terminated with one H atom.

9.1 Outlook

Both techniques show great potential for future investigations.

The fluorinated molecule TDQ has the potential to allow synthesis of GNR if the correct substrate for adsorption is found. Both this molecule and its related fluorinated precursors can be heated via laser annealing and studied *in-situ* via concomitant resonance Raman.

Encapsulation of small molecules in SWCNT has the potential to allow synthesis of extremely different species of long homogeneous GNR. I believe that the analysis method I reported will be pivotal for future Raman characterization the hybrid system GNR@SWCNT unravelled from its precursor's fingerprint.

Appendix A

Additional data on TDQ

A.1 AFM measurements of TDQ@MgO

Atomic force microscopy (AFM) measurements of TDQ@MgO were carried out by Dr. Wim Cuypers at the Department of Chemistry of the University of Vienna.

Further testing went into finding an appropriate surface for cyclodehyodrofluorination (CDHF).

I used a custom made evaporator built inside a UHV chamber to deposit the tetrafluoro-diphenyl-quinquephenyl (TDQ) precursor on a magnesium oxide substrate. Pressure during evaporation was better than 10^{-6} mbar. The TDQ precursor was deposited in a quartz vial connected to the UHV chamber and heated with a custom-built coil heater connected to a voltage generator. The temperature was monitored with a custom built thermocouple.

AFM measurements of TDQ@MgO were carried out by Dr. Wim Cuypers, depicted in figure A.1. Unfortunately, the deposition procedure did not yield a smooth monolayer. Instead it led to islands with a base diameter in the order of 2 nm and a height of several tens of nanometers.

These conditions are not ideal for testing CDHF on insulator surfaces. Further testing will have to be carried out to determine the best insulating substrate for TDQ deposition.

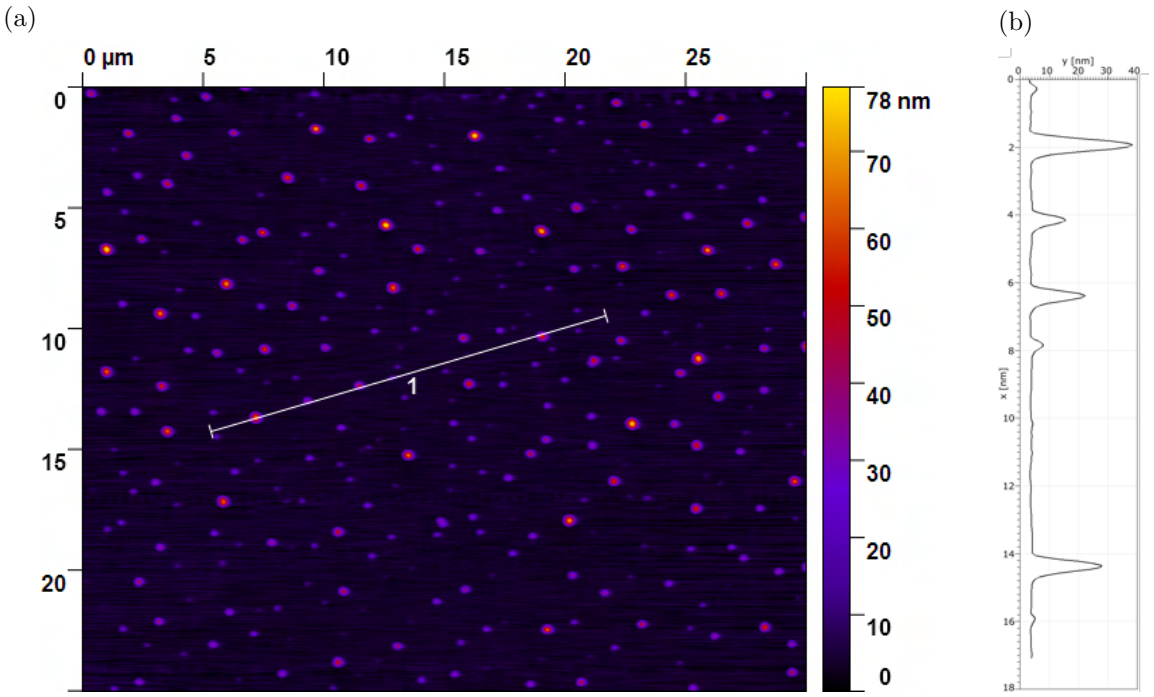

Figure A.1: (a) Heat map of AFM of TDQ@MgO . (b) AFM profile of TDQ@MgO along the line highlighted in (a).

A.2 Numerical Results of Temperature Calculations

Numerical results of temperature calculations, reported graphically in section 7.3.2, are in table A.1.

	$A = 3$		$A = 4$	
Cycle	Temperature (K)	σ_T (K)	Temperature (K)	σ_T (K)
1	1016,26	130,93	983,88	145,78
2	1166,80	129,19	1134,98	142,65
3	1178,74	129,25	1146,91	142,66
4	1102,46	129,37	1070,54	143,27
5	1132,09	129,22	1100,23	142,90
6	966,62	132,57	933,76	148,23
7	965,30	132,62	932,43	148,30
8	1030,19	130,47	997,94	145,11
9	918,81	135,17	885,23	151,93
10	988,11	131,79	955,48	147,07
11	1021,03	130,76	988,69	145,54
12	1041,80	130,28	1009,61	144,80
13	854,08	140,42	819,02	159,38
14	999,76	131,47	967,23	146,58
15	703,12	165,89	660,72	197,80
16	903,79	136,29	869,90	153,50
17	790,98	148,14	753,75	170,55
18	747,42	155,65	708,03	181,78
19	634,36	189,60	584,65	238,81
20	685,58	170,98	641,66	206,07
21	689,01	169,98	645,40	204,42
22	670,74	175,88	625,33	214,27
23	676,54	174,01	631,70	211,09
24	330,20	1248,19	–	–
25	657,24	180,69	610,36	222,58
26	–	–	–	–
27	–	–	–	–
28	484,54	323,51	372,14	828,69
29	570,83	226,30	508,52	317,92
30	–	–	–	–
31	–	–	–	–
32	408,17	536,02	–	–

Table A.1: Temperatures and standard deviations calculated with eqq. 7.2 and 7.3

Appendix B

Additional Data on Encapsulated 5-AGNR@SWCNT

B.1 Diameter of Inner SWCNT Synthesized via Heat Treatment

In order to confirm successful encapsulation of terrylene into SWCNTs, I subjected the hybrid sample to heat treatment at 1550°C to synthesize inner tubes. RBMs of syntesized DWCNTs with many inner tube diameters are visible in the Raman spectra in figure 8.3a.

The diameter of the inner tubes formed under heat treatment can be calculated with the formula [173]:

$$d = 234/(\omega_{\mathrm{RBM}} - 10) \tag{B.1}$$

Results are in table B.1.

Raman Shift (cm^{-1})	Calculated diameter (nm)
239	1,02
251	0,97
265	0,92
273	0,89
279	0,87
289	0,84
297	0,82
305	0,79
309	0,78
334	0,72

Table B.1: Calculated diameters of inner SWCNTs synthesized by heat treatment.

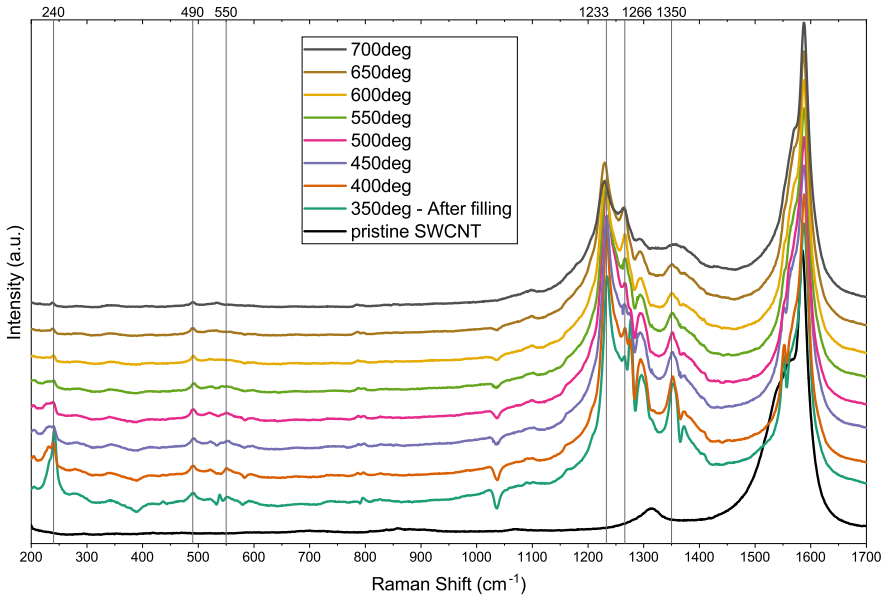

Figure B.1: Spectra acquired at exciting wavelength 633 nm, after subtraction the empirical terrylene model.

B.2 Spectra after Subtraction of Terrylene Empirical Model

Spectra acquired at exciting wavelength 633 nm, after subtraction the empirical terrylene model are in figure B.1. The SWCNT spectrum was not subtracted because of a broadening after filling, which would have led to negative values between 1500 cm^{-1} and 1550 cm^{-1}.

The peaks at 492 cm^{-1} and 1233 cm^{-1} were not influenced by the subtraction, which confirms they are modes of 5-AGNR@SWCNT. After subtraction, the peaks at 1266 cm^{-1}, 1294 cm^{-1} and 1350 cm^{-1} were isolated, which are also modes of 5-AGNR@SWCNT.

As the dielectric environment for mono–layer terrylene outside SWCNT is different from that of van der Waals crystals of terrylene, the empirical model has a limit in the precision with which it predicts position and intensity of the individual peaks. One example is the dip present after filling at 390 cm^{-1}. Imperfections in the empirical model of terrylene led to negative values in some areas where the peak intensity was imperfectly predicted. Moreover, a peak at 240 cm^{-1} is still present after subtraction: this is probably due to an imperfect prediction of position and intensity for the terrylene LCM.

Despite the imperfections, this method is a powerful tool to highlight Raman features belonging to 5-AGNR@SWCNT.

Spectra acquired at exciting wavelength 568 nm, after subtraction the empirical terrylene model and of the pristine SWCNT spectrum are in figure B.2. Similar considerations to those in the previous paragraph can be made.

The procedure works best with 633 nm spectra because the peak used for creating the model, the G-band of terrylene at 1555 cm^{-1}, has high relative intensity.

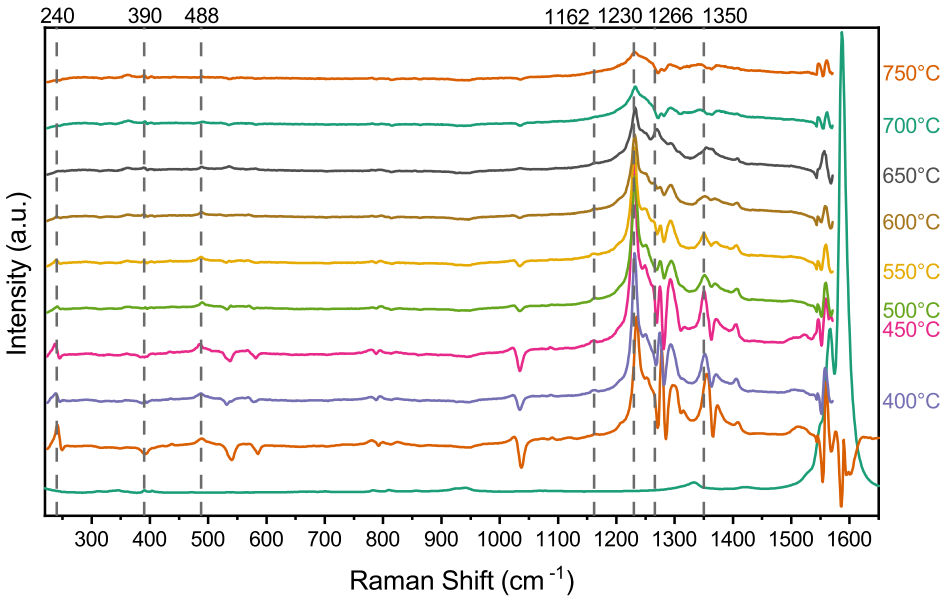

Figure B.2: Spectra acquired at exciting wavelength 568 nm, after subtraction of SWCNT spectra and empirical terrylene model.

Acknowledgements

No man is an island, entire of itself.
John Donne

This manuscript is the result of three years of my own work, but its existence would have been impossible without many people that have supported me in its preparation and during the long months of the COVID-19 pandemic.

I would like to start by thanking my colleagues, with whom I am glad to have shared my time in Vienna.

My supervisor, Prof. Thomas Pichler, helped me define my projects, and was always available for discussion, especially if it involved a freshly brewed cup of coffee. He gave me opportunities I had never expected and helped me develop my skills as an independent scientist.

Prof. Paola Ayala showed me that professorship is not an unreachable goal for a woman and taught me the importance of presenting one's own work in the proper way.

Dr. Christian Kramberger Kaplan shared with me some of his vast knowledge on Raman spectroscopy and taught me how to properly align a laser.

Dr. Juan Carlos Moreno López taught me about ultra-high vacuum systems both in Vienna and at the Laboratório Nacional de Luz Síncrotron in Campinas.

Dr. Filippo Fedi, Dr. Carlos Reinoso and Dr. Johnny Chimborazo introduced me to the lab. Dr. Hidetsugu Shiozawa and Dr. Oleg Domanov taught me how to encapsulate small molecules inside single-walled carbon nanotubes, and also were sometimes in charge of the cookies and ice cream.

Ivan Verbitskii, Claudia Berkmann, Bernd Aichner, Shiraz Ahmed Siddiqui and Weili Cui were there for all my successes and failures in the lab, and for all the above mentioned cookies and ice cream.

Clara Freytag, Joselyn Benalcazar and Eva Gabriela Röck made me see that teaching is not so scary when a bright mind is listening.

Christin Schuster and Dido Denier van der Gon came later, but were always ready with a smile.

I thank Stefan Loyer, Andreas Stangl and Eva Deutsch, who relentlessly take care of practical and bureaucratic matters and who are invaluable to the continuing operations of the laboratory. I thank Christian Vlcek for being always able to find liquid nitrogen.

I am grateful to all of you for your readiness to help and for the good time we had together.

I thank Prof. Lei Shi and Dr. Yifan Zhang of the Sun Yat-sen University in Guangzhou for being present even from a continent away.

I am grateful to Prof. Abner de Siervo and Rodrigo Ferreira of the University of Campinas and Pedro Schio for their guidance during beamtime at the Laboratório Nacional de Luz Síncrotron.

I thank Dr. Ann-Kristin Steiner, Prof. Konstantin Amsharov and Prof. Kazuhiro Yanagi for suppling the materials I worked on in this thesis, and Prof. Manuel Melle Franco and Jorge Laranjeira for confirming my experimental data with calculations.

I would like to thank Prof. Dieter Baurecht and Dr. Stefan Puchegger for giving me access to the Faculty Center for Nano Structure Research of the University of Vienna and training me to use the WiTech Alpha 300A AFM/Raman system.

I thank Dr. Christiane Maria Losert-Valiente Kroon and Viktoria Erben of the Vienna Doctoral School, for their invaluable help in navigating the PhD prior and especially during the pandemic. I thank Prof. Jani Kotakoski for agreeing to be my second mentor, advising me on how to deal with my work.

Finally, I thank my family, who gave me strength with their love, even when the whole world around us seemed hopeless: my lovely husband Simone, my parents Alessandra and Edoardo with their steadfast faith in my abilities, my brother Giancarlo who bore patiently my questions while working on a thesis of his own, and my family-in-law Viviana, Ilario and Loris.

To all those who helped me produce this manuscript or who just kept me sane during lockdown after lockdown, I dedicate this thesis.

Abbreviation and Nomenclature

Abbreviations

AC-HRTEM . aberration-corrected high resolution transmission electron microscopy
AFM ..... atomic force microscopy
AGNR ..... armchair graphene nanoribbon
BSE ..... Bethe-Salpeter equation
BUS ..... bottom-up synthesis
CDHF ..... cyclodehyodrofluorination
CDH ..... cyclodehyodrogenation
CNT ..... carbon nanotube
CVD ..... chemical vapour deposition
DCM ..... dichloromethane
DFT ..... density functional theory
DGU ..... density-gradient ultracentrifugation
DLM ..... D-like mode
DoS ..... density of states
DWCNT ..... double-walled carbon nanotube
FET ..... field-effect transistor
FT ..... Fourier-Transform
FWHM ..... full width at half maximum
GNR ..... graphene nanoribbon
GNR@SWCNT ..... graphene nanoribbons inside single-walled carbon nanotube
GW ..... Green-Coulomb approximation
HV ..... high vacuum
IC ..... image charge
IR ..... infrared
LCM ..... longitudinal compressive mode
LDA ..... local-density approximation
MWCNT ..... multi-walled carbon nanotube
NG ..... nanographene
NIR ..... near infrared
OA ..... optical absorption

RBM ..... radial breathing mode
RBLM ..... radial breathing-like mode
RDS ..... reflectance difference spectroscopy
PL ..... photoluminescence
SDS ..... sodium dodecyl sulfate
SNR ..... signal-to-noise ratio
SLM ..... shear-like mode
STM ..... scanning tunnelling microscopy
STs ..... scanning tunnelling spectroscopy
SWCNT ..... single-walled carbon nanotube
TDQ ..... tetrafluoro-diphenyl-quinquephenyl
TEM ..... transmission electron microscopy
UHV ..... ultra-high vacuum
UV ..... ultra-violet
WDRS ..... wavelength dependent Raman spectroscopy
ZGNR ..... zigzag graphene nanoribbon

Nomenclature

b_l ..... broadening factor

C_{60} ..... buckminsterfullerene

$\vec{C}_h$ ..... chiral vector

HF ..... hydrogen fluoride

w_G ..... Gaussian width

w_L ..... Lorentzian width

Bibliography

[1] S. Kumar, "Fundamental limits to Moore's law," Nov. 2015.

[2] H. N. Khan, D. A. Hounshell, and E. R. H. Fuchs, "Science and research policy at the end of Moore's law," *Nature Electronics*, vol. 1, pp. 14–21, jan 2018.

[3] A. D. Franklin, "The road to carbon nanotube transistors," *Nature*, vol. 498, pp. 443–444, jun 2013.

[4] A. A. Ouahabi, J.-A. Amalian, L. Charles, and J.-F. Lutz, "Mass spectrometry sequencing of long digital polymers facilitated by programmed inter-byte fragmentation," *Nature Communications*, vol. 8, oct 2017.

[5] K. S. Novoselov, "Electric field effect in atomically thin carbon films," *Science*, vol. 306, pp. 666–669, oct 2004.

[6] K. S. Novoselov, A. K. Geim, S. V. Morozov, D. Jiang, M. I. Katsnelson, I. V. Grigorieva, S. V. Dubonos, and A. A. Firsov, "Two-dimensional gas of massless Dirac fermions in graphene," *Nature*, vol. 438, pp. 197–200, nov 2005.

[7] E. Gerstner, "Nobel Prize 2010: Andre Geim & Konstantin Novoselov," *Nature Physics*, vol. 6, pp. 836–836, oct 2010.

[8] A. Hirsch, "The era of carbon allotropes," *Nature Materials*, vol. 9, pp. 868–871, oct 2010.

[9] A. Jorio, R. Saito, G. Dresselhaus, and M. S. Dresselhaus, *Raman Spectroscopy in Graphene Related Systems*. Wiley-VCH Verlag GmbH & Co. KGaA, jan 2011.

[10] L. Ding, S. Liang, T. Pei, Z. Zhang, S. Wang, W. Zhou, J. Liu, and L.-M. Peng, "Carbon nanotube based ultra-low voltage integrated circuits: Scaling down to 0.4 V," *Applied Physics Letters*, vol. 100, p. 263116, jun 2012.

[11] H. C. Chin, C. S. Lim, W. S. Wong, K. A. Danapalasingam, V. K. Arora, and M. L. P. Tan, "Enhanced device and circuit-level performance benchmarking of graphene nanoribbon field-effect transistor against a nano-MOSFET with interconnects," *Journal of Nanomaterials*, vol. 2014, pp. 1–14, 2014.

[12] A. Kumari, S. Rani, and B. Singh, "Parameterized comparison of nanotransistors based on CNT and GNR materials: Effect of variation in gate oxide thickness and dielectric constant," *Journal of Electronic Materials*, vol. 48, pp. 3078–3085, feb 2019.

[13] S. Z. Ahmed, M. S. Shawkat, M. I. H. Chowdhury, and S. M. Mominuzzaman, "Current-voltage characteristics of ballistic Schottky barrier GNRFET and CNTFET: Effect of relative dielectric constant," in *10th IEEE International Conference on Nano/Micro Engineered and Molecular Systems*, IEEE, apr 2015.

[14] J. P. Llinas, A. Fairbrother, G. Borin Barin, W. Shi, K. Lee, S. Wu, B. Yong Choi, R. Braganza, J. Lear, N. Kau, W. Choi, C. Chen, Z. Pedramrazi, T. Dumslaff, A. Narita, X. Feng, K. Müllen, F. Fischer, A. Zettl, P. Ruffieux, E. Yablonovitch, M. Crommie, R. Fasel, and J. Bokor, "Short-channel field-effect transistors with 9-atom and 13-atom wide graphene nanoribbons," *Nature Communications*, vol. 8, p. 633, Sept. 2017.

[15] K. Kamarás and À. Pekker, *Identification and separation of metallic and semiconducting carbon nanotubes*. Oxford University Press, jul 2017.

[16] J. Cai, C. A. Pignedoli, L. Talirz, P. Ruffieux, H. Söde, L. Liang, V. Meunier, R. Berger, R. Li, X. Feng, K. Müllen, and R. Fasel, "Graphene nanoribbon heterojunctions," *Nature Nanotechnology*, vol. 9, pp. 896–900, sep 2014.

[17] G. D. Nguyen, H.-Z. Tsai, A. A. Omrani, T. Marangoni, M. Wu, D. J. Rizzo, G. F. Rodgers, R. R. Cloke, R. A. Durr, Y. Sakai, F. Liou, A. S. Aikawa, J. R. Chelikowsky, S. G. Louie, F. R. Fischer, and M. F. Crommie, "Atomically precise graphene nanoribbon heterojunctions from a single molecular precursor," *Nature Nanotechnology*, vol. 12, p. 1077, Sept. 2017.

[18] C. Ma, L. Liang, Z. Xiao, A. A. Puretzky, K. Hong, W. Lu, V. Meunier, J. Bernholc, and A.-P. Li, "Seamless staircase electrical contact to semiconducting graphene nanoribbons," *Nano Letters*, vol. 17, pp. 6241–6247, sep 2017.

[19] J. Overbeck, G. B. Barin, C. Daniels, M. L. Perrin, L. Liang, O. Braun, R. Darawish, B. Burkhardt, T. Dumslaff, X.-Y. Wang, A. Narita, K. Müllen, V. Meunier, R. Fasel, M. Calame, and P. Ruffieux, "Optimized substrates and measurement approaches for Raman spectroscopy of graphene nanoribbons," *physica status solidi (b)*, vol. 256, p. 1900343, nov 2019.

[20] M. Kolmer, A. Steiner, I. Izydorczyk, W. Ko, M. Engelund, M. Szymonski, A.-P. Li, and K. Amsharov, "Rational synthesis of atomically precise graphene nanoribbons directly on metal oxide surfaces," *Science*, vol. 369, pp. 571–575, jun 2020.

[21] L. Shi, K. Yanagi, K. Cao, U. Kaiser, P. Ayala, and T. Pichler, "Extraction of linear carbon chains unravels the role of the carbon nanotube host," *ACS Nano*, vol. 12, pp. 8477–8484, aug 2018.

[22] M. Fujita, K. Wakabayashi, K. Nakada, and K. Kusakabe, "Peculiar localized state at zigzag graphite edge," *Journal of the Physical Society of Japan*, vol. 65, pp. 1920–1923, jul 1996.

[23] K. Nakada, M. Fujita, G. Dresselhaus, and M. S. Dresselhaus, "Edge state in graphene ribbons: Nanometer size effect and edge shape dependence," *Physical Review B*, vol. 54, no. 24, pp. 17954–17961, 1996.

[24] Y. H. Lu, R. Q. Wu, L. Shen, M. Yang, Z. D. Sha, Y. Q. Cai, P. M. He, and Y. P. Feng, "Effects of edge passivation by hydrogen on electronic structure of armchair graphene nanoribbon and band gap engineering," *Applied Physics Letters*, vol. 94, p. 122111, mar 2009.

[25] G. Borin Barin, A. Fairbrother, L. Rotach, M. Bayle, M. Paillet, L. Liang, V. Meunier, R. Hauert, T. Dumslaff, A. Narita, K. Müllen, H. Sahabudeen, R. Berger, X. Feng, R. Fasel, and P. Ruffieux, "Surface-synthesized graphene nanoribbons for room temperature switching devices: Substrate transfer and ex situ characterization," *ACS Applied Nano Materials*, vol. 2, pp. 2184–2192, mar 2019.

[26] H. Kuzmany, L. Shi, M. Martinati, S. Cambré, W. Wenseleers, J. Kürti, J. Koltai, G. Kukucska, K. Cao, U. Kaiser, T. Saito, and T. Pichler, "Well-defined sub-nanometer graphene ribbons synthesized inside carbon nanotubes," *Carbon*, vol. 171, pp. 221–229, jan 2021.

[27] D. R. Klein, *Organic Chemistry*. WILEY, Dec. 2013.

[28] SinghSharp, "Why do almost all flagship smartphones have an OLED display?," Feb. 2020.

[29] H. J. Jang, J. Y. Lee, J. Kim, J. Kwak, and J.-H. Park, "Progress of display performances: AR, VR, QLED, and OLED," *Journal of Information Display*, vol. 21, pp. 1–9, jan 2020.

[30] F. Banhart, "Elemental carbon in the sp^1 hybridization," *ChemTexts*, vol. 6, dec 2019.

[31] V. Blank, M. Popov, G. Pivovarov, N. Lvova, K. Gogolinsky, and V. Reshetov, "Ultrahard and superhard phases of fullerite C_{60}: Comparison with diamond on hardness and wear," *Diamond and Related Materials*, vol. 7, pp. 427–431, feb 1998.

[32] S. Dub, P. Lytvyn, V. Strelchuk, A. Nikolenko, Y. Stubrov, I. Petrusha, T. Taniguchi, and S. Ivakhnenko, "Vickers hardness of diamond and cBN single crystals: AFM approach," *Crystals*, vol. 7, p. 369, dec 2017.

[33] R. C. Haddon, "The fullerenes: powerful carbon-based electron acceptors," *Philosophical Transactions of the Royal Society of London. Series A: Physical and Engineering Sciences*, vol. 343, pp. 53–62, apr 1993.

[34] S. Reich, J. Maultzsch, C. Thomsen, and P. Ordejón, "Tight-binding description of graphene," *Physical Review B*, vol. 66, p. 035412, jul 2002.

[35] A. A. Balandin, S. Ghosh, W. Bao, I. Calizo, D. Teweldebrhan, F. Miao, and C. N. Lau, "Superior thermal conductivity of single-layer graphene," *Nano Letters*, vol. 8, pp. 902–907, feb 2008.

[36] C. Lee, X. Wei, J. W. Kysar, and J. Hone, "Measurement of the elastic properties and intrinsic strength of monolayer graphene," *Science*, vol. 321, pp. 385–388, jul 2008.

[37] G. G. Samsonidze, A. R. Saito, D. A. Jorio, E. M. A. Pimenta, E. A. G. S. Filho, F. A. Grüneis, D. G. Dresselhaus, and M. S. Dresselhausa, "The concept of cutting lines in carbon nanotube science," *Journal of Nanoscience and Nanotechnology*, vol. 3, pp. 431–458, dec 2003.

[38] Y.-W. Son, M. L. Cohen, and S. G. Louie, "Energy gaps in graphene nanoribbons," *Physical Review Letters*, vol. 97, p. 216803, nov 2006.

[39] N. Merino-Díez, A. Garcia-Lekue, E. Carbonell-Sanromà, J. Li, M. Corso, L. Colazzo, F. Sedona, D. Sánchez-Portal, J. I. Pascual, and D. G. de Oteyza, "Width-dependent band gap in armchair graphene nanoribbons reveals Fermi level pinning on Au(111)," *ACS Nano*, vol. 11, pp. 11661–11668, oct 2017.

[40] J. Cai, P. Ruffieux, R. Jaafar, M. Bieri, T. Braun, S. Blankenburg, M. Muoth, A. P. Seitsonen, M. Saleh, X. Feng, K. Müllen, and R. Fasel, "Atomically precise bottom-up fabrication of graphene nanoribbons," *Nature*, vol. 466, p. 470, 07 2010.

[41] S. Iijima, "Helical microtubules of graphitic carbon," *Nature*, vol. 354, pp. 56–58, nov 1991.

[42] R. Saito, M. Fujita, G. Dresselhaus, and M. S. Dresselhaus, "Electronic structure of chiral graphene tubules," *Applied Physics Letters*, vol. 60, pp. 2204–2206, may 1992.

[43] A. Cadena, B. Botka, and K. Kamarás, "Organic molecules encapsulated in single-walled carbon nanotubes," *Oxford Open Materials Science*, vol. 1, nov 2020.

[44] K. Kim, J.-Y. Choi, T. Kim, S.-H. Cho, and H.-J. Chung, "A role for graphene in silicon-based semiconductor devices," *Nature*, vol. 479, pp. 338–344, nov 2011.

[45] Z. Sun, T. Hasan, F. Torrisi, D. Popa, G. Privitera, F. Wang, F. Bonaccorso, D. M. Basko, and A. C. Ferrari, "Graphene mode-locked ultrafast laser," *ACS Nano*, vol. 4, pp. 803–810, jan 2010.

[46] M. Romagnoli, V. Sorianello, M. Midrio, F. H. L. Koppens, C. Huyghebaert, D. Neumaier, P. Galli, W. Templ, A. D'Errico, and A. C. Ferrari, "Graphene-based integrated photonics for next-generation datacom and telecom," *Nature Reviews Materials*, vol. 3, pp. 392–414, oct 2018.

[47] A. Montanaro, W. Wei, D. D. Fazio, U. Sassi, G. Soavi, P. Aversa, A. C. Ferrari, H. Happy, P. Legagneux, and E. Pallecchi, "Optoelectronic mixing with high-frequency graphene transistors," *Nature Communications*, vol. 12, may 2021.

[48] S. J. Tans, A. R. M. Verschueren, and C. Dekker, "Room-temperature transistor based on a single carbon nanotube," *Nature*, vol. 393, pp. 49–52, may 1998.

[49] A. Javey, J. Guo, Q. Wang, M. Lundstrom, and H. Dai, "Ballistic carbon nanotube field-effect transistors," *Nature*, vol. 424, pp. 654–657, aug 2003.

[50] G. Hills, M. G. Bardon, G. Doornbos, D. Yakimets, P. Schuddinck, R. Baert, D. Jang, L. Mattii, S. M. Y. Sherazi, D. Rodopoulos, R. Ritzenthaler, C.-S. Lee, A. V.-Y. Thean, I. Radu, A. Spessot, P. Debacker, F. Catthoor, P. Raghavan, M. M. Shulaker, H.-S. P. Wong, and S. Mitra, "Understanding energy efficiency benefits of carbon nanotube field-effect transistors for digital VLSI," *IEEE Transactions on Nanotechnology*, vol. 17, pp. 1259–1269, nov 2018.

[51] A. D. Franklin, M. Luisier, S.-J. Han, G. Tulevski, C. M. Breslin, L. Gignac, M. S. Lundstrom, and W. Haensch, "Sub-10 nm carbon nanotube transistor," *Nano Letters*, vol. 12, pp. 758–762, jan 2012.

[52] G. J. Brady, A. J. Way, N. S. Safron, H. T. Evensen, P. Gopalan, and M. S. Arnold, "Quasi-ballistic carbon nanotube array transistors with current density exceeding Si and GaAs," *Science Advances*, vol. 2, p. e1601240, sep 2016.

[53] M. M. Shulaker, G. Hills, N. Patil, H. Wei, H.-Y. Chen, H.-S. P. Wong, and S. Mitra, "Carbon nanotube computer," *Nature*, vol. 501, pp. 526–530, sep 2013.

[54] G. Hills, C. Lau, A. Wright, S. Fuller, M. D. Bishop, T. Srimani, P. Kanhaiya, R. Ho, A. Amer, Y. Stein, D. Murphy, Arvind, A. Chandrakasan, and M. M. Shulaker, "Modern microprocessor built from complementary carbon nanotube transistors," *Nature*, vol. 572, pp. 595–602, aug 2019.

[55] O. Pitkänen, T. Järvinen, H. Cheng, G. S. Lorite, A. Dombovari, L. Rieppo, S. Talapatra, H. M. Duong, G. Tóth, K. L. Juhász, Z. Kónya, A. Kukovecz, P. M. Ajayan, R. Vajtai, and K. Kordás, "On-chip integrated vertically aligned carbon nanotube based super- and pseudocapacitors," *Scientific Reports*, vol. 7, nov 2017.

[56] R. Das, Z. Shahnavaz, M. E. Ali, M. M. Islam, and S. B. A. Hamid, "Can we optimize arc discharge and laser ablation for well-controlled carbon nanotube synthesis?," *Nanoscale Research Letters*, vol. 11, nov 2016.

[57] X. Wang, Y. Ouyang, X. Li, H. Wang, J. Guo, and H. Dai, "Room-temperature all-semiconducting sub-10-nm graphene nanoribbon field-effect transistors," *Physical Review Letters*, vol. 100, p. 206803, may 2008.

[58] A. J. Chaves, G. D. Lima, W. de Paula, C. E. Cordeiro, A. Delfino, T. Frederico, and O. Oliveira, "Dynamical gap generation in graphene nanoribbons: An effective relativistic field theoretical model," *Physical Review B*, vol. 83, p. 153405, apr 2011.

[59] Y. Yano, N. Mitoma, H. Ito, and K. Itami, "A quest for structurally uniform graphene nanoribbons: Synthesis, properties, and applications," *The Journal of Organic Chemistry*, vol. 85, pp. 4–33, dec 2019.

[60] M. H. Rashid, A. Koel, and T. Rang, "Simulations of graphene nanoribbon field effect transistor for the detection of propane and butane gases: A first principles study," *Nanomaterials*, vol. 10, p. 98, jan 2020.

[61] C. Kittel, *Introduction to Solid State Physics*. WILEY, Nov. 2004.

[62] V. Gavryushin, "Graphene brillouin zone and electronic energy dispersion." https://demonstrations.wolfram.com/GrapheneBrillouinZoneAndElectronicEnergyDispersion/, Mar. 2011.

[63] L. A. Falkovsky, "Phonon dispersion in graphene," *Journal of Experimental and Theoretical Physics*, vol. 105, pp. 397–403, aug 2007.

[64] T. Hayashi, Y. A. Kim, T. Matoba, M. Esaka, K. Nishimura, T. Tsukada, M. Endo, and M. S. Dresselhaus, "Smallest freestanding single-walled carbon nanotube," *Nano Letters*, vol. 3, pp. 887–889, jul 2003.

[65] A. C. Torres-Dias, T. F. Cerqueira, W. Cui, M. A. Marques, S. Botti, D. Machon, M. A. Hartmann, Y. Sun, D. J. Dunstan, and A. San-Miguel, "From mesoscale to nanoscale mechanics in single-wall carbon nanotubes," *Carbon*, vol. 123, pp. 145–150, oct 2017.

[66] K. Sato, R. Saito, J. Jiang, G. Dresselhaus, and M. S. Dresselhaus, "Discontinuity in the family pattern of single-wall carbon nanotubes," *Physical Review B*, vol. 76, p. 195446, nov 2007.

[67] A. R. T. Nugraha, R. Saito, K. Sato, P. T. Araujo, A. Jorio, and M. S. Dresselhaus, "Dielectric constant model for environmental effects on the exciton energies of single wall carbon nanotubes," *Applied Physics Letters*, vol. 97, p. 091905, aug 2010.

[68] S. Maruyama, "Kataura-plot for resonant Raman." http://www.photon.t.u-tokyo.ac.jp/~maruyama/kataura/kataura.html.

[69] A. R. Carvalho, J. H. Warnes, and C. H. Lewenkopf, "Edge magnetization and local density of states in chiral graphene nanoribbons," *Physical Review B*, vol. 89, jun 2014.

[70] O. V. Yazyev, R. B. Capaz, and S. G. Louie, "Theory of magnetic edge states in chiral graphene nanoribbons," *Physical Review B*, vol. 84, sep 2011.

[71] R. Gillen, M. Mohr, C. Thomsen, and J. Maultzsch, "Vibrational properties of graphene nanoribbons by first-principles calculations," *Physical Review B*, vol. 80, no. 15, p. 155418, 2009.

[72] S. M. Loh, Y.-H. Huang, K.-M. Lin, W. S. Su, B. R. Wu, and T. C. Leung, "Quantum confinement effect in armchair graphene nanoribbons: Effect of strain on band gap modulation studied using first-principles calculations," *Physical Review B*, vol. 90, jul 2014.

[73] P. Ruffieux, S. Wang, B. Yang, C. Sánchez-Sánchez, J. Liu, T. Dienel, L. Talirz, P. Shinde, C. A. Pignedoli, D. Passerone, T. Dumslaff, X. Feng, K. Müllen, and R. Fasel, "On-surface synthesis of graphene nanoribbons with zigzag edge topology," *Nature*, vol. 531, p. 489, Mar. 2016.

[74] W.-X. Wang, M. Zhou, X. Li, S.-Y. Li, X. Wu, W. Duan, and L. He, "Energy gaps of atomically precise armchair graphene sidewall nanoribbons," *Physical Review B*, vol. 93, p. 241403, jun 2016.

[75] P. Ruffieux, J. Cai, N. C. Plumb, L. Patthey, D. Prezzi, A. Ferretti, E. Molinari, X. Feng, K. Müllen, C. A. Pignedoli, and et al., "Electronic structure of atomically precise graphene nanoribbons," *ACS Nano*, vol. 6, pp. 6930–6935, Aug 2012.

[76] R. Denk, M. Hohage, P. Zeppenfeld, J. Cai, C. A. Pignedoli, H. Söde, R. Fasel, X. Feng, K. Müllen, S. Wang, D. Prezzi, A. Ferretti, A. Ruini, E. Molinari, and P. Ruffieux, "Exciton-dominated optical response of ultra-narrow graphene nanoribbons," *Nature Communications*, vol. 5, jul 2014.

[77] F. Wang, "The optical resonances in carbon nanotubes arise from excitons," *Science*, vol. 308, pp. 838–841, may 2005.

[78] T. Wassmann, A. P. Seitsonen, A. M. Saitta, M. Lazzeri, and F. Mauri, "Structure, stability, edge states, and aromaticity of graphene ribbons," *Physical Review Letters*, vol. 101, p. 096402, aug 2008.

[79] Q. Sun, O. Gröning, J. Overbeck, O. Braun, M. L. Perrin, G. B. Barin, M. E. Abbassi, K. Eimre, E. Ditler, C. Daniels, V. Meunier, C. A. Pignedoli, M. Calame, R. Fasel, and P. Ruffieux, "Massive Dirac fermion behavior in a low bandgap graphene nanoribbon near a topological phase boundary," *Advanced Materials*, vol. 32, p. 1906054, mar 2020.

[80] O. Gröning, S. Wang, X. Yao, C. A. Pignedoli, G. B. Barin, C. Daniels, A. Cupo, V. Meunier, X. Feng, A. Narita, K. Müllen, P. Ruffieux, and R. Fasel, "Engineering of robust topological quantum phases in graphene nanoribbons," *Nature*, vol. 560, pp. 209–213, aug 2018.

[81] G. D. Nguyen, F. M. Toma, T. Cao, Z. Pedramrazi, C. Chen, D. J. Rizzo, T. Joshi, C. Bronner, Y.-C. Chen, M. Favaro, S. G. Louie, F. R. Fischer, and M. F. Crommie, "Bottom-up synthesis of N = 13 sulfur-doped graphene nanoribbons," *The Journal of Physical Chemistry C*, vol. 120, pp. 2684–2687, jan 2016.

[82] R. R. Cloke, T. Marangoni, G. D. Nguyen, T. Joshi, D. J. Rizzo, C. Bronner, T. Cao, S. G. Louie, M. F. Crommie, and F. R. Fischer, "Site-specific substitutional boron doping of semiconducting armchair graphene nanoribbons," *Journal of the American Chemical Society*, vol. 137, pp. 8872–8875, jul 2015.

[83] B. V. Senkovskiy, A. V. Fedorov, D. Haberer, M. Farjam, K. A. Simonov, A. B. Preobrajenski, N. Mårtensson, N. Atodiresei, V. Caciuc, S. Blügel, A. Rosch, N. I. Verbitskiy, M. Hell, D. V. Evtushinsky, R. German, T. Marangoni, P. H. M. van Loosdrecht, F. R. Fischer, and A. Grüneis, "Semiconductor-to-metal transition and quasiparticle renormalization in doped graphene nanoribbons," *Advanced Electronic Materials*, vol. 3, p. 1600490, mar 2017.

[84] C. Chen, J. Z. Wu, K. T. Lam, G. Hong, M. Gong, B. Zhang, Y. Lu, A. L. Antaris, S. Diao, J. Guo, and H. Dai, "Graphene nanoribbons under mechanical strain," *Advanced Materials*, vol. 27, pp. 303–309, oct 2014.

[85] H. Hu, S. M. Loh, T.-C. Leung, and M.-C. Lin, "Strain and screening effects on field emission properties of armchair graphene nanoribbon arrays: a first-principles study," *RSC Advances*, vol. 8, no. 40, pp. 22625–22634, 2018.

[86] J. Lawrence, P. Brandimarte, A. Berdonces-Layunta, M. S. G. Mohammed, A. Grewal, C. C. Leon, D. Sánchez-Portal, and D. G. de Oteyza, "Probing the magnetism of topological end states in 5-armchair graphene nanoribbons," *ACS Nano*, vol. 14, pp. 4499–4508, feb 2020.

[87] Z. Chen, Y.-M. Lin, M. J. Rooks, and P. Avouris, "Graphene nano-ribbon electronics," *Physica E: Low-dimensional Systems and Nanostructures*, vol. 40, pp. 228–232, dec 2007.

[88] M. Y. Han, B. Özyilmaz, Y. Zhang, and P. Kim, "Energy band-gap engineering of graphene nanoribbons," *Physical Review Letters*, vol. 98, may 2007.

[89] L. Jiao, L. Zhang, X. Wang, G. Diankov, and H. Dai, "Narrow graphene nanoribbons from carbon nanotubes," *Nature*, vol. 458, pp. 877–880, apr 2009.

[90] J. M. Tour, "Top-down versus bottom-up fabrication of graphene-based electronics," *Chemistry of Materials*, vol. 26, pp. 163–171, sep 2013.

[91] F. Schulz, P. H. Jacobse, F. F. Canova, J. van der Lit, D. Z. Gao, A. van den Hoogenband, P. Han, R. J. K. Gebbink, M.-E. Moret, P. M. Joensuu, I. Swart, and P. Liljeroth, "Precursor geometry determines the growth mechanism in graphene nanoribbons," *The Journal of Physical Chemistry C*, vol. 121, pp. 2896–2904, jan 2017.

[92] A. Narita, "Synthesis of structurally defined nanographene materials through oxidative cyclodehydrogenation," in *Synthetic Methods for Conjugated Polymers and Carbon Materials*, pp. 183–228, Wiley-VCH Verlag GmbH & Co. KGaA, jan 2017.

[93] R. K. Dubey, M. Melle-Franco, and A. Mateo-Alonso, "Twisted molecular nanoribbons with up to 53 linearly-fused rings," *Journal of the American Chemical Society*, apr 2021.

[94] X. Yang, X. Dou, A. Rouhanipour, L. Zhi, H. J. Räder, and K. Müllen, "Two-dimensional graphene nanoribbons," *Journal of the American Chemical Society*, vol. 130, pp. 4216–4217, apr 2008.

[95] A. Narita, X. Feng, Y. Hernandez, S. A. Jensen, M. Bonn, H. Yang, I. A. Verzhbitskiy, C. Casiraghi, M. R. Hansen, A. H. R. Koch, and et al., "Synthesis of structurally well-defined and liquid-phase-processable graphene nanoribbons," *Nature Chemistry*, vol. 6, pp. 126–132, Dec 2013.

[96] A. Narita, Z. Chen, Q. Chen, and K. Müllen, "Solution and on-surface synthesis of structurally defined graphene nanoribbons as a new family of semiconductors," *Chemical Science*, vol. 10, no. 4, pp. 964–975, 2019.

[97] K.-Y. Yoon and G. Dong, "Liquid-phase bottom-up synthesis of graphene nanoribbons," *Materials Chemistry Frontiers*, vol. 4, no. 1, pp. 29–45, 2020.

[98] L. Talirz, P. Ruffieux, and R. Fasel, "On-surface synthesis of atomically precise graphene nanoribbons," *Advanced Materials*, vol. 28, pp. 6222–6231, Feb 2016.

[99] J. Liu, B.-W. Li, Y.-Z. Tan, A. Giannakopoulos, C. Sanchez-Sanchez, D. Beljonne, P. Ruffieux, R. Fasel, X. Feng, and K. Müllen, "Toward cove-edged low band gap graphene nanoribbons," *Journal of the American Chemical Society*, vol. 137, pp. 6097–6103, may 2015.

[100] D. J. Rizzo, G. Veber, T. Cao, C. Bronner, T. Chen, F. Zhao, H. Rodriguez, S. G. Louie, M. F. Crommie, and F. R. Fischer, "Topological band engineering of graphene nanoribbons," *Nature*, vol. 560, pp. 204–208, aug 2018.

[101] R. M. Jacobberger, B. Kiraly, M. Fortin-Deschenes, P. L. Levesque, K. M. McElhinny, G. J. Brady, R. R. Delgado, S. S. Roy, A. Mannix, M. G. Lagally, P. G. Evans, P. Desjardins, R. Martel, M. C. Hersam, N. P. Guisinger, and M. S. Arnold, "Direct oriented growth of armchair graphene nanoribbons on germanium," *Nature Communications*, vol. 6, aug 2015.

[102] V. Saraswat, Y. Yamamoto, H. J. Kim, R. M. Jacobberger, K. R. Jinkins, A. J. Way, N. P. Guisinger, and M. S. Arnold, "Synthesis of armchair graphene nanoribbons on germanium-on-silicon," *The Journal of Physical Chemistry C*, vol. 123, pp. 18445–18454, jul 2019.

[103] K. Amsharov, M. Kabdulov, and M. Jansen, "Homo-elimination of HF-an efficient approach for intramolecular aryl-aryl coupling," *Chemistry - A European Journal*, vol. 16, pp. 5868–5871, apr 2010.

[104] N. Suzuki, T. Fujita, and J. Ichikawa, "Method for the synthesis of dibenzo[g,p]chrysenes: Domino Friedel–Crafts-type cyclization of difluoroethenes bearing two biaryl groups," *Organic Letters*, vol. 17, pp. 4984–4987, sep 2015.

[105] N. Suzuki, T. Fujita, K. Y. Amsharov, and J. Ichikawa, "Aluminium-mediated aromatic C–F bond activation: regioswitchable construction of benzene-fused triphenylene frameworks," *Chemical Communications*, vol. 52, no. 88, pp. 12948–12951, 2016.

[106] K. Y. Amsharov, M. A. Kabdulov, and M. Jansen, "Facile bucky-bowl synthesis by regiospecific cove-region closure by HF elimination," *Angewandte Chemie*, vol. 124, pp. 4672–4675, apr 2012.

[107] K. Amsharov and P. Merz, "Intramolecular aryl–aryl coupling of fluoroarenes through Al_2O_3-mediated HF elimination," *The Journal of Organic Chemistry*, vol. 77, pp. 5445–5448, jun 2012.

[108] O. Papaianina, V. A. Akhmetov, A. A. Goryunkov, F. Hampel, F. W. Heinemann, and K. Y. Amsharov, "Synthesis of rationally halogenated buckybowls by chemoselective aromatic C–F bond activation," *Angewandte Chemie International Edition*, vol. 56, pp. 4834–4838, mar 2017.

[109] O. Papaianina and K. Y. Amsharov, "Aluminum oxide mediated C–F bond activation in trifluoromethylated arenes," *Chemical Communications*, vol. 52, no. 7, pp. 1505–1508, 2016.

[110] A.-K. Steiner and K. Y. Amsharov, "The rolling-up of oligophenylenes to nanographenes by a HF-zipping approach," *Angewandte Chemie International Edition*, vol. 56, pp. 14732–14736, oct 2017.

[111] D. Sharapa, A.-K. Steiner, and K. Amsharov, "The mechanism of cyclodehydrofluorination on γ-alumina," *Physica Status Solidi (B)*, vol. 255, p. 1800189, jun 2018.

[112] M. Kolmer, R. Zuzak, A. Steiner, L. Zajac, M. Engelund, S. Godlewski, M. Szymonski, and K. Amsharov, "Fluorine-programmed nanozipping to tailored nanographenes on rutile TiO_2 surfaces," *Science*, vol. 363, no. 6422, pp. 57–60, 2019.

[113] A. Chuvilin, E. Bichoutskaia, M. C. Gimenez-Lopez, T. W. Chamberlain, G. A. Rance, N. Kuganathan, J. Biskupek, U. Kaiser, and A. N. Khlobystov, "Self-assembly of a sulphur-terminated graphene nanoribbon within a single-walled carbon nanotube," *Nature Materials*, vol. 10, pp. 687–692, aug 2011.

[114] A. V. Talyzin, I. V. Anoshkin, A. V. Krasheninnikov, R. M. Nieminen, A. G. Nasibulin, H. Jiang, and E. I. Kauppinen, "Synthesis of graphene nanoribbons encapsulated in single-walled carbon nanotubes," *Nano Letters*, vol. 11, pp. 4352–4356, oct 2011.

[115] H. Shiozawa, T. Pichler, A. Grüneis, R. Pfeiffer, H. Kuzmany, Z. Liu, K. Suenaga, and H. Kataura, "A catalytic reaction inside a single-walled carbon nanotube," *Advanced Materials*, vol. 20, pp. 1443–1449, apr 2008.

[116] H. Shiozawa, C. Kramberger, R. Pfeiffer, H. Kuzmany, T. Pichler, Z. Liu, K. Suenaga, H. Kataura, and S. R. P. Silva, "Catalyst and chirality dependent growth of carbon nanotubes determined through nano-test tube chemistry," *Advanced Materials*, vol. 22, pp. 3685–3689, aug 2010.

[117] B. Botka, Á. Pekker, Á. Botos, K. Kamarás, and R. Hackl, "A systematic study of optical and Raman spectra of peapod-based DWNTs," *physica status solidi (b)*, vol. 247, pp. 2843–2846, sep 2010.

[118] X. Liu, H. Kuzmany, T. Saito, and T. Pichler, "Temperature dependence of inner tube growth from ferrocene-filled single-walled carbon nanotubes," *physica status solidi (b)*, vol. 248, pp. 2492–2495, sep 2011.

[119] L. Shi, P. Rohringer, K. Suenaga, Y. Niimi, J. Kotakoski, J. C. Meyer, H. Peterlik, M. Wanko, S. Cahangirov, A. Rubio, Z. J. Lapin, L. Novotny, P. Ayala, and T. Pichler, "Confined linear carbon chains as a route to bulk carbyne," *Nature Materials*, vol. 15, pp. 634–639, apr 2016.

[120] L. Shi, J. Wei, K. Yanagi, T. Saito, K. Cao, U. Kaiser, P. Ayala, and T. Pichler, "Templated direct growth of ultra-thin double-walled carbon nanotubes," *Nanoscale*, vol. 10, no. 45, pp. 21254–21261, 2018.

[121] S. Heeg, L. Shi, T. Pichler, and L. Novotny, "Raman resonance profile of an individual confined long linear carbon chain," *Carbon*, vol. 139, pp. 581–585, nov 2018.

[122] W. Cui, L. Shi, K. Cao, U. Kaiser, T. Saito, P. Ayala, and T. Pichler, "Isotopic labelling of confined carbyne," *Angewandte Chemie International Edition*, mar 2021.

[123] H. E. Lim, Y. Miyata, R. Kitaura, Y. Nishimura, Y. Nishimoto, S. Irle, J. H. Warner, H. Kataura, and H. Shinohara, "Growth of carbon nanotubes via twisted graphene nanoribbons," *Nature Communications*, vol. 4, oct 2013.

[124] T. W. Chamberlain, J. Biskupek, G. A. Rance, A. Chuvilin, T. J. Alexander, E. Bichoutskaia, U. Kaiser, and A. N. Khlobystov, "Size, structure, and helical twist of graphene nanoribbons controlled by confinement in carbon nanotubes," *ACS Nano*, vol. 6, pp. 3943–3953, apr 2012.

[125] H. Kuzmany, L. Shi, J. Kürti, J. Koltai, A. Chuvilin, T. Saito, and T. Pichler, "The growth of new extended carbon nanophases from ferrocene inside single-walled carbon nanotubes," *physica status solidi (RRL) - Rapid Research Letters*, vol. 11, p. 1700158, jul 2017.

[126] E. Gaufrès, N. Y.-W. Tang, F. Lapointe, J. Cabana, M.-A. Nadon, N. Cottenye, F. Raymond, T. Szkopek, and R. Martel, "Giant Raman scattering from J-aggregated dyes inside carbon nanotubes for multispectral imaging," *Nature Photonics*, vol. 8, pp. 72–78, nov 2013.

[127] R. McCreery, *Raman spectroscopy for chemical analysis*. New York: John Wiley & Sons, 2000.

[128] H. Kuzmany, *Solid-State Spectroscopy*. Springer Berlin Heidelberg, 2009.

[129] R. Gillen, M. Mohr, and J. Maultzsch, "Symmetry properties of vibrational modes in graphene nanoribbons," *Physical Review B*, vol. 81, p. 205426, may 2010.

[130] D. J. Gardiner and P. R. Graves, *Practical Raman Spectroscopy*. Springer Berlin Heidelberg, 1989.

[131] M. Milnera, J. Kürti, M. Hulman, and H. Kuzmany, "Periodic resonance excitation and intertube interaction from quasicontinuous distributed helicities in single-wall carbon nanotubes," *Physical Review Letters*, vol. 84, pp. 1324–1327, feb 2000.

[132] I. B. Khaibullin, E. I. Shtyrkov, M. M. Zaripov, R. M. Bayazitov, and M. F. Galjautdinov, "Some features of laser annealing of implanted silicon layers," *Radiation Effects*, vol. 36, pp. 225–233, jan 1978.

[133] A. Dvurechenskii, "The energy pulse-oriented crystallization phenomenon in solids (laser annealing)," in *Advances in Semiconductor Nanostructures*, pp. 367–381, Elsevier, 2017.

[134] P. You, G. Li, G. Tang, J. Cao, and F. Yan, "Ultrafast laser-annealing of perovskite films for efficient perovskite solar cells," *Energy & Environmental Science*, vol. 13, no. 4, pp. 1187–1196, 2020.

[135] C. Kramberger, A. Waske, K. Biedermann, T. Pichler, T. Gemming, B. Büchner, and H. Kataura, "Tailoring carbon nanostructures via temperature and laser irradiation," *Chemical Physics Letters*, vol. 407, pp. 254–259, may 2005.

[136] P. Vecera, J. C. Chacón-Torres, T. Pichler, S. Reich, H. R. Soni, A. Görling, K. Edelthalhammer, H. Peterlik, F. Hauke, and A. Hirsch, "Precise determination of graphene functionalization by *in situ* Raman spectroscopy," *Nature Communications*, vol. 8, p. 15192, May 2017.

[137] J. Chimborazo, *In-situ Raman spectroscopy and synthesis of one dimensional carbon nanostructures*. PhD thesis, University of Vienna, Faculty of Physics, Sept. 2020.

[138] M. Malyj and J. E. Griffiths, "Stokes/anti-Stokes Raman vibrational temperatures: Reference materials, standard lamps, and spectrophotometric calibrations," *Applied Spectroscopy*, vol. 37, pp. 315–333, jul 1983.

[139] B. J. Kip and R. J. Meier, "Determination of the local temperature at a sample during Raman experiments using Stokes and anti-Stokes Raman bands," *Applied Spectroscopy*, vol. 44, pp. 707–711, may 1990.

[140] J. J. Gallardo, J. Navas, D. Zorrilla, R. Alcántara, D. Valor, C. Fernández-Lorenzo, and J. Martín-Calleja, "Micro-Raman spectroscopy for the determination of local temperature increases in TiO_2 thin films due to the effect of radiation," *Applied Spectroscopy*, vol. 70, pp. 1128–1136, jun 2016.

[141] A. Kukovecz, C. Kramberger, V. Georgakilas, M. Prato, and H. Kuzmany, "A detailed Raman study on thin single-wall carbon nanotubes prepared by the HiPCO process," *The European Physical Journal B*, vol. 28, pp. 223–230, jul 2002.

[142] E. G. Röck, "Tunable Raman spectroscopy of single-chirality (n,m) carbon nanotubes," Master's Thesis, University of Vienna, Wien, Sept. 2020.

[143] F. Tuinstra and J. L. Koenig, "Raman spectrum of graphite," *The Journal of Chemical Physics*, vol. 53, pp. 1126–1130, aug 1970.

[144] P. T. Araujo, I. O. Maciel, P. B. C. Pesce, M. A. Pimenta, S. K. Doorn, H. Qian, A. Hartschuh, M. Steiner, L. Grigorian, K. Hata, and A. Jorio, "Nature of the constant factor in the relation between radial breathing mode frequency and tube diameter for single-wall carbon nanotubes," *Physical Review B*, vol. 77, p. 241403, jun 2008.

[145] P. T. Araujo, C. Fantini, M. M. Lucchese, M. S. Dresselhaus, and A. Jorio, "The effect of environment on the radial breathing mode of supergrowth single wall carbon nanotubes," *Applied Physics Letters*, vol. 95, p. 261902, dec 2009.

[146] R. B. Weisman and S. M. Bachilo, "Dependence of optical transition energies on structure for single-walled carbon nanotubes in aqueous suspension: An empirical kataura plot," *Nano Letters*, vol. 3, no. 9, pp. 1235–1238, 2003.

[147] J. Zhou and J. Dong, "Vibrational property and Raman spectrum of carbon nanoribbon," *Applied Physics Letters*, vol. 91, p. 173108, oct 2007.

[148] R. Saito, M. Furukawa, G. Dresselhaus, and M. S. Dresselhaus, "Raman spectra of graphene ribbons," *Journal of Physics: Condensed Matter*, vol. 22, p. 334203, aug 2010.

[149] H. Kuzmany, L. Shi, T. Pichler, J. Kürti, J. Koltai, F. Hof, and T. Saito, "The origin of nondispersive Raman lines in the D-band region for ferrocene@HiPco SWCNTs transformed at high temperatures," *physica status solidi (b)*, vol. 252, pp. 2530–2535, jul 2015.

[150] R. Peköz, X. Feng, and D. Donadio, "Ab initio characterization of graphene nanoribbons and their polymer precursors," *Journal of Physics: Condensed Matter*, vol. 24, p. 104023, feb 2012.

[151] J. Overbeck, G. B. Barin, C. Daniels, M. L. Perrin, O. Braun, Q. Sun, R. Darawish, M. D. Luca, X.-Y. Wang, T. Dumslaff, A. Narita, K. Müllen, P. Ruffieux, V. Meunier, R. Fasel, and M. Calame, "A universal length-dependent vibrational mode in graphene nanoribbons," *ACS Nano*, vol. 13, pp. 13083–13091, oct 2019.

[152] K. Yanagi, T. Iitsuka, S. Fujii, and H. Kataura, "Separations of metallic and semiconducting carbon nanotubes by using sucrose as a gradient medium," *The Journal of Physical Chemistry C*, vol. 112, pp. 18889–18894, nov 2008.

[153] T. Koyama, K. Fujiki, Y. Nagasawa, S. Okada, K. Asaka, Y. Saito, and H. Kishida, "Different molecular arrangement of perylene in metallic and semiconducting carbon nanotubes: Impact of van der Waals interaction," *J. Phys. Chem. C*, vol. 122, pp. 5805–5812, Mar. 2018.

[154] Y. Yamada, O. Kimizuka, K. Machida, S. Suematsu, K. Tamamitsu, S. Saeki, Y. Yamada, N. Yoshizawa, O. Tanaike, J. Yamashita, F. Don, K. Hata, and H. Hatori, "Hole opening of carbon nanotubes and their capacitor performance," *Energy & Fuels*, vol. 24, pp. 3373–3377, apr 2010.

[155] M. E. Abbassi, M. L. Perrin, G. B. Barin, S. Sangtarash, J. Overbeck, O. Braun, C. J. Lambert, Q. Sun, T. Prechtl, A. Narita, K. Müllen, P. Ruffieux, H. Sadeghi, R. Fasel, and M. Calame, "Controlled quantum dot formation in atomically engineered graphene nanoribbon field-effect transistors," *ACS Nano*, vol. 14, pp. 5754–5762, mar 2020.

[156] G. Fábián, C. Kramberger, A. Friedrich, F. Simon, and T. Pichler, "A broadband and high throughput single-monochromator Raman spectrometer: Application for single-wall carbon nanotubes," *Review of Scientific Instruments*, vol. 82, p. 023905, feb 2011.

[157] G. Fábián, C. Kramberger, A. Friedrich, F. Simon, and T. Pichler, "Adaptation of a commercial Raman spectrometer for multiline and broadband laser operation," *physica status solidi (b)*, vol. 248, pp. 2581–2584, oct 2011.

[158] M. Wojdyr, "Fityk: a general-purpose peak fitting program," *Journal of Applied Crystallography*, vol. 43, pp. 1126–1128, sep 2010.

[159] J. Olivero and R. Longbothum, "Empirical fits to the Voigt line width: A brief review," *Journal of Quantitative Spectroscopy and Radiative Transfer*, vol. 17, pp. 233–236, feb 1977.

[160] V. Milotti, M. Melle-Franco, A.-K. Steiner, I. Verbitskii, K. Amsharov, and T. Pichler, "In situ laser annealing as pathway for the metal free synthesis of tailored nanographenes," *Nanoscale Advances*, vol. 3, no. 3, pp. 703–709, 2021.

[161] G. Zhurko, "Chemcraft - graphical program for visualization of quantum chemistry computations.." Ivanovo, Russia, 2005.

[162] M. Dračínský, L. Benda, and P. Bouř, "Ab initio modeling of fused silica, crystal quartz, and water Raman spectra," *Chemical Physics Letters*, vol. 512, pp. 54–59, aug 2011.

[163] C. Li, W. Zheng, Q. Zhu, J. Chen, B. Wang, and X. Ju, "Microstructure variation in fused silica irradiated by different fluence of UV laser pulses with positron annihilation lifetime and Raman scattering spectroscopy," *Nuclear Instruments and Methods in Physics Research Section B: Beam Interactions with Materials and Atoms*, vol. 384, pp. 23–29, oct 2016.

[164] N. Everall, "The influence of out-of-focus sample regions on the surface specificity of confocal Raman microscopy," *Applied Spectroscopy*, vol. 62, pp. 591–598, jun 2008.

[165] T. Weil, T. Vosch, J. Hofkens, K. Peneva, and K. Müllen, "The rylene colorant family-tailored nanoemitters for photonics research and applications," *Angewandte Chemie International Edition*, vol. 49, pp. 9068–9093, oct 2010.

[166] W. Wenseleers, S. Cambré, J. Čulin, A. Bouwen, and E. Goovaerts, "Effect of water filling on the electronic and vibrational resonances of carbon nanotubes: Characterizing tube opening by Raman spectroscopy," *Advanced Materials*, vol. 19, pp. 2274–2278, sep 2007.

[167] J. Campo, S. Cambré, B. Botka, J. Obrzut, W. Wenseleers, and J. A. Fagan, "Optical property tuning of single-wall carbon nanotubes by endohedral encapsulation of a wide variety of dielectric molecules," *ACS Nano*, vol. 15, pp. 2301–2317, dec 2020.

[168] P. H. Tan, A. G. Rozhin, T. Hasan, P. Hu, V. Scardaci, W. I. Milne, and A. C. Ferrari, "Photoluminescence spectroscopy of carbon nanotube bundles: Evidence for exciton energy transfer," *Phys. Rev. Lett.*, vol. 99, p. 137402, Sep 2007.

[169] J. Lefebvre and P. Finnie, "Photoluminescence and Förster resonance energy transfer in elemental bundles of single-walled carbon nanotubes," *The Journal of Physical Chemistry C*, vol. 113, no. 18, pp. 7536–7540, 2009.

[170] A. Ahmad, K. Kern, and K. Balasubramanian, "Selective enhancement of carbon nanotube photoluminescence by resonant energy transfer," *ChemPhysChem*, vol. 10, no. 6, pp. 905–909, 2009.

[171] E. Shafran, B. D. Mangum, and J. M. Gerton, "Energy transfer from an individual quantum dot to a carbon nanotube," *Nano Letters*, vol. 10, no. 10, pp. 4049–4054, 2010. PMID: 20806915.

[172] S. van Bezouw, D. H. Arias, R. Ihly, S. Cambré, A. J. Ferguson, J. Campo, J. C. Johnson, J. Defillet, W. Wenseleers, and J. L. Blackburn, "Diameter-dependent optical absorption and excitation energy transfer from encapsulated dye molecules toward single-walled carbon nanotubes," *ACS Nano*, vol. 12, no. 7, pp. 6881–6894, 2018. PMID: 29965726.

[173] H. Kuzmany, W. Plank, M. Hulman, C. Kramberger, A. Grüneis, T. Pichler, H. Peterlik, H. Kataura, and Y. Achiba, "Determination of SWCNT diameters from the Raman response of the radial breathing mode," *The European Physical Journal B*, vol. 22, pp. 307–320, aug 2001.